

Cryogenic Break-Junction Characterization of Single Organic Molecules

Thomas Grellmann

Forschungszentrum Jülich GmbH
Peter Grünberg Institute/Institute of Complex Systems
Bioelectronics (PGI-8/ICS-8)

Cryogenic Break-Junction Characterization of Single Organic Molecules

Thomas Grellmann

Schriften des Forschungszentrums Jülich
Reihe Schlüsseltechnologien / Key Technologies

Band / Volume 98

ISSN 1866-1807

ISBN 978-3-95806-015-9

Bibliographic information published by the Deutsche Nationalbibliothek.
The Deutsche Nationalbibliothek lists this publication in the Deutsche
Nationalbibliografie; detailed bibliographic data are available in the
Internet at <http://dnb.d-nb.de>.



Bonn-Cologne Graduate School
of Physics and Astronomy



Publisher and
Distributor:

Forschungszentrum Jülich GmbH
Zentralbibliothek
52425 Jülich
Tel: +49 2461 61-5368
Fax: +49 2461 61-6103
Email: zb-publikation@fz-juelich.de
www.fz-juelich.de/zb

Cover Design:

Grafische Medien, Forschungszentrum Jülich GmbH

Printer:

Grafische Medien, Forschungszentrum Jülich GmbH

Copyright:

Forschungszentrum Jülich 2014

Schriften des Forschungszentrums Jülich

Reihe Schlüsseltechnologien / Key Technologies, Band / Volume 98

D 38 (Diss., Köln, Univ., 2014)

ISSN 1866-1807

ISBN 978-3-95806-015-9

The complete volume is freely available on the Internet on the Jülicher Open Access Server (JuSER)
at www.fz-juelich.de/zb/openaccess.

Neither this book nor any part of it may be reproduced or transmitted in any form or by any
means, electronic or mechanical, including photocopying, microfilming, and recording, or by any
information storage and retrieval system, without permission in writing from the publisher.

Abstract

In this thesis, a cryogenic mechanically controllable break-junction (MCBJ) setup is developed and used for the characterization of single organic molecules at different temperatures. Molecules are the building blocks of life and among others responsible for charge transfer in biological processes, e.g. photosynthesis in plants and metabolism in humans. Since these processes are not yet completely understood, single molecules are highly interesting systems to study. Furthermore, due to their astonishing properties they might be used as electronic components in future technologies. This approach is called “molecular electronics”, existing representatives that use thin or thick layers of organic molecules are for instance light emitting diodes (OLED) or liquid crystal displays (LCD). However, single molecule devices are still not in use, and in order to build such systems the single molecules have to be understood, especially their electronic properties.

Since the size of single molecules is typically of the order of nm, their characterization requires an appropriate setup. In this thesis a MCBJ is developed that traps single molecules between two electrodes, and thus allows to characterize its electronic features.

The first aim of this thesis is the construction and development of a cryogenic MCBJ setup, consisting mainly of three parts: (i) the sophisticated sample holder, suitable for measurements inside the helium-flow cryostat, including a piezo-positioner to bend the sample, (ii) an automated setup to control the measurement parameters and acquire the data (e.g. temperature, applied voltage, measured current, piezo-position), and (iii) the development of suitable break-junction samples consisting mainly of a lithographically prepared Au bridge (with nm size dimensions). The three parts together allow measurements of molecules with a position control in the pm regime, currents ranging from below pA to mA, and temperatures ranging from 4 K to room temperature.

The second aim is to develop and to establish adequate procedures for break-junction measurements, regarding mounting of the sample, deposition of molecules and measurement techniques. For the latter one, conductance–position characteristics (CPCs), current–voltages characteristics (IVC), standard CPC histograms and contour histograms are developed, automated and tested in reference measurements without molecules.

The third aim is the measurement of simple “test-bed” molecules. Hexanedithiol and benzenedithiol are chosen as representatives for simple alkanes and conjugated molecules, respectively. CPCs of the rod-like hexanedithiol show a distinct peak in agreement with literature values, while BeDT exhibits a more complex behavior. IVCs are performed on the molecules and molecular levels are obtained. The curves demonstrate the quality of the measurement techniques and the analysis methods.

Finally, the fourth aim is the measurement of the temperature dependent electronic properties of the more complex molecules terphenyldithiol (TPT) and porphyrine (TPyP). The latter one plays an important role in biological processes and represents a promising candidate for molecular electronics. We find, that TPT exhibits a distinct and strongly temperature dependent conductance peak, while the level of the molecular orbital is independent of temperature. It is shown that for TPT a transition from direct tunneling to “hopping” mechanism takes place around a temperature of 100 K. The TPyP displays unusual CPCs. Only tilted plateaus are observed, that are indicative for clustering of the molecule. Contour histograms demonstrate the presence of these clusters in the break-junction. IVCs of TPyP reveal a temperature dependent electronic or vibrational mode. It shifts towards higher voltages with increasing temperature and is therefore only detectable below $T \lesssim 180$ K. Above this temperature reordering of the molecules and the molecule-Au bonds lead to large noise in the IVC at large voltages.

The MCBJ represents an elegant way to detect interesting electronic properties of single molecules. Here, a major aspect is the great stability of the metal-molecule-metal system that allows extensive characterization even in the case of complex molecules. In this thesis it is shown, that lower temperatures improve the performance of the MCBJ, and, even more crucial, temperature dependent measurements allow a deeper insight in the charge transfer of single molecules.

Zusammenfassung

In dieser Arbeit werden organische Einzelmoleküle durch kryogene, mechanisch kontrollierte Bruchkontaktmessungen (englisch: mechanically controllable break-junction, MCBJ) untersucht. Die Grundlage allen biologischen Lebens wird durch organische Moleküle gebildet, die beispielsweise in Prozessen auf denen Photosynthese und Stoffwechselvorgänge beruhen eine wesentliche Rolle spielen. Durch die vielfältigen elektronischen Eigenschaften der organischen Moleküle sind sie auch für die *Molekulare Elektronik* von höchstem Interesse, welche Moleküle als Bausteine für elektrische Schaltkreise zu nutzen versucht. Die Eigenschaften organischer Moleküle werden schon heute in Bauteilen genutzt, beispielsweise in Flüssigkristall-Bildschirmen (LCD) oder organischen Leuchtdioden (OLED). Allerdings sind Einzelmoleküle hierbei keine eigenständigen Bauteile. Um dies zu ermöglichen, müssen die elektrischen Eigenschaften der Moleküle besser verstanden werden.

Da Moleküle typischerweise in der Größenordnung von einigen Nanometern liegen, benötigt ihre Charakterisierung einen geeigneten Aufbau. Die MCBJ wird in dieser Arbeit benutzt um Moleküle zwischen zwei Elektroden zu bringen und dort elektrisch zu charakterisieren.

Die Arbeit kann in vier Teile aufgeteilt werden. Die erste Zielsetzung besteht aus der Entwicklung und Konstruktion eines geeigneten Aufbaus für MCBJ Messungen. Hierbei sind drei Komponenten von großer Wichtigkeit:

(i) Der durchdachte Probenhalter, mit einem Piezo-Positionierer, der für Messungen im Kryostat benutzt werden kann, (ii) ein vollständig automatisierter Aufbau zur Einstellung aller wichtigen Parameter und der Messung der Daten (z.B. Temperatur, angelegte Spannung, gemessener Strom oder Piezo-Position), und (iii) die Entwicklung geeigneter Bruchkontakt-Proben die hauptsächlich aus einer lithographisch hergestellten Goldbrücke (in der Größenordnung von Nanometern) bestehen. Dieser Aufbau erlaubt Messungen an Molekülen mit einer (theoretisch) Pikometer genauen Einstellung der Position, Strom-Messungen bis zu einer Größenordnung von unter Pikoampere und Temperaturen zwischen 4 K und Raumtemperatur.

Der zweite Teil hat die Entwicklung und Etablierung adäquater Messmethoden für die MCBJ, unter anderem den Einbau der Proben, das Aufbringen der Moleküle und verschiedene Messverfahren zum Ziel. Für letztere werden durch Referenzmessungen (ohne Moleküle) Leitfähigkeit-Positionscharakteristika (CPC), Strom-Spannungscharakteristika (IVC), sowie Standard- und Konturhistogramme entwickelt, automatisiert und getestet.

Die dritte Zielsetzung besteht aus der Messung verhältnismäßig einfacher „Testmoleküle“. Als Stellvertreter für Alkane und konjugierte Moleküle werden Hexandithiol (HDT), bzw. Benzendithiol (BeDT) vermessen. Die Leitfähigkeit des „linearen“ HDT, erhalten durch CPC-Messungen, ist relativ eindeutig, während BeDT komplexere Verhaltensweisen mit mehreren Leitfähigkeiten zeigt – beides stimmt mit Literaturwerten überein. Die molekularen Niveaus werden mithilfe von IVCs gemessen, wobei die gemessenen Kurven die Qualität der Messtechnik und der Auswertung demonstrieren.

Der vierte und letzte Teil der Arbeit hat die Untersuchung komplexerer Moleküle, Terphenyldithiol (TPT) und Porphyrine (TPyP), in Abhängigkeit der Temperatur als Zielsetzung. Porphyrine übernehmen wichtige Aufgaben in vielen biologischen Systemen und sind zudem für die molekulare Elektronik von großem Interesse. Der Wert für die Leitfähigkeit von TPT ist temperaturabhängig, während die molekularen Niveaus über den gemessenen Temperaturbereich konstant sind. Es kann gezeigt werden, dass für TPT bei steigender Temperatur eine Änderung im Mechanismus des Elektronentransports auftritt. Bei tiefen Temperaturen dominiert kohärentes Tunneln den

Transport, welches bei etwa 100 K von inkohärentem Tunneln, dem sogenannten „hopping“ (Hüpfen) abgelöst wird. In den CPCs von TPYP können nur geneigte Plateaus gemessen werden welche nicht auf Einzelmoleküle, sondern auf einen Molekülverbund schließen lassen. Konturhistogramme weisen den Einfluss des Molekülverbunds auf den Bruchkontakt nach. IVCs von TPYP zeigen eine interessante Temperaturabhängigkeit die auf einen elektrischen Zustand oder einen Schwingungszustand hinweist. Der Zustand ist nur unterhalb von $T \lesssim 180$ K beobachtbar, da er sich mit zunehmender Temperatur zu höheren Spannungen hin verschiebt wo schließlich starkes Rauschen auftritt. Dies kann durch Reorganisationsprozesse der Moleküle und der Au-Molekül-Bindung erklärt werden.

Die MCBJ stellt eine elegante Methode zur Untersuchung elektrischer Eigenschaften einzelner Moleküle dar. Ein Hauptaugenmerk liegt dabei auf der außergewöhnlichen Stabilität der Metall-Molekül-Metall Systeme, was selbst für komplexe Moleküle ausführliche Messungen erlaubt. In dieser Arbeit wird gezeigt dass tiefe Temperaturen einen wichtigen Aspekt für die MCBJ darstellen und dass temperaturabhängige Charakterisierungen einzelner Moleküle einen tiefen Einblick in ihren Ladungstransport erlauben.

Contents

Abstract	I
Zusammenfassung	III
1 Introduction and Aims	1
2 Theoretical Background	5
2.1 Mechanically Controllable Break-Junction	5
2.2 A Quantum Mechanical Approach	7
2.3 Electron Tunneling Through a Potential Barrier	7
2.4 Conductance Mechanisms of Single Molecules	9
2.4.1 Simmons' Model	9
2.4.2 Resonant Tunneling Model	11
2.4.3 Summary	14
3 Sample Preparation and Experimental Setup	15
3.1 Cryogenic Break-Junction Sample Holder	15
3.2 Electronic Setup	16
3.3 Automation	19
3.4 Sample Design and Preparation	20
3.4.1 Preparation Steps	20
3.4.2 Au Deposition	23
3.4.3 Design of the Break-Junction	26
3.5 Mounting the Sample	27
4 Results and Discussion	31
4.1 Reference Measurements	31
4.1.1 Conductance–Position Characteristics	31
4.1.1.1 Attenuation Factor	32
4.1.1.2 Histogram	35
4.1.1.3 Contour Histogram	37
4.1.2 Current–Voltage Characteristics	40
4.2 Characterization of Molecules	41
4.2.1 Characterization Methods	41
4.2.1.1 Conductance–Position Characteristics	41
4.2.1.2 Resonant Tunneling Model	43
4.2.1.3 Fowler–Nordheim Plot	43
4.2.1.4 Double Logarithmic Plot	44
4.2.1.5 Derivatives of the IVC	44
4.3 Hexanedithiol and Benzenedithiol	46
4.4 Terphenyldithiol	55
4.5 Porphyrines	61
5 Summary	69
6 Danksagung	73

References	75
A The Quantum of Conductance	81
B Chemical Analysis	83
C Eidesstattliche Erklärung	87

1 Introduction and Aims

Molecules are not only the basis for all liquids and nearly all gases. Moreover, *organic molecules* represent the building blocks for life, i.e. humans, animals and plants. Among others, organic molecules are responsible for complex charge transfer processes in biological systems, e.g. in metabolism processes or photosynthesis.

In contrast, charge transfer in classical electric circuits is based on metallic structures, mostly silicon, with a repeating (crystalline) atomic structure. In the last decades the question has arisen:

Can we combine the two worlds?

More explicitly, is it possible to include organic molecules in electric circuits and to use their unique properties in *Molecular Electronics*?

The term organic is historically derived, and used since ancient times. In 1806 the Swedish chemist Jöns Jacob Berzelius introduced the term organic chemistry since he considered that only living organisms (“vis vitalis”) were able to create organic molecules (although already in 1828 the German chemist Friedrich Wöhler proved this wrong by the synthesis of urea) [62]. As a rule of thumb, organic molecules consist of a significant amount of carbon, and most have C-C or C-H bonds. The variability of carbon is the reason for the versatility of organic molecules. In the recent years, organic molecules entered the field of electronic devices, such as the organic light-emitting diode (OLED), liquid crystal displays (LCD) or various sensor devices. While thin or thick layers of organic molecules are already used in nowadays electronic technology, *single* organic molecules might play a role for the fabrication of new designed electric circuits of the future. Contrary to building electric circuits via the classical “top-down” method in which the device is patterned via subtractive methods (e.g. etching) from the bulk, a “bottom-up” technique could be possible for this so called molecular electronics, i.e. arranging the circuit from single molecules. The smallest scale accessible with this approach is a circuit consisting of individual molecules as electrical components, where single molecules could act as wires, resistors, diodes or transistors.

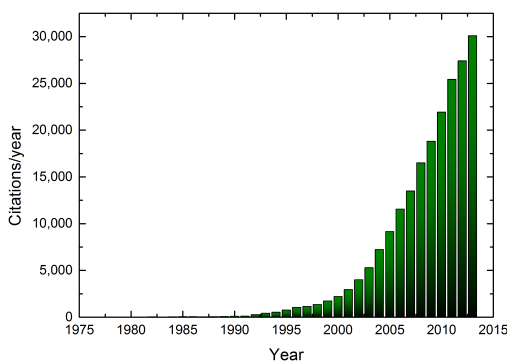


Figure 1: Citations per year in the topic “Molecular Electronics” [8]

The term molecular electronics was introduced in the 1970’s by Aviram and Ratner [9]. Fig. 1 shows the rapid increase of scientific citations regarding the topic “molecular electronics” in the past years, proving the growing interest in this field [8]. One motivation to study molecular

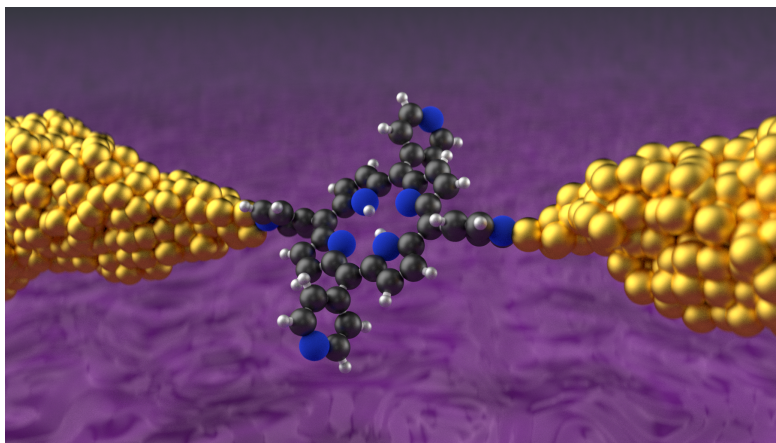


Figure 2: Sketch of a molecule trapped between two electrodes in the MCBJ.

electronics are the shrinking feature sizes in classical electric circuits. The miniaturization of the standard silicon (Si) process techniques eventually reaches its theoretical limits. A combination of Si-technology and molecular electronics could be one possibility to maintain the improvements of the performance of the information technology of the last decades (for instance described by “Moore’s law”). The use of molecular structures for electronic purposes provides several advantages:

- The small size of the molecules could lead to a higher efficiency and speed of the system.
- The possible self-assembly of molecules on nano-scale might be used as a production step of electric circuits.
- The large variety of molecules could allow novel electronic functionalities not available in conventional devices.

Although molecular electronics will probably never replace the silicon-based technique, it could complement it, for instance by including molecular based components with improved or novel functionalities. Furthermore, bio-compatible devices are imaginable, which for instance could be implemented in the body and help to prevent or cure diseases, act as prosthesis or monitor body functions [12, 33].

Furthermore, electron transfer mechanisms represent a central part not only in physics and chemistry, but also play a major role in all enzymatic cycles in biological systems. Although the mechanisms have been investigated for several decades, however, they are not fully understood yet (e.g. the electron transfer from one redox active side to the other of the protein). In order to understand these and similar mechanisms of charge transfer in small organic systems, the electronical analysis of single organic molecules can be helpful.

The aim of this thesis was to characterize the electronic properties of single organic molecules. For this purpose, a cryogenic and automated mechanically controllable break-junction (MCBJ) setup is developed that allows to electronically measure molecules that are trapped between two gold electrodes (see Fig. 2). The different tasks of this work are in detail:

1. Development and automation of a cryogenic MCBJ setup.
2. Development and optimization of a sample preparation, including the break-junction and the molecule deposition.
3. Test and optimization of the setup and measuring and analyzing procedures using Au nano bridges without deposited molecules, with alkanes (hexanedithiol) and with conjugated systems (benzenedithiol) for first tests.
4. Characterization of the electron transport in more complex and important molecules, terphenyldithiol and tetrapyrildiporphine.

Chap. 2 provides a basic introduction to the physics of small systems and molecules. The experimental setup and the sample preparation are described in Chap. 3, and the main results and the discussion can be found in Chap. 4. Here, the data are analyzed and the molecules are investigated. Finally, a summary is given in Chap. 5.

2 Theoretical Background

This chapter provides a first basic insight of the working principle of a mechanically controllable break-junction (MCBJ) and an overview of the theoretical description of basic ingredient of the MCBJ, i.e. the metal-molecule-metal contact. The discussion is necessarily oversimplified since a more detailed introduction would go beyond the scope of this thesis. However, the goal is to provide the basis for a general understanding of the charge transfer of electrons, and their dependence on voltage, distance, and temperature.

The working principle of the break-junction is introduced in Chap. 2.1, a basic quantum mechanical description for electron tunneling, which plays an important role for understanding the MCBJ, follows in Chaps. 2.2 and 2.3. Finally, the standard models that describe the conductance of single molecules are presented in Chap. 2.4. Detailed information on the theoretical background of the chapters can be obtained for instance in Ref. [12, 27, 33].

2.1 Mechanically Controllable Break-Junction

The mechanically controllable break-junction (MCBJ) represents an ideal method to investigate electronic and mechanical properties of single molecules. The main component is a metallic nano contact on a flexible substrate which is mechanically controlled by the reversible bending of the substrate via a manipulator, for instance a motor or a piezo-positioner (see Fig. 3 a). Well defined vertical movements of the manipulator bent the substrate and as a result separate the junction.

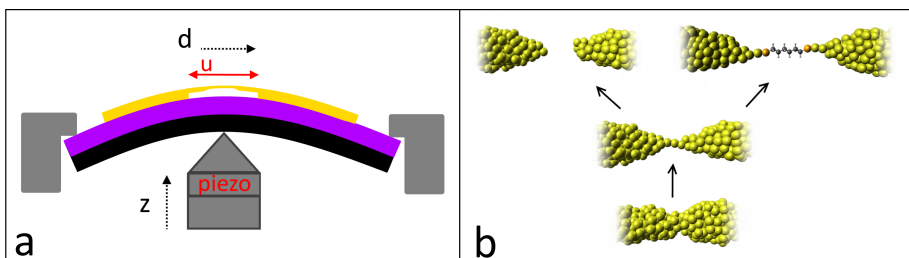


Figure 3: Sketch of the working principle of the mechanically controllable break-junction. (a) A metallic substrate (black) is mounted into the sample holder and precisely bent vertically by a piezo-positioner in z -direction. The nano gold (Au) junction with a freestanding bridge of length u (yellow)—on top of the substrate and an isolating layer (purple)—is therefore displaced in lateral direction d . Since the Au bridge has a constriction of only several 10 nm in diameter, the displacement leads to a reduction of the cross section until only one atom connects the electrodes and finally causing a breaking. This process is sketched in (b). If molecules are deposited onto the Au, eventually a molecule can be trapped between the Au tips, see right hand side in (b), and thus can be characterized electronically.

Due to the precise movement of the positioner and the geometrically defined attenuation factor that converts the vertical movement z to a horizontal movement d , the gap between the two gold tips can be controlled on sub-nanometer scale (in our setup theoretically in the pm range, see Chap. 4.1.1.1). The molecules are placed between the tips and thus mechanical and/or electronic properties of the molecules can be analyzed.

As long as the break-junction is intact, i.e. the metallic nano bridge consists of more than several hundred atoms, it shows a macroscopic behavior. That is, the current I is proportional to

the applied voltage V . This means it obeys Ohm's law:

$$I = V/R, \quad (1)$$

with the resistance R . In this case bending of the substrate mainly reduces the cross section A of the bridge and the resistance increases continuously. Since the length l of the underetched part stays nearly constant, the decrease of the cross section of the contact is simply described by

$$R = \rho_0 \frac{l}{A_{\text{eff}}}, \quad (2)$$

where ρ_0 is the specific electrical resistance, and A_{eff} is the effective cross section of the nano contact. The continuous increase of the resistance, i.e. reduction of the conductance, stops when the cross section reaches atomic size. For some materials, depending on the mechanical properties (especially ductility), finally a single atom contact is formed.

At this point, quantum effects have to be considered, and Ohm's law cannot be applied anymore, since the scattering length of the electrons is typically larger than the atomic structure. In the Landauer model (see Chap. 2.4.2) for the zero temperature limit and low voltages, the current becomes:

$$I = \left(\frac{2e^2}{h}T\right)V. \quad (3)$$

This describes the situation for one transmission channel with $0 \leq T \leq 1$. Consequently, the maximal conductance of *one* transmission channel, i.e. $T = 1$, is:

$$G_0 := \frac{2e^2}{h} \approx 77 \mu\text{S} \approx (13 \text{ k}\Omega)^{-1}, \quad (4)$$

the so called *quantum of conductance* (a more intuitive derivation of G_0 can be found in appendix A). This provides a remarkable result. For the nano contact the conductance changes in a step-like manner, and the proportionality does not depend on material specific properties, like the density of states. To oversimplify, a nano bridge consisting of only one atom has a resistance of $G_0^{-1} = 13 \text{ k}\Omega$. G_0 represents a fundamental value that can be calculated from natural constants (see Eq. 4).

For some materials—like Au—a plateau occurs at G_0 in the conductance–position characteristics (CPC) since chain-like atomic structures develop, that sustain some mechanical strain (see middle structure in Fig. 3 b). Finally, the maximum strain is executed and the chain breaks, which result in a sudden decrease of the conductance to values $G \ll G_0$.

If molecules are deposited onto the bridge, the measurement can change. First the molecules do not contribute to the conductance. However, as the junction breaks a molecule can be trapped between the two Au tips. This situation is illustrated on the right side of Fig. (3 b). Further bending does not change the conductance since the molecule pulls out a chain of Au atoms, similar to the procedure at the quantum of conductance. The probability for measuring a molecular plateau depends on the properties of the specific molecule, e.g. length and flexibility. However, the end groups which have to connect to the Au atoms, play the major role. The stronger the bond to Au, the better is the ability to extract a chain of atoms out of the tips and hence detect the molecule as a signature in the measurement. If the displacement of the Au electrodes is stopped, the molecule can be characterized by using current–voltage curves (IVC) to obtain basic properties, e.g. molecular energy levels. Increasing the bending further, finally leads to the rupture of the metal-molecule-metal connection and an exponentially decreasing tunnel current.

Up to this point the idea of the working principle of the break-junction can be understood by

classical physics. However, if we want to understand the physics of charge transport through a nano-junction and later characterize molecules, we have to use quantum mechanical approaches. This is the aim of the next chapters.

2.2 A Quantum Mechanical Approach

In contrast to classical mechanics, quantum mechanics provides no precise prediction of the position or momentum of a particle. Instead the quantum state of the particle is described by a wave function (for a detailed introduction, see Ref. [27]). In general, this wave function contains all information of all particles (not only one) in the system and can be interpreted as a probability amplitude. The squared modulus of the wave function represents the probability density function:

$$|\Psi(x, t)|^2 = \rho(x, t). \quad (5)$$

It does not provide an exact location of the particle, but a relative likelihood of finding the particle in a measurement at a given time t at a given position x .

The Schrödinger equation (Erwin Schrödinger, 1926) (Ref. [49, 50, 51, 52]) represents the basic equation for quantum mechanics. The form is adapted from classical mechanics, however a priori derivation does not exist. The most general notation for the Schrödinger equation is:

$$i\hbar \frac{\partial \Psi}{\partial t} = \hat{H} \Psi, \quad (6)$$

where \hbar is Planck's constant $\hbar/2\pi$, \hat{H} represents the Hamilton operator and corresponds to the total energy of the system.

For a non relativistic particle with mass m moving in an one-dimensional potential $U(x)$ the Hamiltonian is $\hat{H} = \hat{p}^2/2m + U(x) = -\frac{\hbar^2}{2m} \frac{\partial^2}{\partial x^2} + U(x)$ which leads to the following form of the Schrödinger equation:

$$-\frac{\hbar^2}{2m} \frac{\partial^2 \Psi(x, t)}{\partial x^2} + U(x) \Psi(x, t) = i\hbar \frac{\partial \Psi(x, t)}{\partial t}. \quad (7)$$

In principle, we can determine the wave function of an electron in a tunnel junction (with or without molecule) with Eq. 7.

2.3 Electron Tunneling Through a Potential Barrier

Let us first consider an open metal junction, i.e. the situation of the break-junction without molecule after rupture. It consists of two metal surfaces opposing each other and thus forming a small gap between them. We can simply model the electron transfer by a rectangular potential barrier which separates two regions in which electrons can move as free particles. Close to the surface of the metals an electron experiences a potential that prevents it from leaving the metal. To overcome this potential (and thus allow the electron to move away from the surface) an energy is required which is usually called the "work function" Φ of the metal. The work function depends on the metal and lies typically in the order of a few electron volts (e.g. $\Phi_{\text{Au}} \approx 5.3 \text{ eV}$ [31]). In this picture the work function defines the height of the barrier, the width of the barrier corresponds to the gap between the two metals.

According to this classical description, the energy barrier cannot be passed by electrons if their energy is too small. However, in the quantum mechanical description the electron is allowed to "tunnel" through the potential barrier even if it possesses an energy that is smaller than Φ . Applying the Schrödinger equation (Eq. 7) we obtain the general form of the solution for this

non-relativistic, one-dimensional problem [27]:

$$\Psi(x) \propto \exp(\pm ikx), \quad (8)$$

with the imaginary unit i and k the wave number. The plus and minus signs describe incident and reflected waves, respectively. For an electron on the left side of the barrier the Hamilton operator contains only the kinetic energy of the free electron $\hat{H} = -\frac{\hbar^2}{2m} \frac{\partial^2}{\partial x^2}$. The resulting wave function is a combination of the two (incident and reflected) complex waves

$$\Psi_L(x) = \exp(ik_fx) + r \exp(-ik_fx). \quad (9)$$

For convenience, the amplitude of the incident wave is typically set to 1, i.e. only one electron is considered. Here, r with $0 < r < 1$ represents the reflective index, and the wave number of the free electron is given by:

$$k_f = \sqrt{2mE}/\hbar. \quad (10)$$

The real part of the wave function—which is the only physically observable part—is a sinusoidal oscillating wave (see Fig. 4). The electron propagates through the metal and the propagation is described by the wave number k_f .

Inside the barrier of height Φ_0 the Hamilton operator changes to $\hat{H} = -\frac{\hbar^2}{2m} \frac{\partial^2}{\partial x^2} + \Phi_0$ and the resulting Schrödinger equation is:

$$-\frac{\hbar^2}{2m} \frac{\partial^2}{\partial x^2} \Psi(x) + \Phi_0 \Psi(x) = E. \quad (11)$$

Using the approach given in Eq. 8, the solution for the electron inside the barrier is given by:

$$\Psi_b(x) = A \exp(ik_bx) + B \exp(-ik_bx). \quad (12)$$

A and B are constants that can be obtained by the two boundary conditions for the wave functions between the metals and vacuum. The wave number is now

$$k_b = \sqrt{\frac{2m(E - \Phi_0)}{\hbar^2}}. \quad (13)$$

Since we assume that the energy of the electron E is smaller than the height of the barrier Φ_0 , the argument of the square root is negative. By introducing a real wave number κ_b

$$i\kappa_b := k_b = i \sqrt{\frac{2m(\Phi_0 - E)}{\hbar^2}} \quad (14)$$

Eq. 12 becomes

$$\Psi_b(x) = A \exp(\kappa_bx) + B \exp(-\kappa_bx). \quad (15)$$

The resulting wave function has no imaginary part. Depending on the choice of A and B , the wave function can grow exponentially or decay exponentially with increasing x . Since the first part of the solution (Eq. 15) does not make sense (in this case the probability to find a particle in the gap would increase with increasing distance from the electrode) $A = 0$. Thus, the wave function exponentially *decays* inside the barrier:

$$\Psi_b = B \exp(-\kappa_bx). \quad (16)$$

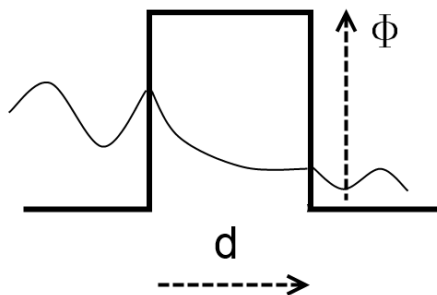


Figure 4: Electron tunneling through a thin barrier of height Φ and thickness d , inside the barrier the wave function decreases exponentially.

Therefore, in contrast to the classical picture, there is *always* a finite probability to find electrons on the right hand side of a finite barrier (see Fig. 4). This effect is known as “tunneling”.

2.4 Conductance Mechanisms of Single Molecules

Based on the quantum mechanical idea, different approaches exist that describe the conductance of a single molecule trapped between two electrodes, ranging from simple tunneling models to *Density Functional Theory* simulations [10, 11]. A more qualitative understanding of measurements of small single molecules is possible with simpler approaches. In the next chapters two basic models are introduced that provide a useful interpretation of the current–voltage curves of single molecules.

2.4.1 Simmons' Model

Similar to the consideration in Chap. 2.2 a molecule between two electrodes can be modeled by a rectangular potential barrier (see Fig. 5). If we apply a voltage, the potential between both contacts is shifted. In 1963, Simmons derived an expression for the current density for an one-dimensional, small insulator sandwiched between two metal electrodes, using the Wentzel–Kramers–Brillouin (WKB) approximation to simplify the Schrödinger equation, Eq. 7. For a rectangular barrier in the zero-temperature limit the equation for the net tunnel current density is then given by

$$J = \left(\frac{e}{2\pi\hbar\alpha d^2} \right) \left\{ \Phi_B \exp \left[-\frac{\sqrt{8m}}{\hbar} \alpha d \sqrt{\Phi_B} \right] - (\Phi_B + eV) \exp \left[-\frac{\sqrt{8m}}{\hbar} \alpha d \sqrt{\Phi_B + eV} \right] \right\}, \quad (17)$$

with the electron mass m , the elementary charge e , a barrier width d and an average height Φ_B relative to the negative electrode, and an applied voltage V (see Fig. 5). Furthermore, α is a dimensionless factor which helps to fit the Simmons equation to data. Often it is considered to account for the effective mass of the electrons in the junction. For a free electron $\alpha = 1$ (effective mass $m^* = m$), whereas in complex systems α —and therefore the effective mass of the electron—can become very small or large [48].

Eq. 17 can be simplified for different regimes of the applied voltage. In the case of a relatively small voltage compared to the barrier height ($eV \ll \Phi_0$, with Φ_0 being the barrier height at zero voltage) the tilting of the barrier can be neglected, and the barrier height becomes $\Phi_B \approx \Phi_0 =$

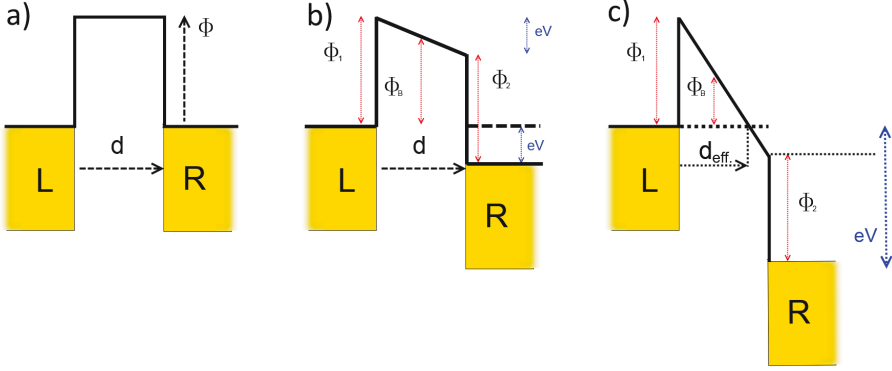


Figure 5: Tunneling through a small rectangular potential wall (with height Φ and width d) between two electrodes (L,R) (a). The vertical axis represents the energy. By applying a voltage the Fermi level of the right electrode is shifted and for small voltages the barrier stays nearly rectangular (b). However, if the applied voltage is relatively large, the barrier shows a triangular behavior, affecting the effective width and height of the barrier (c).

$(\Phi_1 + \Phi_2)/2$ (Fig. (5 a)). In this regime the current density is:

$$J_I = V \left(\frac{\sqrt{2m\Phi_B} e^2}{4\pi^2 \hbar^2 d \alpha^2} \right) \exp \left[-\frac{\sqrt{8m}}{\hbar} \alpha \sqrt{\Phi_B} d \right] \quad (18)$$

or

$$J_I = V J_k \frac{\sqrt{\Phi_B}}{d} \exp \left[-Bd \sqrt{\Phi_B} \right], \quad (19)$$

with $B := \sqrt{\alpha^2 8m}/\hbar$ and $J_k := \sqrt{e^4 2m}/(4\pi^2 \alpha \hbar^2)$. In the low voltage regime, the current decreases exponentially with the distance d , similar to the case of electrons tunneling between the contacts without molecules (see Chap. 2.3). Furthermore, the current density J is proportional to the applied voltage V , i.e. the current–voltage curve should exhibit a linear behavior.

If we apply an *intermediate* voltage but $eV < \Phi_0$, the barrier height can be averaged by $\Phi_B \approx (\Phi_1 + \Phi_2 - eV)/2$, Fig. (5 b) and the current density becomes

$$J_m = J_k \frac{\sqrt{\Phi_B}}{d} \exp[-Bd \sqrt{\Phi_B}] \left\{ V + \frac{Bde^2}{32} \left(\frac{Bd}{3\Phi_0} - \frac{1}{\Phi_0^{3/2}} \right) V^3 \right\}. \quad (20)$$

Again the current density decreases exponentially with the distance, but there is an additional cubic term in the current–voltage characteristic.

By increasing the voltage even more ($eV > \Phi_B$) the tilting of the barrier becomes strong enough to decrease the effective width of the barrier to d_{eff} (see Fig. (5 c)). Tunneling is now only possible in one direction (left to right), since no empty states for the tunneling are available in the left electrode. If we neglect image charges, this is the same situation that occurs in field emission from a metal into the vacuum. According to reference [12] Eq.(17) can then be simplified to

$$J_h = \frac{V^2}{d_{\text{eff}}^2} \frac{2.2e^3}{8\pi\hbar} \exp \left[-\frac{2}{2.96e} \frac{Bd}{V} \Phi_1^{3/2} \right], \quad (21)$$

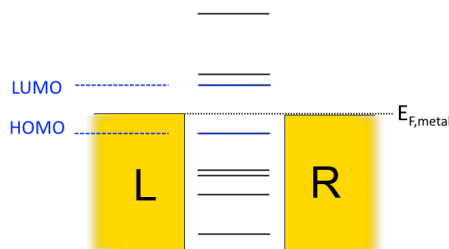


Figure 6: Sketch of the concept of the resonant tunneling model, the x-axis represents the position and the y-axis the energy. Two metal electrodes (L and R) form a small gap while a molecule is placed inside. The metal electrodes are filled continuously with electron states up to the Fermi energy E_F , while the molecule has sharp orbitals (which are broadened inside the junction). Every orbital has a different energy, the highest occupied molecular orbital (HOMO) is the closest orbital below the Fermi energy, while the lowest unoccupied molecular orbital (LUMO) is the closest orbital above the Fermi energy of the electrodes.

where d_{eff} represents the effective width of the barrier. In this regime J depends in a complex way on the effective width and the applied voltage. This regime is often called *Fowler-Nordheim tunneling*. However, one should note that Eq. 21 is the result of the simplification given in Eq.17. An exact solution for this problem can be obtained by using the so called Airy functions [18].

The basic results of the Simmons model can be useful for understanding the basic principles, however, conductance through molecular orbitals is completely neglected. Although the Simmons model is still often used to explain basic mechanisms, the approach to simulate a molecule between two electrodes with one potential barrier is obviously oversimplified, even if the molecule has a very high resistance. Since the molecule attaches to two electrodes, there should be at least two tunnel barriers, i.e. from the left electrode to the molecule and from the molecule to the right electrode. In the next chapter another basic model is introduced which uses two tunnel barriers and one molecular orbital.

2.4.2 Resonant Tunneling Model

The general principle of resonant tunneling is based on the problem of an electron tunneling through two barriers. In this case a resonance occurs at energy states that are defined by the distance between the two tunnel barriers. Since the arrangement of the metal-molecule-metal bears some similarity with the above described situation, the model described below is called Resonant Tunneling Model (RTM). However, the name is misleading. No resonances are described by this model, but the influence of an molecular energy level on the conductance of the junction.

The basic idea of the model is to mimic the situation of a molecule that is trapped between two electrodes (Fig. 6). Charges and energy levels rearrange, if the molecule binds to the metal. The metallic electrodes possess continuously filled energy states up to the Fermi energy of the metal, whereas the molecular orbitals are defined by sharp energy levels (that broaden a bit due to the hybridization of the states of the metal with the molecular orbitals). In case of charge transport through the molecule, in principle each of these molecular orbitals can contribute to the conductance. However, usually only one single orbital dominates the charge transport through the molecule. Obviously, in the most cases this orbital is the highest occupied molecular orbital

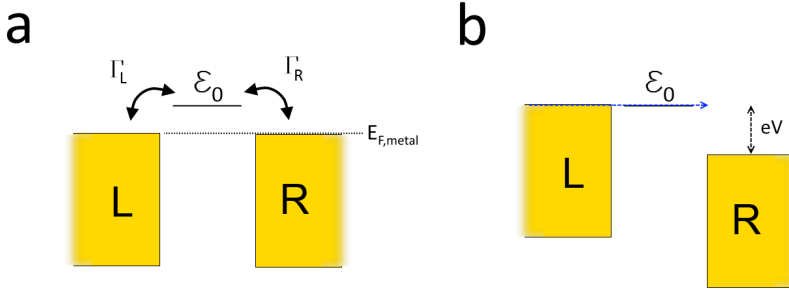


Figure 7: The RTM assumes that only one orbital contributes to the transport through the molecule. In most cases this assumption is convenient, since one orbital (probably HOMO or LUMO close to the Fermi energy) will dominate the charge transport. In this case the scattering rates $\Gamma_{R/L}$ and the energy of the orbital ϵ_0 describe the charge transfer in the RTM (a). By applying a voltage, the Fermi energy of the metals shift, and for high enough voltages the conductance increases dramatically if the molecular orbital ϵ_0 is aligned with the Fermi energy of one electrode (b).

(HOMO) or the lowest unoccupied molecular orbital (LUMO) which both lie next to the Fermi energy of the electrodes. Therefore, in the RTM the electronic structure of the molecule is approximated by a single orbital with the energy ϵ_0 (Fig. 7). Furthermore, we need two parameters that describe the coupling strength (or the scattering rate) of the orbital to the electrodes, i.e. Γ_L for the coupling to the left electrode (L), and Γ_R to the right electrode (R), respectively (this is again different to the classical resonant tunneling where two tunnel contacts are required). By applying a voltage to the electrodes, the Fermi levels of the metal shift. At a certain energy (eV) the voltage is high enough for the Fermi energy to reach the level of the molecular orbital (HOMO or LUMO). This leads to a dramatic increase in the current–voltage curve (IVC).

Generally, the current through a junction for the case of one resonant quantum state can be obtained via *Nonequilibrium Green’s Function formalism* (NEGF) (for an introduction and an overview of NEGF, see Refs [28, 45]). One can use the so called *Keldysh* formalism of the NEGF to formulate current–voltage characteristics. Starting with a tight binding Hamiltonian for the two electrodes, the Hamiltonian for each electrode is simple, and the coupling between the two electrodes is treated as a perturbation. The voltage dependence is just given by a shift of the energy level of one electrode. If only the two outermost atoms in the junction interact we get an expression for the current between the electrodes, as an integral over the energy of the electrons.

$$I(V) = \frac{2e}{h} \int_{-\infty}^{\infty} dE T(E, V) [f_L(E) - f_R(E)] \quad (22)$$

with f_L and f_R being the Fermi function of the left and right electrode, respectively. At zero temperature the electron states are filled up to the Fermi energy, and higher energy states are not occupied. The most complex part is the transmission probability $T(E, V)$ for the electrons, depending on the local electronic structure of the electrodes and the strength of the coupling. Eq. 22 is similar to the simplest form of the *Landauer formula*, a famous formula already introduced in the 1950’s [39].

In the case of the RTM we just consider a single orbital that is coupled to the electrodes. Within the so called “wide-band approximation” (i.e., the Green’s function of the electrodes does not

depend on an energy close to ϵ_0) one can calculate the transmission probability:

$$T_{\text{res}}(E) = \frac{4\Gamma_L\Gamma_R}{(E - \epsilon_0)^2 + (\Gamma)^2}, \quad (23)$$

with $\Gamma := \Gamma_L + \Gamma_R$. This expression is known as the Breit-Wigner formula [15]. Here, Γ_L and Γ_R are considered not to depend on the voltage or energy. This approximation is reasonable if the density of states is relatively flat at the Fermi energy, which is true for noble metals like Au. With the Breit-Wigner formula for the transmission probability the integral in the simple form of the Landauer formula (Eq. 22) can be solved analytically for similar couplings $\Gamma_L = \Gamma_R$

$$I(V) = \frac{G_0}{e} \frac{4\Gamma_L\Gamma_R}{\Gamma} \left[\arctan\left(\frac{eV/2 - \epsilon_0}{\Gamma}\right) + \arctan\left(\frac{eV/2 + \epsilon_0}{\Gamma}\right) \right], \quad (24)$$

with the quantum of conductance G_0 . Eq. 24 describes the form of the IV curve in the resonant tunneling model. For low voltages, the current increases nearly linear with the applied voltage since the molecular level does not contribute to the conductance. However, at higher voltages the level starts to align with the chemical potential of one of the electrodes and thus contributes to the transport. The current starts to enhance significantly (stronger than linear). The size of this regime is defined by the finite broadening of the orbital. Finally, at voltages higher than $V_{\text{sat.}} \gtrsim 2|\epsilon_0|$, the current saturates to

$$I_{\text{sat}} = \frac{G_0}{e} \frac{4\Gamma_L\Gamma_R}{\Gamma}. \quad (25)$$

In order to reach this saturation for most molecules, several volts have to be applied, since HOMO or LUMO typically lie some eV above or below the Fermi energy of the metal. Again the quantum of conductance plays a major role for the description of the electronic properties of small systems. However, one should note that the name “quantum of conductance” can be misleading. Firstly, despite the name, G_0 is not the smallest conductance possible, as for instance the *Planck length* is for the distance. It is a useful value for the description of small conductance channels since it can be expressed by natural constants, similar to the *Rydberg constant* for spectroscopy. Secondly, the quantum of conductance does not behave like a “typical” conductance. Since it describes the probability of transmission through the quantum channel, no power is dissipated in the channel itself. The power is dissipated in the bulk material where the electrons scatter. Therefore, relatively high voltages can be applied and relatively high currents can flow through the nano channel (see Chap. 4.5).

Mechanism	Voltage dependence	Temperature dependence
Simmons/direct tunneling	$J \propto V$	none
Fowler-Nordheim/field emission	$\ln(J/V^2) \propto V^{-1}$	none
Thermionic emission	$\ln(J) \propto V^{1/2}$	$\ln(J/T^2) \propto T^{-1}$
Hopping	$J \propto V$	$\ln(J/V) \propto T^{-1}$

Table 1: Selection of different conductance mechanisms and their dependence from voltage V and temperature T (from [56]).

2.4.3 Summary

The Simmons model and the resonant tunneling model are descriptions of coherent tunneling. While the Simmons model describes the tunneling through a (tilted) potential barrier, the RTM considers one dominating molecular orbital that influences the charge transport. Although coherent tunneling is not temperature dependent, in the RTM the temperature dependent can be expressed by the fitted parameters. However, despite the two discussed models, usually a separation into different transport mechanisms takes place, depending on their current dependence on voltage and temperature.

Tab. 1 summarizes the standard conductance mechanisms. Direct tunneling and field emission are different regimes of the same conduction mechanism, elastic tunneling. However, since they exhibit clearly different voltage dependencies they are usually considered as different mechanisms. While in the direct tunneling the current is proportional to the voltage, for the field emission a complex dependence of the current from the voltage is observed. In the case of thermionic emission (which is also a coherent transport), the electron virtually “jumps” over the molecule due to thermal excitation, therefore a strong temperature dependence is observed. Finally, “hopping” is an incoherent transport, where an electron is inelastically transported through a molecule via multiple coherent steps. It is often used as a description for electron transfer in biological systems, e.g. in the “Marcus theory” [37]. Since hopping is a statistical process, higher temperatures lead to a higher electron transfer rate. Hence, the hopping conductance is also strongly temperature dependent. In this thesis, mainly the resonant tunneling model and the Fowler-Nordheim description is used to analyze the coherent transport through the molecules, and the hopping model for the incoherent molecular transport.

3 Sample Preparation and Experimental Setup

A sophisticated setup, regarding size and control, is required to perform measurements in a large temperature range. Hence, one of the major aims of this work was the development of a cryogenic setup for mechanically controllable break-junction experiments. This includes not only the design and assembly of the setup, but also the fabrication process of the break-junction sample and the optimization of the sample holder including the connection of the electronic devices. Additionally, the setup is automatized to improve control of the parameters and the data acquisition, and to allow continuous (e.g. over night) measurements.

Sample holder and electronic setup are described in Chap. 3.1 and 3.2, the automation is presented in Chap. 3.3. The sample preparation is described in Chap. 3.4, and finally Chap. 3.5 provides an overview of the preparation and mounting procedure of the sample.

3.1 Cryogenic Break-Junction Sample Holder

The central part of the experimental setup is the sample holder for the cryogenic measurements that was developed, assembled and tested in the framework of this thesis. Fig. (8 a) shows the construction sketch of the sample holder. The size of the cryostat (inner diameter 50 mm) defines the limitation of the size of the complete system.

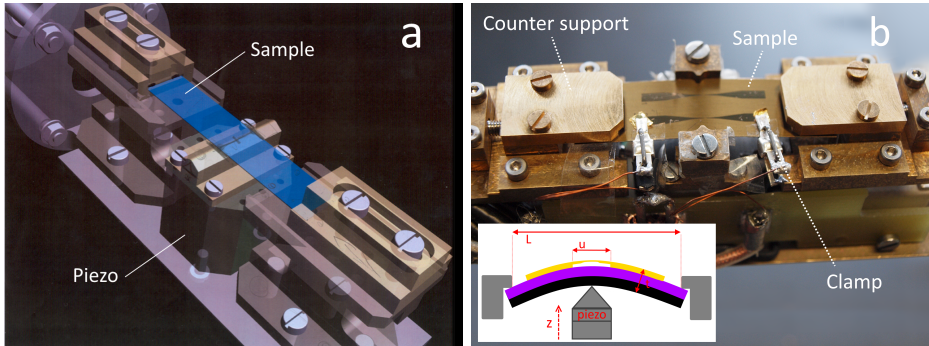


Figure 8: The sample holder for cryogenic break-junction experiments. a) Sketch for the construction of the sample holder, the piezo-positioner is located beneath the sample (blue). b) A photo of the sample holder with a break-junction sample connected by two clamps and fixed by metal plates at the ends. Additionally, small holders at the sides of the sample prevent movements to the side. Due to the dimension of the cryostat the diameter of the sample holder is restricted to 50 mm. The inset in b) shows a sketch of the working principle. The sample with thickness t and the underetched bridge with length u is bent by a piezo-positioner in the middle, while two plates separated by the distance L fix the sample at the edges.

A special sample holder is needed to arrange the piezo-positioner, counter supports, heater, temperature sensors and electrical connections and, at the same time, to provide enough space to bend the sample. The break-junction sample is mounted between the piezo-positioner and the counter supporters. The latter fix the sample in horizontal and vertical direction during the bending process. The distance between the counter supporters can be changed in order to adjust the maximum bending of the sample and thus the attenuation factor a , that describes the ratio between the lateral extension d of the nano bridge and the vertical displacement z of the sample. Four resistive heaters

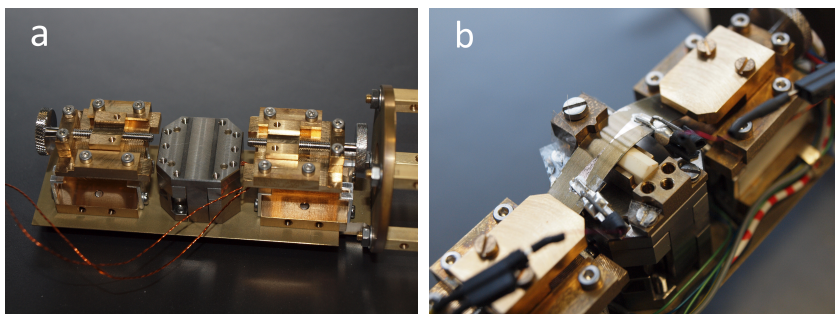


Figure 9: The heart of the sample holder is the sophisticated mechanical construction and the piezo-positioner (a). A lengthwise cut sample (width 0.8 mm) allows to observe the bending process in more detail (b).

and two temperature sensors allow an accurate control of the temperature of the sample in the helium-flow cryostat.

3.2 Electronic Setup

The electronic setup consists of the measurement circuit (voltage source and current measurement), the positioner for bending the sample, and the temperature control.

Measurement Circuit

Three different systems are tested in the framework of this thesis:

- A (self-made) voltage divider with a stable constant voltage source.
- A combination of a voltmeter (Voltmeter 2000, Keithley) with a voltage amplifier (DDCPA 300, Femto).
- A Source Meter Unit (2635B, Keithley), that applies voltages and measures currents at the same time.

In the first setup, the voltage source was not programmable and therefore not suitable for current-voltage curves (IVC), and in the second case voltage peaks during range switching of the receiver occurred and destroyed the sensitive nano bridge. Therefore, the third electronic setup was chosen for all measurements performed in this thesis.

The Source Meter Unit (SMU) has three major advantages regarding the measurement process. Firstly, the resistance measurement range is very large $10^{-3} \Omega \lesssim R \lesssim 10^{11} \Omega$, (i.e. the conductance regime $10^{-7} G_0 \lesssim G \lesssim 10^7 G_0$ which is necessary for our measurement)[7]. Fig. 11 shows the standard deviation of the SMU for different conductances measured at 0.1 V. Secondly, the voltage source and the measuring unit are combined in one device, i.e. they work at the same electric potential and the data recording is synchronized. Finally, the SMU is completely programmable, hence the desired automation of the setup could be realized. To optimize the measurement, several test runs were performed testing different wires, wirings, grounds and settings of the SMU (averaging, NPLC, filter and range settings).

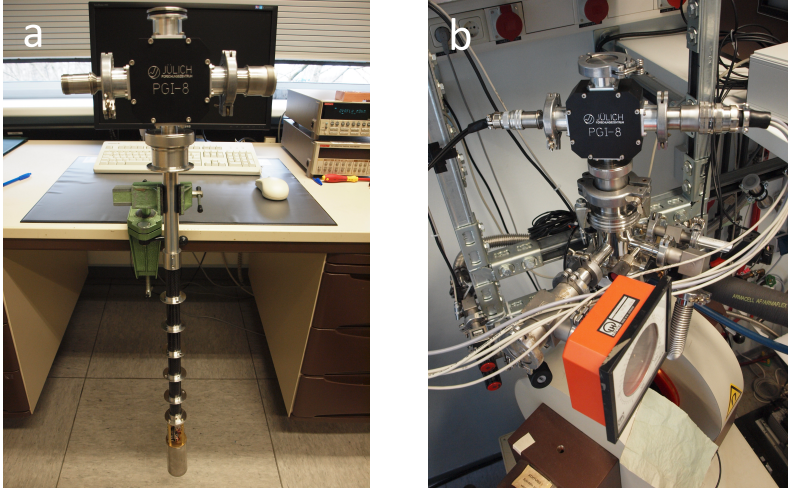


Figure 10: The sample holder, here inside the metallic cylinder at the lower part of the picture (see Fig. 9), is connected to a long carbon tube and further up to the head for the electronic connections (a). For measurements, the sample is placed into the helium-flow cryostat and electronically connected through the divider box (black) at the top (b).

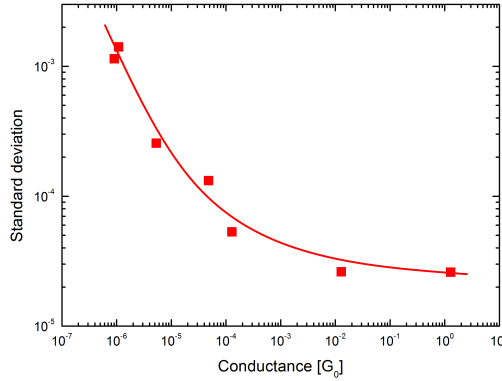


Figure 11: Accuracy of the SMU (Keithley 2635B) for different conductances in units of $G_0 \approx (13 \text{ k}\Omega)^{-1}$ for an applied voltage of 0.1 V. The standard deviation lies below one percent for conductances down to $G \approx 10^{-7} G_0$ (or resistances up to $R \approx 10^{11} \Omega$).

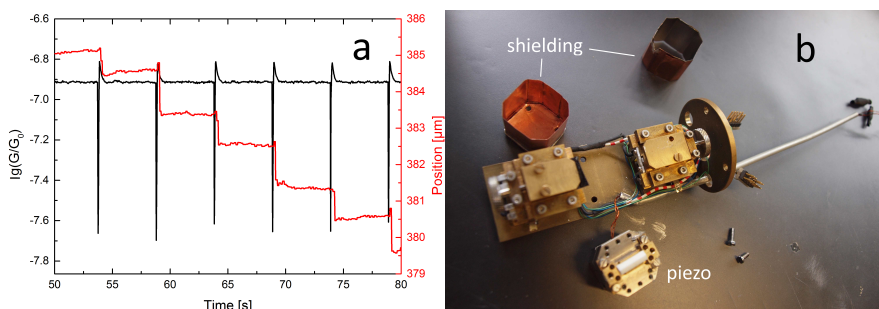


Figure 12: The movement of the piezo in the slip-stick mode is actuated by a tooth-saw shaped voltage. Without additional shielding (b), spikes appear in the signal of the break-junction if the position of the piezo is changed (a). With the additional shield this artifacts in the signal can be avoided.

To summarize, the programmable SMU provides resistance/conductance measurements over more than 10 decades. The data recording time (for one write and read command) is approximately 40 ms for high conductances up to 350 ms in the lower conductance limit of the device.

Positioner

The manipulator is responsible for the bending of the sample, and therefore a crucial part of the setup. In our case a piezo-positioner (Attocube, ANPz101/RES) with a size of $24 \times 25 \times 20 \text{ mm}^3$ and a maximum hub of 5 mm is used that fits in the sample holder, works at temperatures ranging from 10 mK to 370 K, and possesses an integrated reading (resistively) of the actual position. The piezo expands proportionally to the applied voltage (for low voltages) in the range of several hundred nm. To move the positioner over a larger range, a slip-stick motion is used that is based on a saw-tooth shaped applied voltage [1].

In the slip stick mode, the movement of the piezo consists of steps in the range of $z_{\text{step}} \approx 1 \mu\text{m}$, the exact step size depends on the maximum voltage of the tooth saw curve ($10 \text{ V} \lesssim V_{\text{max}} \leq 70 \text{ V}$). The step size, the time between the steps ($f_{\text{max}} \leq 100 \text{ Hz}$), and the load (maximal force of the piezo-positioner $F_{\text{max}} \approx 5 \text{ N}$) define the velocity of the piezo-positioner which can reach $v_{\text{max}} \approx 1 \text{ mm/s}$. A large number of test runs of the piezo-positioner (e.g. amplitude-, velocity- and frequency-stabilized movements) were performed at different temperatures in order to optimize the bending procedure.

Due to the working principle (slip-stick mode) a fast change of the high electric field (up to 70 V) is necessary. These large and fast voltage changes can affect the electric signal of the break-junction measurement. Subsequently, a metallic shielding around the piezo-positioner had to be developed to prevent this effects (see Fig. 12).

The piezo is the heart of the sample holder. The exact regulation and measurement of the position, with an accuracy below μm , allow a precise control of the bending process of the break-junction sample in the complete temperature range.

Temperature Control

Finally, a temperature controller (332 Temperature Controller, Lakeshore) four resistive heaters and two temperature sensors (Cernox) are used to set and control the temperature in the range of 4 K to room temperature. The sample is cooled down with liquid helium in the helium-flow cryo-

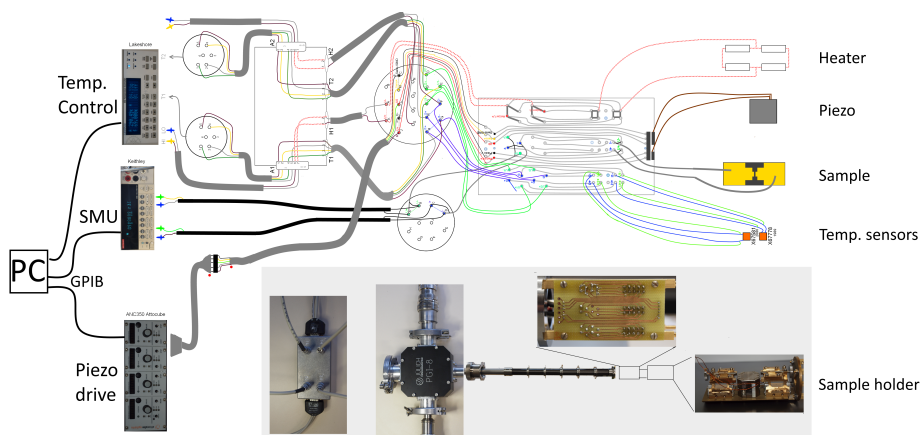


Figure 13: Sketch of the complete electronic setup for the MCBJ. Different devices are connected to the cryogenic sample holder, the temperature control for temperature measurement and heating, the SMU for applying a voltage and measuring the current, and the piezo drive for controlling the piezo-positioner.

stat and the two temperature sensors are placed close to the sample. Four heaters (i.e. resistances of 1 k Ω) are evenly located to adjust the temperature resistively.

SMU, piezo-positioner and temperature control provide a suitable setup for our cryogenic break-junction experiments, a sketch of the complete electronic wiring is shown in Fig. 13. All devices in the setup are fully automatized, as presented in the next chapter.

3.3 Automation

The setup is fully automated in order to control the experiment and read and analyze the data. The automation is performed with the programming software “Labview” and contains some important features. The data, among others applied voltage, measured current, temperature and piezo-position are set and/or recorded automatically. Furthermore, the data are analyzed while performing the measurements, e.g. conductance–position curves (CPC), current–voltage characteristics (IVC) and histograms are directly visible (see Fig. 14).

The major advantage of our self-written program is the ability to control every parameter individually in order to understand and to optimize the measurements. Generally, CPCs, IVCs and histograms can be recorded automatically for instance for different temperatures and even over night. All parameters like start and stop condition for a characteristic, voltage-, position- and temperature steps or repetition rates can be varied automatically within the physically or electronically allowed range. The basic structure consists of several parallel loops for the main tasks, which allow independent, and therefore faster, measurements and data acquisition.

Subsequently, the data are usually evaluated via the program “Origin”. After the analysis techniques were optimized, scripts were written to allow a fast and comparable analysis.

To sum up, the automation of the setup represents a crucial feature of the setup that is explicitly developed by us for this experiment. The ability to control and modify every parameter helps to find optimized procedures for the characterization of molecules. Furthermore, due to the complete automation of the devices, extended measurements can be performed, e.g. for several days and over-night.

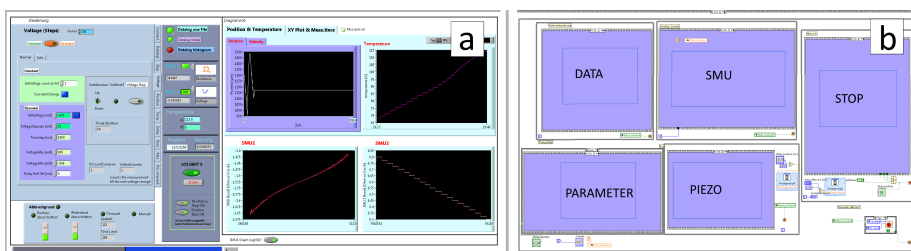


Figure 14: Labview program for the break-junction setup. (a) Screenshot of the working panel. All parameters of the measurement can be controlled and the results (CPC, IVC or histogram) are shown during the measurement. (b) Screenshot of the programming window. The basic structure consists of parallel loops (e.g. data acquisition, current and voltage measurements, piezo positioner) that operate independently to maintain a fast measurement procedure.

3.4 Sample Design and Preparation

The sample preparation represents another crucial part of the work. The nano bridge of the break-junction sample represents a rather delicate system, small deviations, e.g. of thickness and length, strongly influence the behavior. By optimization of the different process steps the success rate for a reliable operating break-junction could be increased from about 30% to 70%.

The fabrication process consists of nine steps (see Tab. 2). After cleaning, the sample is coated with two layers of polyimide. The polyimide serves as an isolating layer and allows a free-standing nano contact. A third layer of resist allows to write lithographically the structure onto the sample. After the development of the resist the metal layers (titanium and gold) are deposited, subsequently the Au structure with the nano-contact is obtained via a lift-off process. In a last step the nano contact is underetched in order to obtain the free standing Au nano contact. For an overview of the preparation process, see Tab. 2.

All steps except for the electron beam writing are performed in a cleanroom.

3.4.1 Preparation Steps

Substrate: The cryogenic break-junction experiment is based on a substrate, with a sufficient flexibility over the whole temperature regime from 10 K to room temperature, however, the substrate should not be too soft. Spring steel is relatively flexible compared to other metal substrates even at low temperatures. Therefore a spring steel substrate with a size of $44 \times 12 \text{ mm}^2$ and a standard thickness of 0.2 mm was chosen in the beginning. Thickness and width of the steel was optimized, to allow a reproducible bending of the sample with the commercial piezo-positioner (see Fig. 15). For instance the standard metal substrates (thickness of 0.2 mm) can be bent to the maximal position of $z_{\text{max}} = 5 \text{ mm}$ at room temperature. However, with decreasing temperature the velocity and the maximal z -position of the piezo-positioner continuously decrease. Different solutions for this problem have been tested:

- decrease of the width of the substrate,
- decrease of the thickness of the substrate, and
- the use of another substrate material.

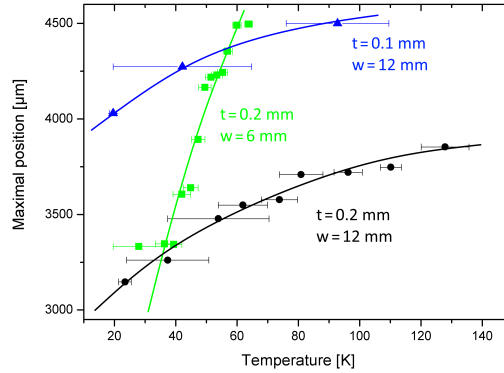


Figure 15: Temperature dependence of the maximal obtainable z -position of the piezo-positioner with a spring steel substrate of different width w and thickness t .

Fig. 15 shows the maximal position of the piezo-positioner for different temperatures and substrates. Both, a reduction of the width and the thickness of the substrate, change the temperature dependence of the maximal position. Although a smaller substrate (e.g. $w = 6$ mm) can easily be bent to the maximum position of the piezo-positioner down to 60 K, we decided to choose wider samples ($w = 12$ mm). These samples can be handled easier in the cleanroom and they allow to produce several nano contacts on one substrate (see discussion of the lithography below).

Furthermore, CuBe (copper-beryllium alloy) was tested successfully. However, this material cannot be processed in our cleanroom. Therefore, a spring steel substrate with a reduced thickness of only 0.1 mm was used for all fabricated samples.

Cleaning: In order to remove organic compounds (e.g. oil, that results for instance from the cutting step in the workshop) the metal substrate is cleaned in acetone and propanol and dried with nitrogen gas.

Polyimide Coating: The cleaned substrate is coated with polyimide (PI). PI serves as an isolating layer for the free standing nano contact. Additionally, its high elasticity contributes to a homogenous conversion from horizontal to vertical movement.

The sample is mounted on a spin-coater, and PI is deposited onto the sample at a rotation speed of 3000 rounds per minute (rpm), maintained for 30 s in order to achieve a homogeneous film thickness of approximately $6\text{ }\mu\text{m}$ (see Fig. 16). The film is baked on a heating plate at $90\text{ }^{\circ}\text{C}$ for 2 minutes, followed by a second heating at a temperature of $250\text{ }^{\circ}\text{C}$ for 20 minutes. Subsequently, a second deposition of PI is performed under the same conditions. The used PI-2611 (HD MicroSystems) consists of a polyimide precursor (based on biphenyldianhydride/1,4-phenylenediamine) that is dissolved in n -methyl-2-pyrrolidone (NMP). In the cured form the PI-2611 is resistant to acetone and alcohols and therefore suitable for the next preparation steps [4].

PMMA Coating: In order to obtain the Au nano contact on the PI, poly(methyl-methacrylate) (PMMA) solved in chlorobenzene is spin coated on the PI (30 seconds at 3000 rpm). PMMA 649.04 950K (Allresist) suitable for the following e-beam writing process is used. The sample is baked to cure the resist (95 seconds at $180\text{ }^{\circ}\text{C}$). The parameters, especially the baking time, are

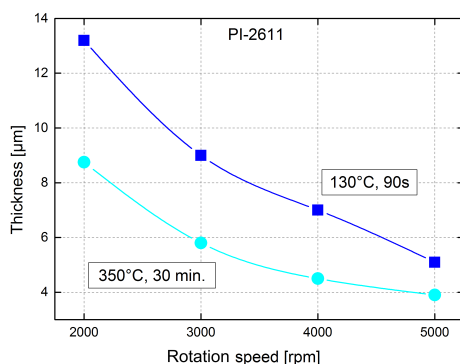


Figure 16: Thickness of PI-2611 layers as function of the rotation speed of the spin-coater during the PI deposition ([4]). In our case, the layer is deposited at 3000 rpm, and baked at 250 °C for 20 minutes. Therefore, the thickness is expected to lie between 6 – 9 μm .

optimized with regard to the thickness and quality of the PMMA layer. They deviate from the standard conditions [6].

Electron-Beam Writing: The “e-beam writer” consists basically of an electron source and different lenses to focus an electron beam onto the sample that is coated with e-beam sensitive resist (in our case PMMA). Where the incident electrons hit the resist, they cleave the main chains of the resist into fragments, which then can be removed in the development step. In this thesis an e-beam writer (VISTEC EBP 5000 plus) based on a field-emission source was used to write the structure onto the samples.

Several layouts with contact sizes ranging between 15 nm and 60 nm are designed using the programs “Autocat” and “Clewinn” and are transferred to the e-beam writer (see Chap. 3.4.3). The quality of the structure (especially the nano contact) strongly depends on the dose of the electron beam. A too small dose will have no impact on the resist, whereas a too large dose leads to unsolicited effects, like forward and backward scattering of the primary electrons (“proximity effect”). This leads to a statistical broadening of the electron beam and reduces the contrasts. Calculations of the dose and experimental tests of doses on different parts of the structure help to minimize unwanted effects and lead to optimized nano contacts.

Development: Subsequently, a development step removes the exposed parts of the resist. The sample is rinsed for 55 s in the developer AR-600-55 (Allresist)—the main component of the developer is methyl-isobutyl-ketone (MIBK) [6]—and immediately afterwards dipped into isopropanol to stop the development. The development step is very crucial for the fabrication process. Too short development time will remove just a part of the exposed resist. This finally leads to a sample with a reduced metal structure, whereas over-development leads to a broadening of the structure. In the latter case the junction might not be breakable in the setup.

Deposition and Lift-Off: The Au nano contact is completed by the deposition of the metallic layers to the polyimide structure. First a 2 nm–4 nm thick Ti layer is deposited onto the sample in order to guarantee a good adhesion. On top of the Ti layer an Au layer is deposited. Details of the deposition process are given in Chap. 3.4.2.

An acetone bath removes the remaining PMMA, including the Au layer on top of it, leaving just the exposed structure as a gold layer on the sample. This so called “lift-off” process usually takes a few minutes. However, for a lot of the samples the lift-off did not work properly. If the resist could not be removed with solely acetone, an ultra-sonic (US) bath (1 min., 50 Hz, 320 W) enables the lift-off. However, this process is critical, some of the structures were also destroyed in the US bath. As a substitute for the acetone a special chemical remover (Allresist, REM400) for the PMMA residues was tested, however, it did not improve the lift-off process. Hence the most of the samples experienced an acetone lift-off without US bath.

Etching: The last fabrication step is an etching step that establishes a free standing Au nano bridge. In “reactive ion etching” (RIE) a strong electric field ionizes a gas. The positively charged ions are accelerated towards the sample and remove a part of the polyimide layer. Due to the reactive component (working gas 20 mbar O_2/CH_3 , etching power 100 W, time 8 min.) only the polyimide and not the Au is affected. As a result, the nano bridge, the thinnest part of the structure, is underetched. The resistance of the resulting nano Au bridge provides an ideal characterization and control of the quality of the contact. An ideal bridge with $t \approx 30$ nm and $w \approx 30$ nm has a resistance $R \approx 200 \Omega$. Scanning Electron Microscope (SEM) images of optimized nano contacts are shown in Fig. 19.

Tab. 2 summarizes the preparation process for the break-junction samples. Photos, optical microscope pictures and SEM pictures of the samples are presented in Fig. 18, 19 and 20, respectively.

3.4.2 Au Deposition

Next to the patterning the quality and exact thickness of the Au layer represent the important parameters for a reliable, optimized and persistent operation of the break-junction. Different deposition techniques, magnetron sputtering and evaporation, are tested for the deposition of Ti and Au.

In sputtering positively charged ions bombard the target thereby removing atoms from the target and simultaneously creating free electrons. The electrons are accelerated towards the plasma creating new ions and, then, maintaining the process. By choosing the potential at the cathode the energy of the atoms that are forming the film can be controlled. The most important advantage compared to other deposition methods is the relatively large particle energy of sputter deposition that is controlled via the cathode potential. On the one hand one of the consequences is the good mechanical stability and adhesion of sputter deposited films. On the other hand in contrast to deposition processes with low particle energy more defects can be created during the sputter process. Furthermore, we found out, that the thickness of the Au layer at the nano contact strongly differs from the thickness of the larger Au areas, and therefore cannot be controlled very well. This should briefly be explained in the following.

Due to the resist pattern (thickness of PMMA $h \approx 170$ nm [6]) the deposition of the Au coming from the sputter track of the 4'' Au magnetron target is strongly reduced for small gaps. This can be illustrated by a simple simulation using ballistic particles (Au atoms) impinging on a narrow trench which is formed by the PMMA resist (see the sketch in Fig. 17). The result of such a simple simulation of the sputtered thickness in dependence of the width of the structure is given in Fig. 17. In this calculation a 30 nm wide structure in a 170 nm high resist is covered only by $1/6$ of the film compared to an extended structure. Furthermore it demonstrates why the exact thickness of the film cannot easily be controlled. Since the operation of the break-junction depends heavily










Step	Process			Sketch
1	Cleaning	a	Acetone	
		b	Propanol	
		c	Heating (90°C; 5 min.)	
2	Coating PI 2611	a	Spincoating (3000 rpm; 30 s)	
		b	Pre-heating (90°C; 120 s)	
		c	Heating (230°C; 20 min.)	
3	Coating PI 2611	a	Spincoating (3000 rpm; 30 s)	
		b	Pre-heating (90°C; 120 s)	
		c	Heating (230°C; 20 min.)	
4	Coating PMMA 649.04	a	Spincoating (3000 rpm; 30 s)	
		b	Heating (160°C; 90 s)	
5	Lithography	a	e-Beam writing	
6	Development AR-600-55	a	Dipping (55 s)	
		b	Propanol (stopping)	
7	Deposition Evap./sput.	a	Ti (2 nm)	
		b	Au (30 nm)	
8	Lift-off	a	Acetone (> 1 min.)	
		b	US-bath, (320 W, 1 min.)	
		c	Nitrogen gas	
9	Etching	a	Reactive Ion Etching (20 mbar O ₂ /CH ₃ , 100 W, 8 min.)	

Table 2: Steps of the fabrication procedure for a break-junction sample, the sketches illustrate the cross section (left) and top view (right) of the sample after the specific process. The different colors represent: grey–metal, purple–PI, bright green–PMMA, dark green–exposed PMMA, yellow–gold.

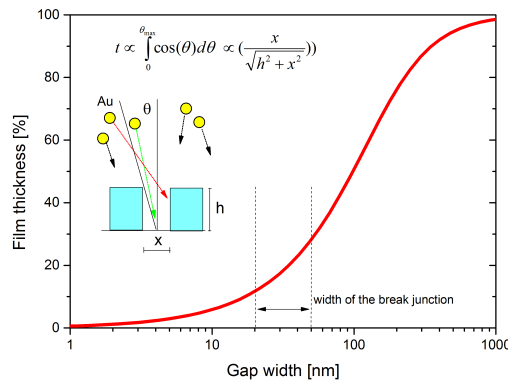


Figure 17: Simulation of the film thickness of a sputtered film as function of the gap width of a PMMA structure of thickness $h = 170$ nm. The sketch illustrates the situation of ballistic Au atoms arising at the PMMA structure, the dashed lines mark the regime of the gap width that is used in this thesis.

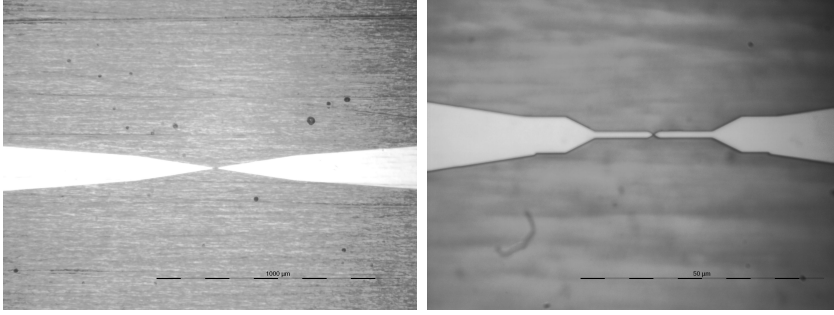


Figure 18: Optical microscope pictures (different magnifications) of the center of a typical break-junction sample. The nano-structure itself is placed in the middle of the structure, and it is not visible in an optical microscope.

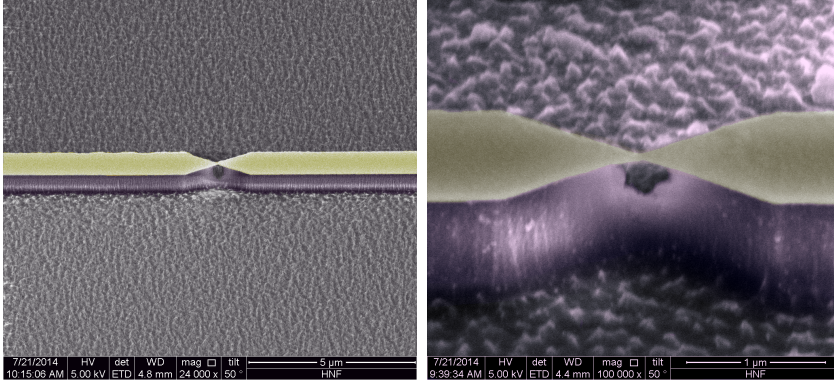


Figure 19: *Scanning electron microscope* (SEM) pictures of the nano contact of a typical break-junction sample. For clarity, gold was colored yellow and PI purple. The etching process removes the PI on places where no gold layer protects it. Since the thinnest part of the structure is the middle of the bridge, here an underetching takes place, which is clearly visible in the picture.

on the geometrical design of the bridge, this complicates the fabrication of the desired structure. Moreover, evaporated particles have a lower energy than sputtered particles, leading to a more homogenous film with fewer defects. Therefore, mostly the evaporation technique was used to deposit the two metal layers.

A crucial parameter for the optimal operation of the break-junction is the thickness t of the Au layer. Therefore, different thicknesses of the gold layer, ranging from 20 nm to 50 nm, are tested. For thin layers ($t < 30$ nm) the process is very unstable. Either the nano bridge, which is the thinnest part of the structure, is not continuously formed, or it is very sensitive, and thus destroyed during the mounting process. Moreover, samples with a thin gold layer generally show a relatively short lifetime in the measurement. In contrast, too thick layers ($t > 40$ nm) are not breakable in our setup (the maximal displacement of our piezo-positioner is $z_{\max} \approx 5$ mm). Therefore, the optimal thickness of the gold film turns out to be $t \approx 30$ nm.

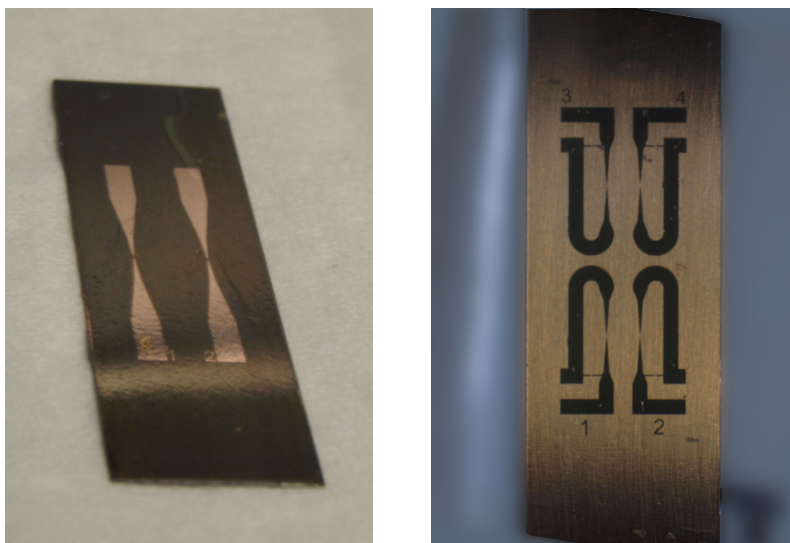


Figure 20: Photos of typical break-junction samples. On the left side a photo of a sample with two straight gold structures is shown, while on the right side a sample of the same size with four looped structures including a shunt is shown (see Chap. 3.4.3 for more information).

3.4.3 Design of the Break-Junction

For the structural design of the break-junction several programs are used, e.g. “Autocat” or “Clewinn” program. To improve various aspects of the experiment (e.g. reduction of noise, robustness during implementation and/or operation, redundancy) different e-beam structures were developed and tested. Since most of the changes are small, only two important variations of the basic structure are shown in Fig. 21. The simplest structure (Fig. (21 a)) consists of two tapered arms with contact pads on both sides. One structure has a length of $l \approx 600 \mu\text{m}$ and a width of $w \approx 100 \mu\text{m}$, respectively. The bridge is positioned in the middle of the structure and has a nominal diameter of 30 nm (see Fig. (21 d)). The width and length of the nano contact and the supporting structure nearby plays a major role for the break-junction operation. To optimize the structure, the geometry of the nano contact is varied, especially the width at the thinnest part, together with the thickness of the deposited Ti and Au layer.

In contrast, the design in Fig. (21 b) shows four (higher redundancy) identical patterns which have a number of interesting features. First, both connecting pads are on the same side of the bridge, resulting in a small loop. The motivation for this is the antenna like behavior of the connected system. Long gold structures with two connecting wires act as a loop, hence couple to electromagnetic fields that significantly can influence the measurement, especially for low conductances and therefore small measure currents. Second, additional shunts are added, that can simplify the mounting of the sample. Finally, the nano contact is moved away from the central position at which the piezo-positioner exhibits the force onto the sample to bend it.

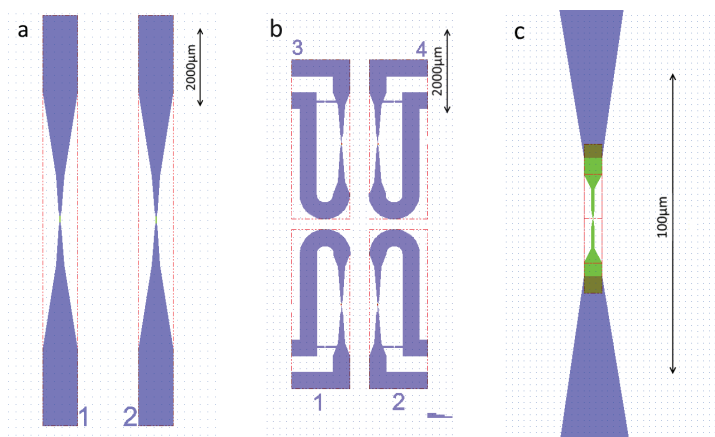


Figure 21: Lithographic structures for the break-junction, designed via the programs “Autocat” and “Clewlin”. The drawing is divided into two layers, a “fine-writing” (green) with a high resolution (< 2 nm) for the nano-structured bridge, and a “rough-writing” (purple) with a higher velocity but lower resolution (~ 50 nm) for the rest of the structure. Two different designs for the latter writing type are shown in (a) and (b). While (a) is the simplest type of break-junction, with two opposite big contact pads connected to the straight lines, (b) is more sophisticated. The two contact pads are placed near to each other, hence every structure forms a small loop. The reason is the antenna-like behavior of the connected junction. The fine structure (drawing c, green) is smaller than $30\text{ }\mu\text{m}$ and consists of the bridge and the connection lines.

3.5 Mounting the Sample

Mounting the sample turned out to be a crucial initial point of all experiments, since (i) any even small electrostatic pulse can easily destroy the nano bridge and (ii) the preparation of the molecules under test can be quite challenging. After preparation the sample is mounted on top of the piezo-positioner. Two counter supports at the ends fix the sample for the bending process and hinder the movement to the sides. The structure can be contacted electrically in several ways, particularly the electric charge of the first contact can easily destroy the nano structure on the sample (Fig. (24 a,b)). Two types of contacting the nano bridges are used in this thesis:

(i) Small clamps (isolated on one side) are mechanically clamped onto the contact pads. Silver paste and gold foil are tested to improve the contact, since bending the substrate sometimes leads to movement and disconnection of the clamps. The advantage of the use of the clamps is the easy and reproducible (de-)contacting and the fast connection without any delay, e.g. drying time. However, the clamps have disadvantages. Firstly, it is difficult to close the clamps carefully, since the size has to be small enough to fit into a cryostat. Secondly, particularly at low temperatures the connection becomes unstable during bending of the substrate. Additionally, before the clamps contact the structure a shunt has to be implemented. The first clamp is grounded and clamped onto the first structure pad. A shunt between the two clamps is established before the second clamp is connected. This assures that the same potential is present at both sides of the structure. Subsequently, before the shunt is removed it protects the nano structure during the connection to the measurement device (SMU), see Fig. 22.

(ii) Thin wires are placed below adhesive tape pieces onto the contact pads. Holes in the tape allow to glue the wire with silver paste to the pad. Again the possibility to “burn” the lithographic structures has to be taken into account, especially when attaching the tape to the structure. Tape

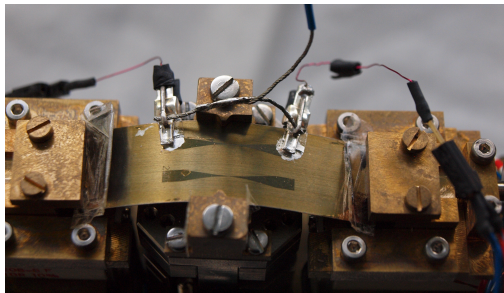


Figure 22: The sample is connected with clamps (and silver paste) at the contact pads. In case of electrostatic charge flow, when the measurement device is connected, a shunt between the two clamps protects the structure from damage. The silver paste improves the electrical contact between the Au structure and the clamps.

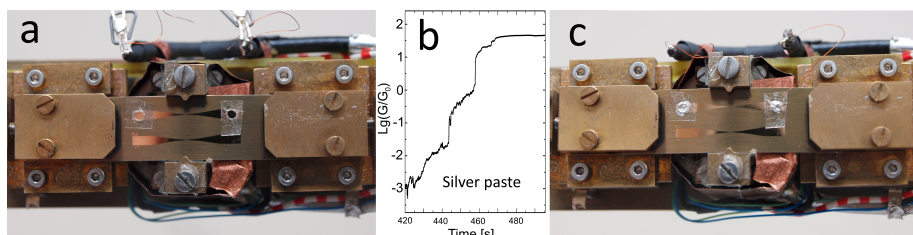


Figure 23: Mounting procedure for the break-junction sample into the sample holder. Firstly, two small pieces of adhesive tapes with drilled holes are carefully attached to the contact pads (a). Electrostatic charge in the adhesive tape has to be compensated before attaching, otherwise the fine-structure of the sample can be destroyed. The same compensation is necessary for the measurement wires, for this reason different shunts are introduced. The wires are placed below the tape and silver paste is filled into the drilled holes to ensure a permanent electrical contact. The tapes hinder the silver paste to spread over the sample and stabilizes the wires until the paste has dried. In the liquid form the silver paste is nearly isolating, in the hardened form it is highly conducting. The change of the measured conductance with time by contacting a closed break-junction sample with silver paste is shown in (b). This effect establishes slowly an electrical connection, especially in the case of contacting the sample without clamps (c).

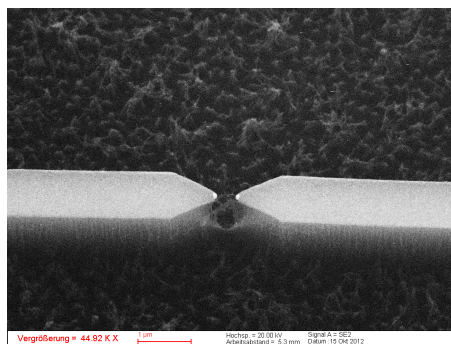


Figure 24: If the mounting process is not done carefully the electrostatic charge flow evaporates the nanostructure and no current can flow through the junction. The two remaining tips appear to be melted.

and wires are grounded before putting it to the sample until the wires are connected to the sample. The advantage of the second method lies in its mechanical stability. Furthermore, the electrical connection between the measurement system (SMU and wires) and the sample is gradually established (it takes several minutes for a drop of the silver paste to harden and, thus, become finally conducting). In the liquid form the silver paste is nearly isolating, while in the dry form a metallic connection is established (see the inset in Fig. 23).

Finally, for the measurement of molecules a solution with the desired molecules is prepared. Depending on the molecule, different solvents (methanol, ethanol, dichlormethan, chloroform and chloroform with pyridine) and different concentrations are tested. For instance the best conditions for hexanedithiol were obtained for ethanol and 2 mM and for porphyrine for chloroform and 0.05 mM. Optical tests and proton NMR are used to analyze the solubility, see appendix B. All break-junctions are tested in the cryostat before depositing molecules on them, therefore the deposition takes place on the mounted and connected sample. A small drop of the solution is carefully placed with a pipette on the junction in the middle of the sample. If the volume in the pipette is too large, it will spread over the sample, and contaminate all parts of the setup or dissolve the silver paste. A too small volume in the pipette does not allow to deposit one single drop. In this thesis, a volume of 16 μl was used. After the solvent is evaporated the sample is placed in the cryostat at low pressure to evaporate remaining solvent and possible liquid contamination. The cryostat is flooded several times with He and pumped for cleaning.

The preparation of porphyrines turned out to be problematic. Porphyrines show a tendency to cluster to large structures. For high concentrations of the solution, (~ 2 mM) in chloroform, large structures can be observed on parts of the gold surface in the SEM pictures (see Fig. (25 c)). However, even at intermediate concentrations (~ 0.2 mM) or low concentrations (~ 0.05 mM) small clusters are sometimes observed in parts of the SEM pictures (see Fig. 25).

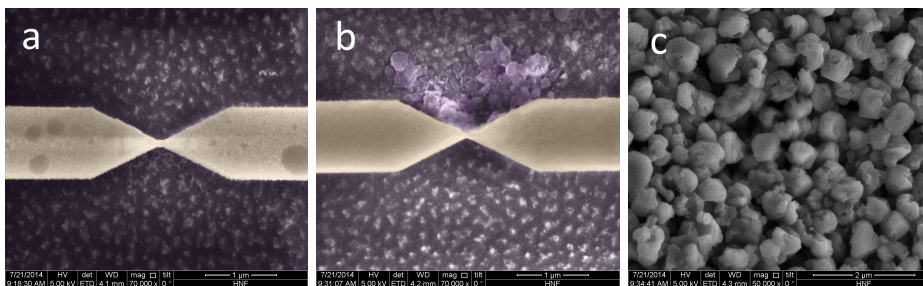


Figure 25: Porphyrines seem to cluster when deposited onto the sample. A SEM picture (magnification 70,000; colored) of the nano bridge without porphyrines is shown in (a), while (b) shows a SEM picture (colored) of the bridge with porphyrines (0.2 mM). (c) The clustering is clearly visible in the SEM picture (magnification 50,000) if porphyrines are deposited in relatively high concentrations (2 mM in chloroform). However, it has to be noted, that these structures only partially cover the surface.

4 Results and Discussion

4.1 Reference Measurements

The main purpose of our mechanically controllable break-junction experiments is the electronic characterization of single molecules. In order to understand these experiments, we first have to understand the behavior of the gold bridge itself. Bending velocity, applied voltage, and temperature affect the breaking process. Even at defined conditions each (dis-) connection of the tips can be different. In order to interpret the data of the molecules, various reference measurements are performed for gold bridges before molecules are deposited.

In the following chapters two basic measurement techniques, conductance–position characteristics (CPC, see Chap. 4.1.1) and current–voltage characteristics (IVC, see Chap. 4.1.2) with the corresponding analysis are introduced and demonstrated for gold bridges without molecules.

4.1.1 Conductance–Position Characteristics

An optimized lithographically prepared break-junction sample has an electrical resistance of about $200\ \Omega$ or a conductance of about $5\ \text{mS}$. For standard conductance measurements, a constant voltage (e.g. $50\ \text{mV}$) is applied using a Source Meter Unit (SMU).

Generally the resistance of the break-junction depends on the lateral elongation d of the Au contact which is controlled by the z -position of the piezo-positioner (see also Fig. 30). By bending the sample the junction gets thinner and the resistance increases, relaxing the sample leads to the opposite effect (see Fig. 27). Nevertheless, breaking and closing the junction are different procedures.

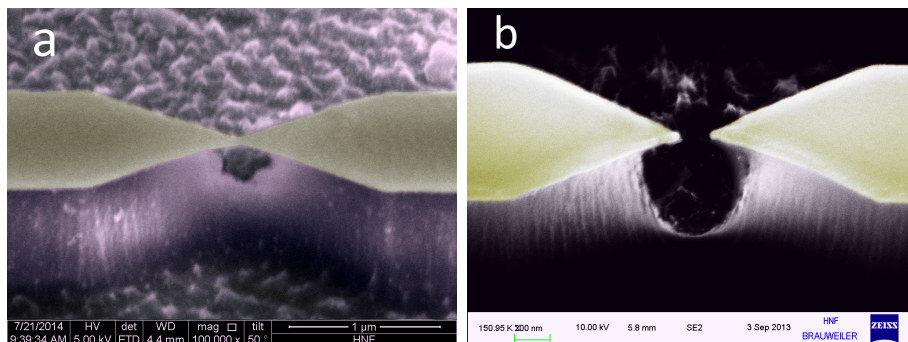


Figure 26: Colored scanning electron microscope (SEM) pictures of a closed (a) and an opened (b) break-junction.

Let us start with the first step, the breaking of the junction which is shown in detail in Fig. 28. Starting with a bridge of finite size (sketch (a) in Fig. 28) the bending leads to a reduction of the cross section of the Au junction (sketch (b) in Fig. 28). Finally the junction approaches the atomic size (sketch (c) in Fig. 28) and the cross section cannot shrink continuously anymore. The resistance of this single atom contact is approximately $13\ \text{k}\Omega$, the so-called quantum of conductance G_0 (see Chap. 2.1) which represents the conductance ($77.5\ \mu\text{S}$) of the smallest possible metallic

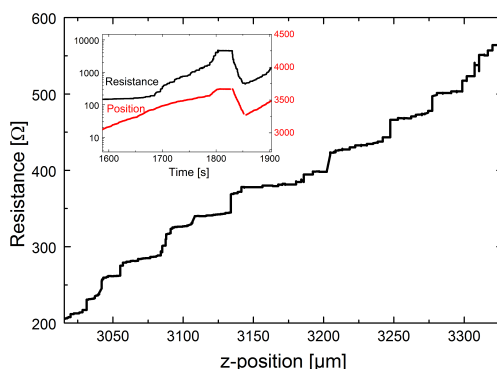


Figure 27: The resistance of a break-junction depends on the position of the piezo-positioner. The inset shows the measured resistance (black circles) of a closed break-junction and the position of the piezo-positioner (red squares) versus the time.

contact. Due to the ductile behavior of the gold [14] further bending pulls out a chain of gold atoms (sketch d in Fig. 28) which does not change the conductance and thus leads to a plateau in the CPC (Fig. 28). This plateau at the quantum of conductance is significant for all break-junction experiments and is often used for calibration of the experiment.

If the sample is bent further, finally the Au-chain breaks (sketch (e) in Fig. 28), the plateau in the CPC ends and the conductance starts to decrease exponentially with the distance between the remaining tips of the two Au contacts. The exponential decay is indicative for vacuum tunneling as conduction mechanism (Eq. 16). Often the rupture of the bridge is accompanied by a jump in the conductance, which indicates that after the breaking the two remaining parts of the Au-chain relax and thus instantaneously form a tunnel contact with a large gap (cf. the dashed line in Fig. 28 I). The jump in the conductance is observed in nearly all of our experiments. Only in the case of very slow and careful bending and for some molecular experiments a continuous CPC was observed. Since the gold atoms arrange randomly, the form of the surface is different for each breaking process. In our experiments the tunneling behavior is continued until the conductance reaches the limit of the sensitivity of our measurement at about $10^{-6} G_0$ to $10^{-7} G_0$. Here, the movement of the piezo-positioner is automatically stopped and after a small pause reversed in order to close the junction again. Fig. 26 shows SEM pictures of a closed and an opened break-junction.

The closing CPC of break-junction samples in general shows the same behavior as the opening CPC, i.e. an exponential dependence of the conductance of the z-position. However, in contrast to the opening characteristic, they exhibit a more recognizable and stable slope in the tunneling regime because no rearrangement of Au atoms takes place before the two gold tips connect again and close the junction. Fig. 29 shows three exemplary CPCs for closing curves. In the next chapter those CPCs are used to evaluate the attenuation factor.

Since it is unlikely to trap a molecule between the two contacts during the relaxation of the sample and since this would not lead to an extended plateau in the CPC, the closing CPCs are not suitable for characterizing single molecules.

4.1.1.1 Attenuation Factor

The principle and advantage to measure single molecules with a break-junction setup is given by the ability to control the distance between the two gold electrodes in the pm regime. The exact

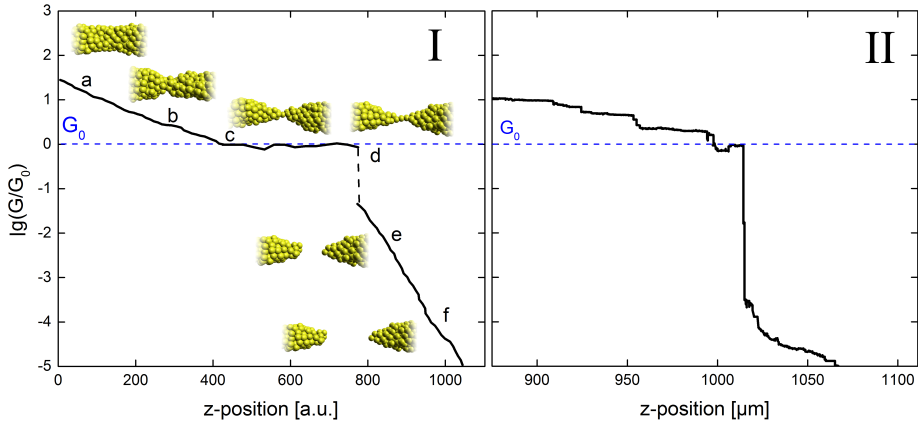


Figure 28: "Breaking process" of a MCBJ without molecules, the logarithmic conductance in units of G_0 is plotted versus the piezo-position. (I) shows a sketch of the CPC, while in (II) a measured CPC is presented for comparison. By bending the substrate vertically the gold structure is stretched horizontally and the conductance decreases nearly continuously (a,b) until G_0 is reached (c). At this point a gold chain is created by pulling the tips further apart, and the conductance stays constant (d). After the rupture vacuum tunneling dominates the conductance (e,f), i.e. the conductance decreases exponentially with increasing position of the piezo-positioner. Often after the rupture the two remaining tips rearrange fast (dashed line), hence the conductance jumps to a value far below G_0 before exponential tunnel decay starts.

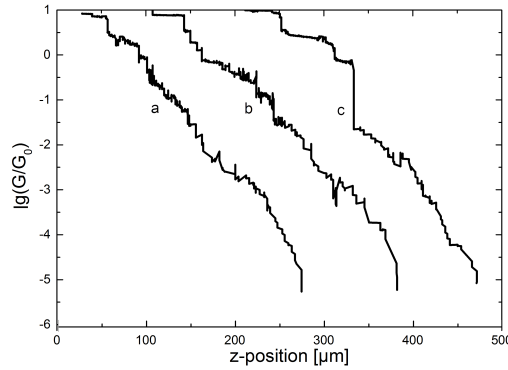


Figure 29: Three different CPCs for closing of the MCBJ (the CVCs are shifted horizontally for clarity). In contrast to the opening process, a more or less stable exponential increase of the conductance with decreasing position is observed for the closing process. Only in some cases the bridge shows a spontaneous, fast contraction to G_0 (c).

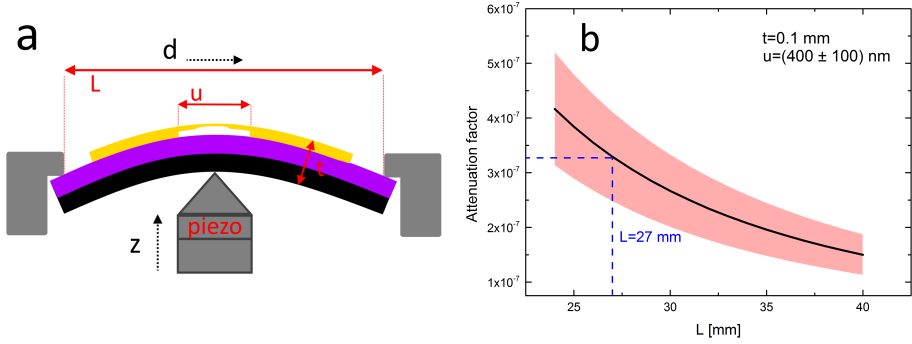


Figure 30: The working principle of the MCBJ is based on a translation from the vertical movement (in the z -direction) to a horizontal movement (in the d -direction) with a geometrically defined “attenuation factor”. The sample with thickness t is fixed at the two sides (distance L). The underetched part of the gold structure (with the length u) is stretched in the direction of d , by bending the sample in the z -direction (a). The attenuation factor describes the ratio of the two movements: $a = \Delta d / \Delta z$ and can be calculated according to Eq. 26. L , the distance between the counter supports can be easily adjusted to control the attenuation factor of our setup (black line in b). For $t = 0.1$ mm and $u = 400$ nm the standard distance of $L \approx 27$ mm gives an attenuation factor of $a_{\text{geom.}} \approx 3.3 \times 10^{-7}$. The red area in b indicates the range of the attenuation factor for $300 \text{ nm} \leq u \leq 500 \text{ nm}$.

control depends on the geometrical “attenuation factor” of the setup. A movement of the piezo-positioner leads to a modification of the lateral extension d , since the ends of the sample are fixed via counter supports (see Fig. 30 a). The ratio of the lateral movement Δd of the gold tips versus the vertical movement Δz of the positioner provides the attenuation factor [63, 60]:

$$a_{\text{geom}} = \frac{\Delta d}{\Delta z} = \frac{6ut}{L^2}, \quad (26)$$

where u is the length of the underetched gold bridge, t the thickness of the substrate and L the length of the substrate between the two counter supports (see Fig. (30 a)). In our case, $t \sim 0.1$ mm and $u = (400 \pm 100)$ nm. We obtain a geometrical attenuation factor depending on the distance L between the counter supports, that can vary from 25 mm to 40 mm. In most experiments a distance of $L = 27$ mm. Thus, the theoretical attenuation factor is

$$a_{\text{geom}} \approx (3.3 \pm 0.8) \times 10^{-7}. \quad (27)$$

An experimental way of estimating the attenuation factor utilizes the tunnel current between the two gold electrodes. If the junction is separated by the distance d in vacuum, the current depends approximately exponentially on the distance (see Chap. 2.3):

$$I = C_1 \exp(-2.6 \times 10^{19} \sqrt{\Phi} d), \quad (28)$$

where C_1 is a constant, Φ is the work-function and d is the distance between the tips. In a logarithmic plot of the current versus the distance, we get a linear behavior with the slope δ .

$$\lg(I) = C_2 - 2.6 \times 10^{19} \lg(e) \sqrt{\Phi} d = C - \delta d, \quad (29)$$

where C_2 is a constant. For vacuum tunneling from gold, the work function is $\Phi \approx 4.8 \text{ eV} \approx$

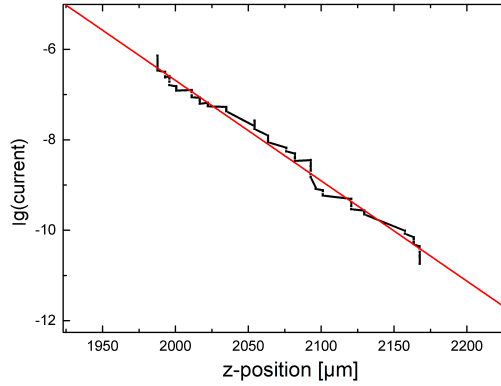


Figure 31: Logarithmic plot of the current versus the piezo-position of a closing CPC without molecules. For the closing curve the linear fit yields $m_{\text{clos}} \approx (-22.18 \pm 0.28) \times 10^{-3} (\mu\text{m})^{-1}$, i.e. an increase of the piezo position of approximately $100 \mu\text{m}$ leads to a decrease of the current of one order of magnitude. From the slope the attenuation factor a_{tunnel} of the setup can be estimated (see Eq. 31).

$7.69 \times 10^{-19} \text{ J}$ [3, 31]. Therefore the theoretical expected slope is

$$\delta \approx 9.9 \times 10^9 \text{ m}^{-1} = 0.99 \text{ \AA}^{-1}. \quad (30)$$

The experimental slope can be obtained from the CPC (see Fig. 31). The resulting experimental attenuation factor is the given by the ratio of both slopes:

$$a_{\text{tunnel}} = \frac{m_{\text{CPC}}}{\delta}. \quad (31)$$

As already mentioned in the previous chapter, closing curves are suitable for this calculation. With a linear fit of a closing CPC, Fig. (31 a), the attenuation factor of our setup is :

$$a_{\text{tunnel}} \approx \frac{(22.2 \times 10^3) \text{ m}^{-1}}{(9.9 \times 10^9) \text{ m}^{-1}} \approx 2.24 \times 10^{-6}. \quad (32)$$

The values for a_{geom} and a_{tunnel} differ by one order of magnitude. One should bear in mind that both attenuation factors are only rough estimations. Eq. 26 is based on simplified Lagrange methods and it depends strongly on the length u of the underetched bridge. Also the second calculation, Eq. 32, based on the tunnel-current is an approximation. It uses the mass m_e of a *free* electron and the work function $\Phi_{\text{Au}} \approx 4.8 \text{ eV}$ [3] of *bulk* gold. However, work function and effective mass of the electron of a randomly formed gold-tip might differ from that of a flat surface.

Nevertheless, both estimations yield reasonable values around 10^{-6} and demonstrates the possibility of controlling the gap between the Au tips, on the pm scale, suitable for single molecule experiments.

4.1.1.2 Histogram

A statistical way of analyzing the data obtained by the CPCs is given by histograms and contour histograms. In case of a “classical” histogram all conductance values within a certain conductance interval (bin) are counted. Typically a large number (>100) of CPCs of the breaking event of the junction are analyzed. Thus, the resulting histogram summarizes the CPCs, and allows to identify

the plateaus, e.g. caused by the Au chain and the molecules, on a statistical basis [67].

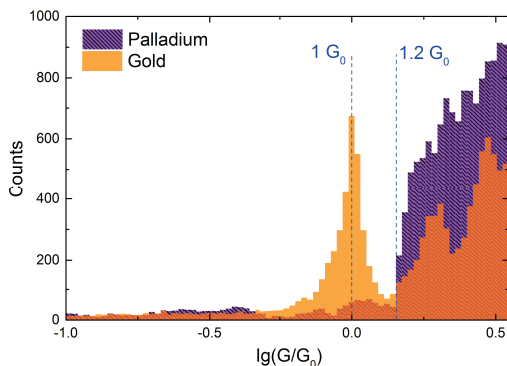


Figure 32: Comparison of a Pd (purple, striped bars) and an Au bridge (orange bars). Both bridges are sputtered with the same thickness and the CPCs are measured under similar conditions and show a strong decrease in the number of conductance values with decreasing conductance. However, the more ductile Au shows a clear peak around $1 G_0$, whereas the conductance of Pd just decays without forming a plateau, hence no peak is observed in the histogram.

Fig. 32 shows a comparison of a histogram taken for a MCBJ made from gold (Au) and palladium (Pd). Due to the specific properties of Au (especially the ductility) the atoms rearrange in the bending process. Immediately before the regime of vacuum tunneling Au forms chains and thus shows relatively reproducible and stable conductance plateaus in its CPCs. These plateaus turn out to be almost exactly at the quantum of conductance, and therefore form a clearly visible peak at G_0 in the histogram. In contrast, no peak at the quantum of conductance is visible for Pd, i.e. Pd break-junctions separate without pulling a chain of Pd atoms out of the electrodes. Therefore only a strong decrease at about $1.2 G_0$ is measured, see Fig. 32. As described in Chap. 2.1, the ability to extract chain-like structures of atoms from the electrodes is an essential feature for the identification of molecules in break-junction measurements. Only in this case the molecule can create a plateau in the CPC and, thus, can be identified. Therefore, in this thesis Au is used as material for the junction.

In a typical MCBJ experiment the conductivity is recorded over several orders of magnitude, in our setup down to typically $10^{-6} G_0$. As a consequence, the measurement device (SMU) uses different settings to cover the complete range. As a consequence a range switching of the SMU is visible in form of minima in the histograms (Fig. (33 a)). To proof that the minima are caused by the switching of the range of the SMU different voltages are applied. Fig. (33 b) shows two histograms recorded under the same conditions with 50 mV and 150 mV, respectively. The minima are shifted, i.e. the real dependence should be given by the “envelope” of both histograms.

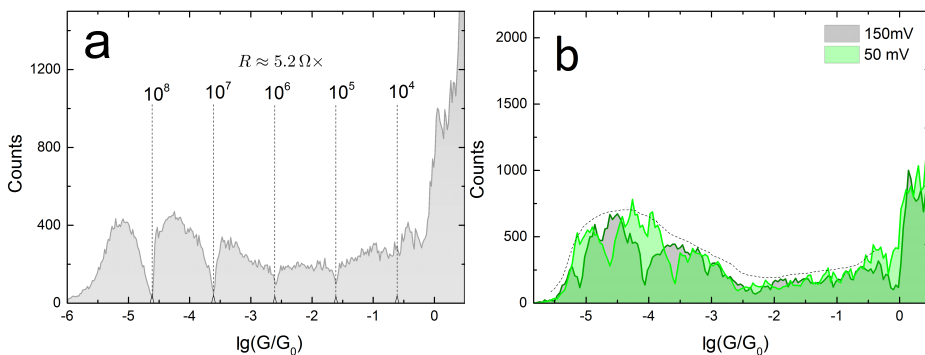


Figure 33: Histograms of the opening curves of an Au bridge. (a) For each voltage decade the recording device (SMU) changes the range (here at resistances of $5.2 \times 10^4 \Omega$). Since during this switching no data is recorded, sinks are visible in the histogram. The lower the conductance, the stronger the influence of the range switching. (b) Two histograms of the opening curves of an Au bridge, recorded at different constant voltages of 50 mV (grey) and 150 mV (bright green). Since the SMU records the resistance of the junction, a change of the applied voltage leads to a shift of the minima caused by range switching of the SMU.

4.1.1.3 Contour Histogram

The advantage of the use of histograms lies in the use of statistics. A single CPC might include a clearly pronounced plateau that might be indicative for a molecule, whereas the next CPC might show only vacuum tunneling or another plateau (e.g. another arrangement of the Au-molecule-Au contact). Statistically summarizing all CPCs should then help to visualize the or several molecular conductance level(s). Theoretically, this concept should be applicable to every molecular break-junction experiment. However, in practice the standard histogram turns out to be only useful in some cases and the method has its limitations, especially in the case of MCBJ experiments with molecules.

Therefore, in this thesis a modified histogram, a “contour histogram” is introduced to analyze CPCs. All opening curves are plotted in a conductance–position diagram, and a color code indicates the density of data points in a certain area that is defined by a given bin size for position and normalized conductance in logarithmic units. Two examples of contour histograms for a MCBJ experiment without molecules, are shown in Fig.(34). Generally, the same features are visible that also appear in the standard histogram. The data density around the quantum of conductance G_0 is high. Due to the rearrangement of the Au atoms directly after the rupture of the bridge, the density of data points is relatively small in the conductance range from G_0 to $10^{-3} G_0$. In the conductance regime below $10^{-3} G_0$ minima occur due to the “range switching” of the SMU. The higher the velocity, the more pronounced the range switching of the device, but the effect occurs even at a very small bending speed of $v_{\text{piezo}} \approx 1.5 \mu\text{m/s}$.

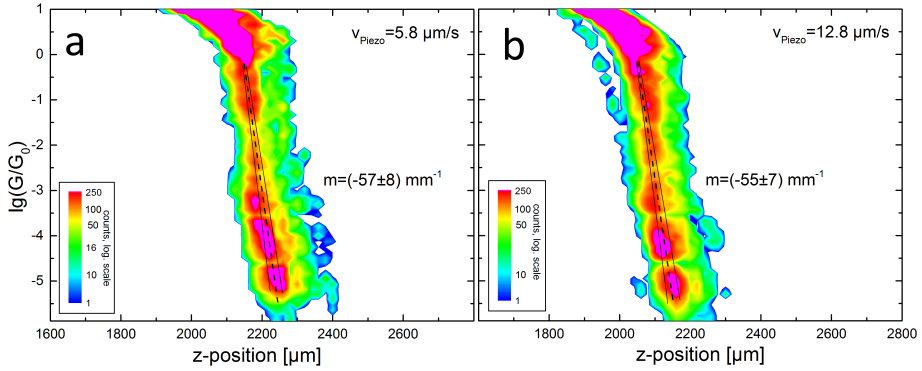


Figure 34: Contour histograms of opening CPCs without molecules recorded with different bending velocities of the piezo-positioner. Note that the piezo velocities do not change the slope. The color code allows to distinguish the breaking around G_0 and the switching of the range in the lower conductance regime. As expected, the minima in the histogram (cf. Fig.(33)) are more clearly pronounced for faster breaking, as expected. For the histograms 120.000 data points and a bin size of $20\text{ }\mu\text{m} \times 0.12$ was chosen, which is the standard for this thesis. The slope m of the histograms are $(-57 \pm 8)\text{ mm}^{-1}$ and $(-55 \pm 7)\text{ mm}^{-1}$, respectively.

The advantage of this new type of histogram lies in the additional information, i.e. the *position* at which a large number of signals are detected which later helps to detect molecules in the break-junction. Moreover, the contour histograms yield averaged slopes of $m \approx -(55-57)\text{ mm}^{-1}$ in Fig. 34, i.e. for 1 mm displacement the conductivity would change more than 50 orders of magnitude. These slopes differ clearly from those of the *closing* CPCs of the same measurement, with $m \approx -(23-24)\text{ mm}^{-1}$ (see Fig. 35).

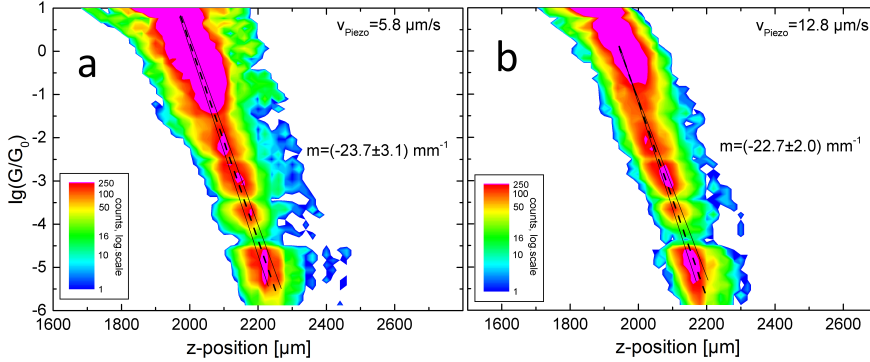


Figure 35: Contour histograms of closing CPCs without deposited molecules recorded with different bending velocities. Note that the breaking velocities do not change the slope of the histograms, which are $m_{a,\text{closing}} \approx (-24 \pm 3)\text{ mm}^{-1}$ and $m_{b,\text{closing}} \approx (-23 \pm 2)\text{ mm}^{-1}$. The corresponding contour histograms of the opening CPCs exhibits more than two times larger slopes (see Fig. 34).

In the closing CPCs a relatively stable and reproducible system is expected, whereas rearrangement of Au atoms after the breaking leads to a more complicated system in the case of opening CPCs. Therefore, closing CPCs provide a more reliable attenuation factor. However, later on we will compare the decay constants from opening contour histograms with molecules with those for

vacuum tunneling. For this reason a different attenuation factor $\tilde{a}_{\text{tunnel}}$ for the opening CPC is introduced:

$$\tilde{a}_{\text{tunnel}} \approx \frac{(56 \times 10^3) \text{ m}^{-1}}{(9.9 \times 10^9) \text{ m}^{-1}} \approx 5.66 \times 10^{-6}. \quad (33)$$

By using this attenuation factor for the opening contour histograms, we obtain a decay constant $\delta \approx 1 \text{ \AA}^{-1}$ for vacuum tunneling (see Eq. 30).

4.1.2 Current–Voltage Characteristics

Definitely, the most important tool for the electronic characterization of single molecules is given by current–voltage characteristics (IVC). For the reference measurements (i.e. without molecules) the IVC should show a linear dependence for not too high voltages.

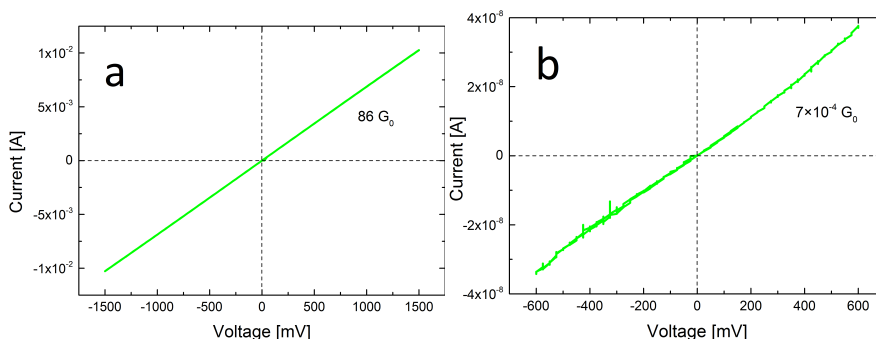


Figure 36: IVCs of a closed bridge at room temperature (a). The slope of the curve defines the conductance ($86 G_0 \approx (150 \Omega)^{-1}$) and is constant over the whole range. (b) A similar IVC of a tunnel junction after the electrodes are separated. At higher voltages the measurements without molecules become unstable, for instance the Au electrodes connect spontaneously due to the high electric field. The slope of the curve equals a conductance of approximately $7 \times 10^{-4} G_0$.

Fig. 36 shows typical IVCs for a break-junction sample before and after breaking. Both IVCs show a more or less Ohmic behavior. Obviously the closed junction (Fig.(36 a)) is more stable, i.e. less noise and deviation from the linear behavior are visible, whereas for the open junction (Fig.(36 b)) larger noise and deviation from the linear behavior appear to be visible. However, it has to be taken into account that the sensitivity of the latter measurement is about 6 orders of magnitude better than that for the closed junction. Nevertheless, tiny changes in the arrangement and distance of the atoms, for instance caused by the modification of the voltage between the tips, influence the tunnel current. Furthermore, high electric fields can even spontaneously close the junction. IVCs recorded with molecules turn out to be often more stable than those without molecules. In this case the IVCs show a non-linear dependence, which can be used to obtain characteristic properties of the molecule, e.g. energy levels of orbitals. The different analysis techniques for those IVCs are presented in Chap. 4.3.

4.2 Characterization of Molecules

In this chapter we first briefly introduce the basic principle of MCBJ experiments on single molecules, i.e. conductance–position and current–voltage characteristics, and sketch different methods of interpretation of the experimental data.

4.2.1 Characterization Methods

Similar to the reference measurements, for the characterization of single molecules with break-junction experiments, conductance–position characteristics (CPC) and current–voltage characteristics (IVC) are used. In general, the analysis of the CPCs (i.e. CP plot, histogram and contour histogram) is similar to the measurements of junctions without molecules (see Chap. 4.1).

However, some differences that occur for CPCs with molecules are shown in Chap. 4.2.1.1. Finally, Chaps.(4.2.1.2–4.2.1.5) provide an overview of the different analysis techniques used for IVCs of molecules.

4.2.1.1 Conductance–Position Characteristics

Generally two different CPCs can be obtained for MCBJ experiments with molecules:

- If no molecule is trapped between the tips of the two electrodes during breaking of the nano contact, the CPC is identical to that of a reference measurement without molecules (note that tunneling currents via molecules can be neglected in this case).
- Only if a molecule is trapped between the contacts, the CPCs differ from that of the reference measurement.

As we will see in the experiments, both options occur in MCBJ experiments with molecules. In the following we will only discuss the latter case, illustrated in Fig. 37.

In the beginning of the bending process a CPC similar to that of the reference measurement is obtained, since the molecule does not contribute significantly to the electron transport (see Fig. (37 g,h)). After breaking of the Au nano contact the conductance decreases exponentially, since tunneling dominates the current. Contributions of the current through the molecule can be neglected. However, at some point a molecule might be trapped between the Au tips, see Fig. (37 i). The current is then defined by the current through the molecule, i.e. it is defined by the two Au-molecule bonds and the electronic properties of the molecule itself. If the Au-molecule bonds are strong enough, the molecule pulls out a chain of Au atoms, hence further bending does not change the conductance (see Fig. (37 j)), i.e. similar to the procedure at the quantum of conductance a plateau appears at the conductance G_m , that defines the Au-molecule-Au conductance. The probability and extension for a molecular plateau to occur depends on the properties of the specific molecule (e.g. strength of the Au-molecule bond and flexibility of the molecule).

The most important role play the anchoring groups of the molecule which have to connect to the Au atoms. The stronger the bond to Au, the better the ability to extract an Au chain out of the tips and hence detect the molecular plateau at G_m as a signature in the measurement. Increasing the bending finally leads to the rupture of the metal-molecule-metal connection and an exponentially decreasing tunnel current (Fig. (37 k)). Typical conductance values for the conductance–position measurements are summarized in Tab. 3.

System	Resistance [Ω]	Conductance [S]	Conductance [G_0]
30 nm \times 30 nm Au junction	2×10^2	5×10^{-3}	65
Last Au atom	1.3×10^4	8×10^{-5}	1
Typical molecular conductance	$\geq 10^7$	$\leq 10^{-8}$	$\leq 1.3 \times 10^{-4}$

Table 3: Overview of typical resistance and conductance values for the CPC.

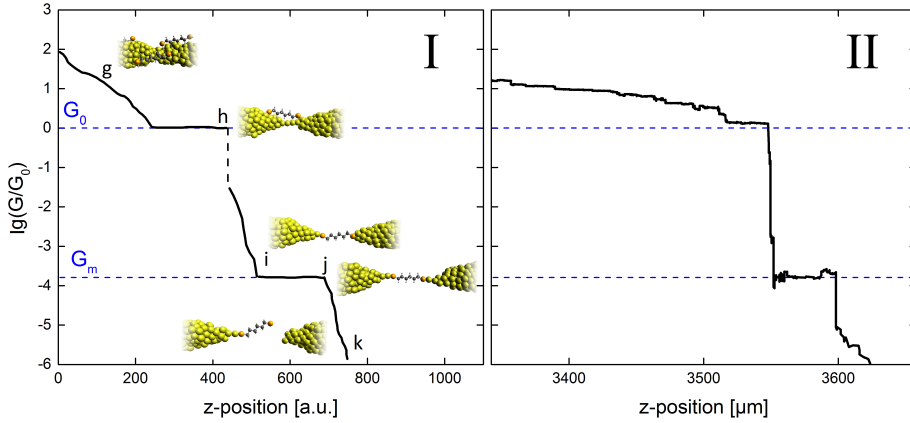


Figure 37: If molecules are deposited onto the junction, one or more additional plateaus can be visible in the CPC. A sketch of the CPC behavior is shown in (I), whereas (II) shows an exemplary measurement of a molecule for comparison. At the starting point the junction is closed, the electrodes form a bridge and the molecules do not contribute to the conductance (g). The first part (g, h) is identical to the CPC without molecules (Fig. (28 a-d)). After the chain of atoms ruptures (h), vacuum tunneling is the dominant conductance mechanism. However, at some point the molecule is placed between the electrodes (i). If the electrodes are separated further and the anchoring bonds are strong enough the molecule pulls out a few atoms while the conductance is unchanged, similar to the situation of the plateau at G_0 . Hence, a second plateau of the molecule G_m occurs in the CPC, before the molecule is de-contacted (j) and tunnel decay occurs again (k).

With the help of the CPCs (and the resulting histogram) we are able to determine the plateau that indicates the molecular conductance. Simply spoken, we know the conductance of one molecule trapped between the two tips and moreover we can identify the z-position at which the metal-molecule-metal contact has to be expected (Fig. (37 i,j)). Finally, in order to characterize the molecule itself, the CPC measurement is stopped when this conductance value (i.e. plateau at G_m) is reached and a current-voltage curve (IVC) is performed. The recording of reproducible IVCs turned out to be often difficult, since the system—one molecule between two Au tips—is not very stable especially for high electric fields. Although the dissipated power seems to be quite low, typically $< 10^{-8}$ W, the power density is extremely large for the molecule, theoretically up to 10^{20} W m^{-3} which is much larger than the maximum power allowed for conventional cables [2]. Although the dissipation mostly takes place in the metal electrodes, the metal-molecule-metal system will be influenced significantly.

As mentioned in Chaps. (2.4.1–2.4.3), in principle an IVC provides more insight into the molecule as a CPC. Features like molecular orbital levels, coupling strength to the electrodes or vibrational modes of the molecule might be obtainable. In this thesis different analyzing techniques are used to extract information from the IVCs.

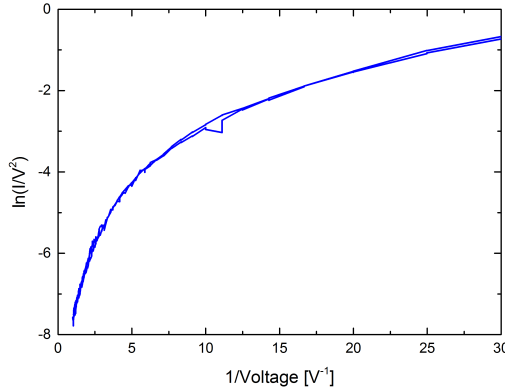


Figure 38: Fowler-Nordheim plot ($\ln(I/V^2)$ versus V^{-1}) of the IVC of a break-junction without molecules. The curve shows no sign of a kink, i.e. barrier tilting according to Eq. 35, up to 1 V.

4.2.1.2 Resonant Tunneling Model

In case of symmetrical “s-shaped” IVCs the resonant tunneling model (RTM) is used to estimate the molecular level ϵ_0 and the coupling constant Γ (Chap. 2.4.2) via a direct fit of the IVC. In case of asymmetric IVCs the fit procedure is more difficult, since different coupling constants Γ have to be assumed. Nevertheless, it is possible as shown in detail in the discussion of IVCs measured for BeDT in Chap. 4.3. Generally, the values obtained via this fit procedures have to be interpreted with care since (i) they are obtained by fitting an arcus tangent to an s-shaped curve and (ii) due to the limited voltage range (typically -1.5 V to $+1.5$ V), only a small part of the arcus tangent characteristic is fitted.

4.2.1.3 Fowler–Nordheim Plot

Alternatively, the Simmons model can be used to estimate molecular levels using the so called Fowler-Nordheim plot (FN plot) which is a plot of $\ln(I/V^2)$ versus V^{-1} . The FN plot is based on the following observations. In the low voltage regime the IVC is linear (Eq. 18):

$$J_I(V) = \gamma V, \quad (34)$$

while in the higher voltage (FN regime) the dependence changes to

$$J_{\text{FN}}(V) = \delta_1 V^2 \exp(-\delta_2 V^{-1}). \quad (35)$$

γ , δ_1 and δ_2 are positive constants (see Eq. 18 and 21). In the case of pure field emission a plot of $\ln(I/V^2)$ versus V^{-1} (FN plot) should yield a constant slope $m_{\text{FN}} = -\delta_2 = -\frac{2B}{2.96e} d\Phi_1^{3/2}$ $m_{\text{FN}} = -\delta_2 = -2Bd\Phi_1^{3/2}/(2.96e)$ (see Eq. 21), and d or Φ can be extracted from the slope. For IVCs of molecules the FN plot reveals this characteristic only at very high voltages that typically lead to a destruction of the metal-molecule-metal contact.

Nevertheless, the transition from the linear to the FN regime, and therefore an estimation for the molecular level ϵ_0 , can be obtained by the FN plot of the IVC. Fig. (39 a) shows the FN plot for a linear and a cubic current–voltage dependence. The linear dependence results in a positive (for $V > 0$) and negative (for $V < 0$) slope with monotonic increase and decrease, respectively. The FN behavior shows a constant slope, and any stronger voltage dependence of I , e.g. $I \propto V^3$, results

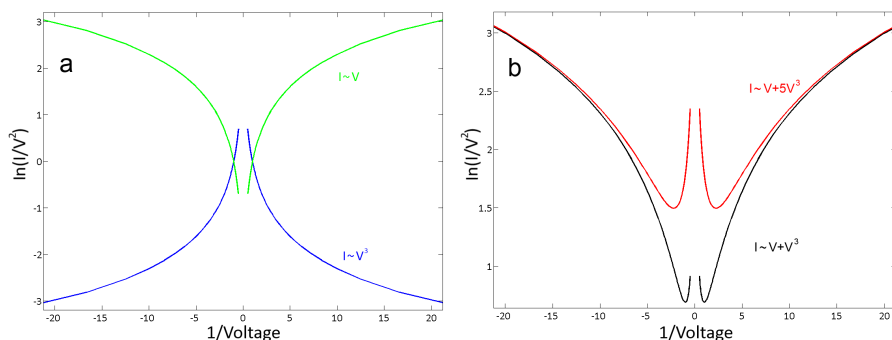


Figure 39: Simulations of different IVCs in the form of a FN plot, $\ln(I/V^2)$ versus V^{-1} . For a linear IVC (a, green line) the plot exhibits a positive slope (in the positive voltage regime), whereas a cubic behavior leads to a negative slope (a, blue line). Subsequently, the change of the linear to the field emission behavior of the IV curve is characterized by a minimum at V_{FN} in the FN plot. This kink occurs if the voltage dependence changes from less to more than quadratic. The stronger the cubic behavior (b, red line), the smaller is the value of V_{FN} , i.e. the lower is the voltage that has to be applied for the IVC to observe a kink.

in a behavior in the FN plot opposite to that of the linear dependence, i.e. a negative or positive slope for $V > 0$ or $V < 0$, respectively. A combination of the different voltage dependencies, which represents a good approximation of the shape of an IVC of a molecule, automatically yields a characteristic minimum in the FN plot where the behavior changes from linear to the cubic FN behavior (Fig. (39 b)). This minimum at a voltage V_{FN} indicates approximately the start of the field emission and can therefore be used to estimate the barrier height in the Simmons model, i.e. one of the molecular levels. However, one should note that any IVC exhibits a minimum in the FN plot when the voltage dependence of the current changes from less than quadratic (positive slope in the FN plot) to more than quadratic (negative slope in the FN plot), see Fig. (39 b).

Nevertheless, without molecule (reference measurement) the Simmons model represents the work function of the electrons, which for a flat gold-surface should be $W_{\text{vacuum}} \approx (4.8 - 5.3) \text{ eV}$ [3, 31]. If we assume a rectangular barrier, an applied voltage tilts the barrier. However only for voltages of the order of W_{vacuum} this will lead to a significant decrease of the effective widths. For typical break-junction measurements IVCs with voltages much higher than 1 V are difficult to measure. Therefore, without molecules we do not expect a kink in the Fowler-Nordheim plot, which is demonstrated in Fig. 38.

4.2.1.4 Double Logarithmic Plot

Another way to analyze an IVC is the representation in a double-logarithmic form. If the current depends on the voltage in form of a potential law, $I \propto V^n$, the double logarithmic plot should show a linear dependence with a slope n . Thus, in an ideal case the double logarithmic plot should start with a slope 1 at low voltages (linear regime). At higher voltages—if a molecular orbital enhances the conductance, or the field effect sets in—the slope should be larger than 1, before the current saturates at very high voltages (see Fig. 40). So far, in the literature the standard double-logarithmic plot was not used in the discussion of IVCs for single molecules.

4.2.1.5 Derivatives of the IVC

The first and second derivative of the IVC yield information about the molecular contribution to the current. A kink in the first derivative (dI/dV vs. V) and peak in the second derivative

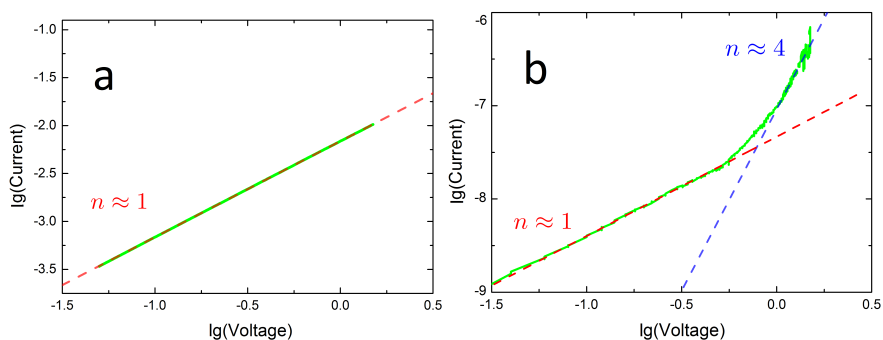


Figure 40: Double logarithmic plot of a linear IVC (a), with a slope of $n \approx 1$. (b) A double logarithmic plot of an IVC of a molecule shows a linear regime at low voltages, slope $n \approx 1$, and a strong increase at higher voltages, slope $n \approx 4$.

$(d^2I/dV^2 \text{ vs. } V)$ indicate that the applied voltage is identical (or close) to an energy level (HOMO or LUMO) of the molecule. However, since in this thesis the derivatives are numerically evaluated from the data of the IVC, small changes in the measurement lead to large fluctuations in the first, and hence second derivative.

4.3 Hexanedithiol and Benzenedithiol

Hexanedithiol and benzenedithiol are well known and small organic molecules. Particularly for electronic measurements of benzenedithiol data exist in the literature. Both molecules can easily be prepared for break-junction measurements and are commercially available. For this reasons they are chosen as test-bed molecules.

Hexanedithiol

The basic structure of 1,6-hexanedithiol (HDT) consists of a row of six carbon atoms, each with two hydrogen atoms, and terminated at both ends by a thiol (S-H) group. The elemental formula is $C_6H_{14}S_2$ (see Fig. 41). If the molecule attaches to Au the S-H bond is replaced by a S-Au bond.

The hexanedithiol (99.8%, Sigma Aldrich) was analyzed with elementary analysis and gas chromatography. The values obtained for the elementary analysis of carbon and hydrogen confirm the purity of the solution. The chromatogram shows a clear peak at the expected position of HDT (relative area 94.83%) and a smaller second peak (relative area 5.17%), that might correspond to 1,2-dithiocane or an isomeric structure ($C_6H_{12}S_2$) (see appendix B). For the measurements, a 1 mM solution of HDT in pure ethanol is prepared.

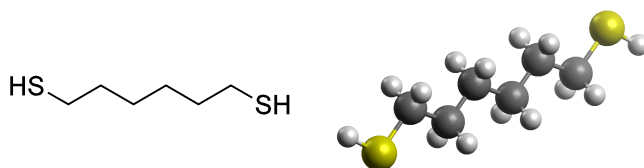


Figure 41: Structure of 1,6-hexanedithiol. Hexanedithiol consists of an alkane of six carbon atoms, with one thiol group (SH) attached to each end.

Due to their simple structure of single σ -bonds between carbon atoms, alkanes, like hexanedithiol, are not expected to show complex conductance effects. Furthermore, the probability to form multi-molecule structures like long chains is low. For HDT the connection to the Au electrodes is rather strong due to the thiol groups at both ends, which result in an Au-S bond. As a result of these features the CPCs show one dominating clear molecular plateau below the quantum of conductance, as shown in Fig. 42. The levels of this plateau corresponds to $G_{\text{HDT}} \approx 5.8 \times 10^{-4} G_0$, and the z -extension can be up to $100 \mu\text{m}$, which corresponds to a lateral elongation of up to 1 \AA or roughly the radius of a single Au atom.

In some of the curves no molecular plateau is visible, i.e. no molecule seems to be trapped between the Au in that specific measurement cycle (in this case the CPC is similar to that of Fig. 28). In Fig. (42 b) four CPCs are plotted. For a better distinction the CPCs are displayed with a horizontal offset. They show very similar conductance levels for the quantum of conductance at G_0 and the distinct molecular plateau at G_{HDT} . However, all CPCs possess additional smaller plateaus at various conductance values. Different effects can be responsible for these plateaus. First, more than one single molecule might contribute to the conductance, e.g. two or more molecules can be attached in parallel between the electrodes leading to a plateau at a conductance $G > G_{\text{HDT}}$.

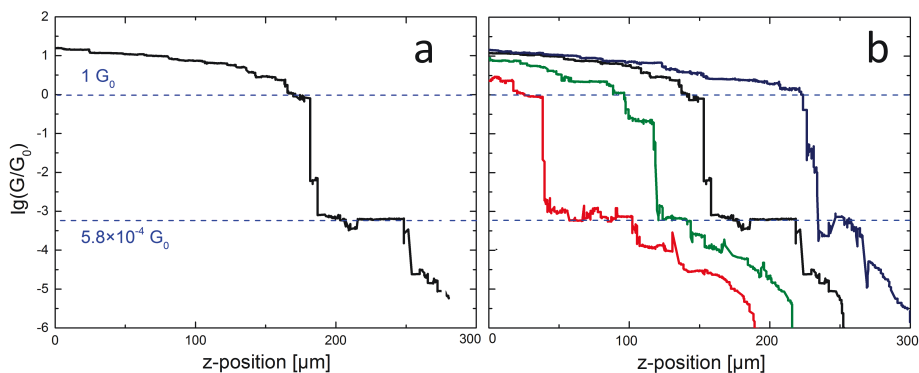


Figure 42: The logarithmic conductance in units of G_0 against the piezo-position for the measurement of HDT. Below G_0 HDT shows a strong decrease of the conductance with increasing position. A very distinct plateau in the CPC at $5.8 \times 10^{-4} G_0$ can be observed (a), but every single curve has a unique shape (b). The curves in b) are horizontally shifted for clarity.

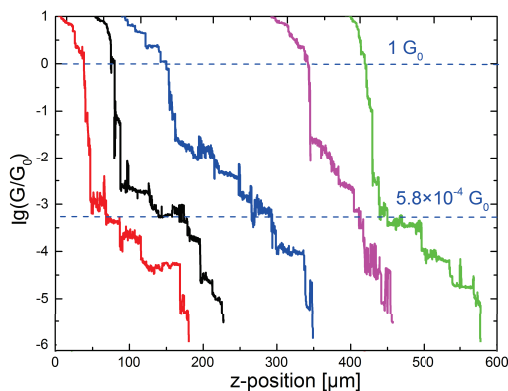


Figure 43: The CPC of HDT recorded with a velocity of $v_{\text{piezo}} = (0.7 \pm 0.1) \mu\text{m/s}$. If the sample is very slowly bent the molecular plateau is still present (see Fig. 42), however, different plateaus similar to the molecular plateau are measured due to the step-like motion of the piezo-positioner. Thus, the plateau is difficult to detect.

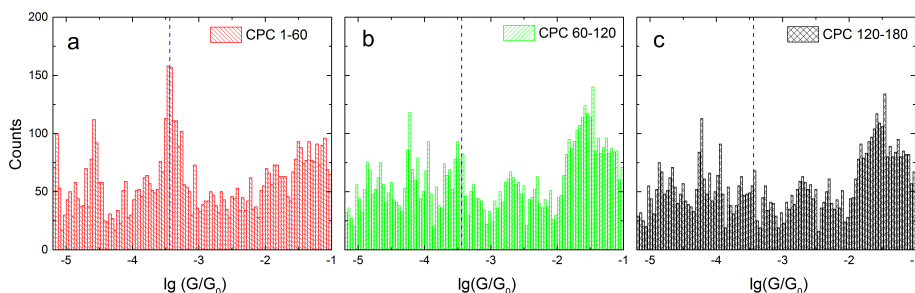


Figure 44: Three histograms of 1,6-hexanedithiol recorded in successive CPCs. The number of the CPCs used for the different histograms are given in the legend. After the measurement cycle is repeated many times the molecule peak might vanish.

Second, the probability may be low for two molecules to pull out Au atoms and to form a chain between the electrodes at the same time, however, additional molecules could be connected just to one electrode and thus also change the system (for instance lower the work function) and therefore the measured conductance. Third, the rearrangement of the Au atoms before and after the break is different for each CPC. Relaxation effects in the electrodes could lead to sudden jumps or small plateaus in the CPC. Finally, the effect of a molecule detaching and attaching to one electrode could cause jumps in nearly every measured plateau. The latter could be for instance the reason for the black CPC in Fig. (42 b) that exhibits a rather stable plateau except for a small temporary decrease in the conductance.

Furthermore, the shape of the CPCs depends on the velocity of the bending procedure. For the measurements in Fig. (42 b) a velocity of $v_{\text{piezo}} \approx 3 \mu\text{m/s}$ was used. If the velocity is too high ($v_{\text{piezo}} \geq 15 \mu\text{m/s}$) molecular plateaus cannot be detected, since the time they are present is too short for the data recording. However, also for very small velocities the CPCs do not reveal the electronic properties of the molecules in an optimal way. In this case the step-like motion of the piezo-positioner comes into effect, after each step of the piezo-positioner the configuration is stabilized. Six different curves of HDT recorded with a velocity of $v_{\text{piezo}} \approx 0.7 \mu\text{m/s}$ are presented in Fig. 43. It is difficult to distinguish between molecular and “artificial” plateaus due to the slow bending velocity causing a drift of the data.

Although the plateaus are clearly visible in the CPCs, a histogram summarizing a large number of CPCs might not display the molecular features. In Fig. 44 three different histograms are presented that are recorded for HDT under same conditions. In the first set of curves the HDT plateau is visible in form of a peak at G_{HDT} in the histogram. However, the other two histograms that were taken after the first measurement do not show this peak. After repeating the measurement cycle many times no molecule might be attached to the junction anymore. A summarized histogram of all the data of the three histograms might not allow to distinguish the HDT peak from the background. An alternative way of presenting a histogram is shown in Fig. 45. It displays a contour histogram for HDT which provides additional information, i.e. the z-position where the Au-molecule-Au contact is most likely established and information on the work function at the molecular contact.

Finally it should be noted that histograms summarize the conductance values at a constant voltage, typically a small voltage of (50–150) mV. Hence for most molecules—like alkanes—the conductance of the contact between anchoring group and Au dominates the experimental value

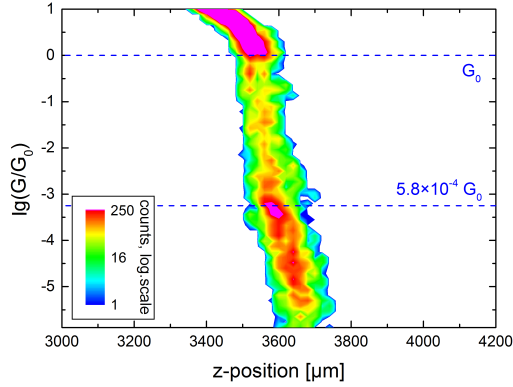


Figure 45: Contour histogram of 1,6-hexanedithiol (HDT). The plateau and rupture at G_0 is clearly visible. Below $10^{-3} G_0$ a maximum at G_{HDT} shows the conductance and z -position of the Au-molecule-Au contact.

for the plateau, i.e. G_{HDT} for this molecule. For a more detailed analysis of the electronic properties of the molecules current-voltage curves (IVCs) are necessary, they are discussed in detail for benzenedithiol in the next chapter. For completeness, they are also shortly discussed here for HDT. IVCs of HDT exhibit a characteristic s-shape. Since for voltages ≥ 0.9 V the measurement of HDT becomes quite unstable, the resonant tunneling model (RTM) is fitted to the data recorded for $|V| \lesssim 1$ V. The RTM fit yields a low molecular level $\epsilon_{\text{RTM}}(\text{HDT}) \approx 0.9$ eV and a coupling parameter of $\Gamma \approx 2.5 \times 10^{-5}$ eV. However, the fitting is not very sensitive to small changes of the data. A degree for the accuracy of a fit is given by the coefficient of determination r with $0 < r < 1$. The closer the value given of r lies to 1 the better the model fits to the data. In this case $r \approx 0.96$. Furthermore, in the FN plot (Fig. 46) no kink is observed that would indicate a change to field emission.

In conclusion, single molecule measurements of 1,6-hexanedithiol (HDT) were successfully performed with our setup. HDT shows a remarkably stable plateau at $G(\text{HDT}) \approx 5.8 \times 10^{-4} G_0$ in the CPC recorded at low voltages. The quality of the curves depends on the bending velocity. The best results for HDT are obtained at a velocity of the piezo-positioner of $v_{\text{piezo}} \approx (3 - 6) \mu\text{m/s}$, or a (theoretical) displacement of the Au tips of $v_{\text{tip}} \approx 5$ pm/s, respectively. The literature values for the conductance of HDT differ dramatically, they range from $\epsilon(\text{HDT}) = 1.3 \times 10^{-5} G_0$ to $\epsilon(\text{HDT}) = 1.2 \times 10^{-3} G_0$ [48].

The corresponding IVCs of HDT are stable up to a voltage of $|V| \lesssim 1$ V and show a characteristic s-shape. RTM fits yield a value for the molecular orbital of $\epsilon_{\text{RTM}}(\text{HDT}) \approx 0.9$ eV. The corresponding FN plot indicates that the barrier should be higher than 1.0 eV.

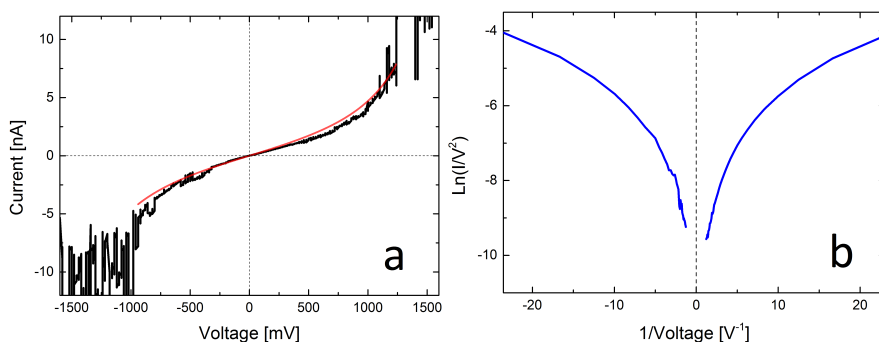


Figure 46: The IVC of HDT exhibits a characteristic s-shaped form but becomes unstable at higher voltages (a). By fitting the symmetrical resonant tunneling model to the IVC values are obtained for the molecular orbital $\epsilon = (0.876 \pm 0.007)$ eV and for the coupling constant $\Gamma = (2.46 \pm 0.03) \times 10^{-5}$ eV, respectively. The coefficient of determination is $r \approx 0.96$. A FN plot (b) shows no kink and hence no sign of starting field emission for a voltage $-1 < V < 1$ (for higher voltage fluctuations are too strong) which indicate that the height of the potential barrier is not measurable for this system.

Benzenedithiol

1,4-benzenedithiol (BeDT) consists of benzene connected with a pair of opposite positioned thiol groups. The elemental formula of BeDT $C_6H_4S_2$ differs from hexanedithiol only in the number of hydrogen atoms. The ring of benzene is conjugated, i.e. single and double bonds alternate. The single bond is a covalent bond where a pair of electrons of the s-orbitals are shared between two atoms (σ -bond). The double bond involves four electrons and consists of an overlap of s-orbitals (σ -bond) and p-orbitals (π -bond). Consequently, through the connecting σ -bonds the p-orbitals of the system overlap, and the π -electrons (of the p-orbital) are delocalized over the molecule. This is called conjugation, a conjugated system has a lower overall energy and is expected to possess a high conductance.

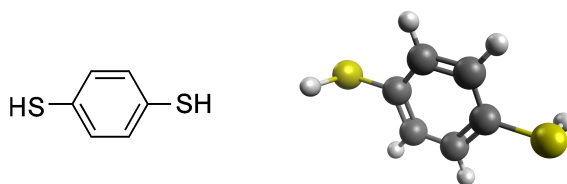


Figure 47: Structure of 1,4-benzenedithiol. The aromatic ring has two thiol groups attached at the first and fourth position.

The benzenedithiol (99.8%, Sigma Aldrich) was analyzed with elementary analysis and gas chromatography, the exact results can be found in appendix B. The measured content of carbon and hydrogen obtained from the elementary analysis differs slightly from the theoretical value, 0.3% total mass difference with respect to the theoretical value for the weight of carbon and 0.03% for the hydrogen, respectively. In both cases this difference exceeds the error margins. However, only one clear peak of benzenedithiol is detectable in the chromatogram. For the measurements, a 1 mM solution of BeDT in pure ethanol was prepared.

Fig. 48 shows four exemplary CPCs of BeDT. The molecular plateaus lie between $0.1 G_0$ and $0.01 G_0$, multiple plateaus are visible. One reason might be given by the size of the molecule. The smaller the molecule, the more important becomes the geometrical arrangement of the Au and the anchoring groups which can differ for each CPC. Furthermore, enhanced conductance by two (or more) molecules connecting the junction in parallel has to be considered, especially for smaller molecules. Moreover, BeDT consists of a conjugated carbon ring which might allow the molecules to cluster easily to bigger complexes that influence the measurement. One of these effects may have caused the jump in the fourth curve in Fig. (48 a) after reaching a stable plateau slightly below $0.1 G_0$.

The IVCs of BeDT can be analyzed using the different methods mentioned above. RTM yields values of the molecular orbital by fitting it with Eq. 24. A typical example is given in Fig. (49 a).

The RTM fit yields values of $\epsilon(\text{BeDT}) = (0.4625 \pm 0.004) \text{ eV}$ for the molecular orbital and $\Gamma = (1.059 \pm 0.001) \times 10^{-4} \text{ eV}$ for the coupling constant, respectively. For the symmetrical curve the fitting is very accurate, the coefficient of determination is $r \approx 0.998$. Again in the Fowler–Nordheim plot of the IVC, no minimum is observed for $|V| \leq 0.6$ (see Fig. (49 b)). According

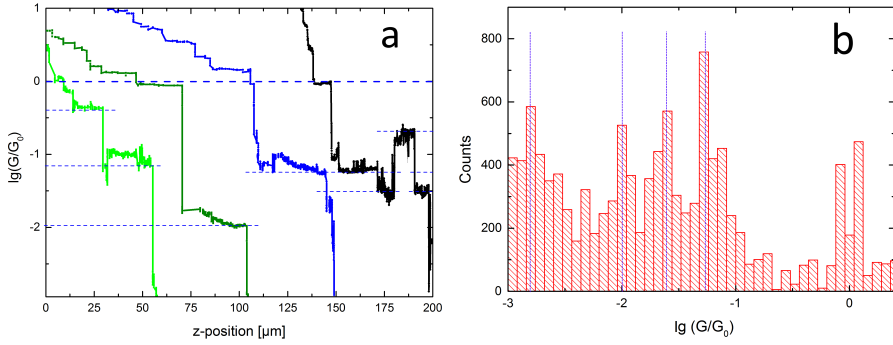


Figure 48: BeDT shows multiple steps in the CPC (290 K, 150 mV) with conductance values between $10^{-1} G_0$ to $10^{-3} G_0$ (a). The curves are shifted horizontally for clarity. Consequently, the histogram of BeDT exhibits different peaks of similar height (b).

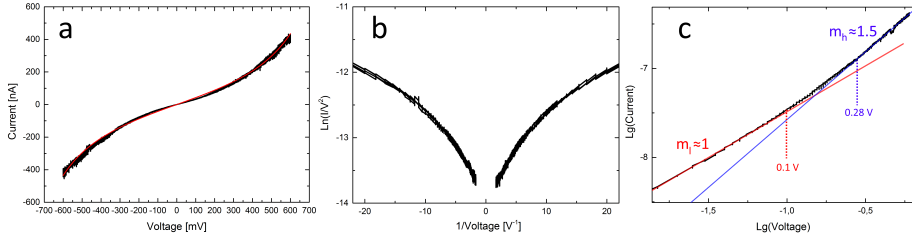


Figure 49: The IV-curve of BeDT can be analyzed with different methods. Fitting the IVC of BeDT with the resonant tunneling model (a) yields $\epsilon = (0.4625 \pm 0.004) \text{ eV}$ and $\Gamma = (1.059 \pm 0.001) \times 10^{-4} \text{ eV}$ for the molecular level and the coupling constant, respectively. The model fits the data (red line) with very high accuracy ($r \approx 0.998$). The Fowler-Nordheim plot shows no kink for the IVC (b). According to the Simmons model this indicates that a higher voltage is necessary to tilt the potential barrier. In (c) the double logarithmic plot of the IVC reveals a slope of $m_l \approx 1$ for the lower voltage regime (fitted by the red line), and a slope of $m_h \approx 1.5$ for the higher voltage regime (fitted by the blue line). The linear regime fits the curve nicely up to 100 mV, whereas a behavior $I \propto V^{1.5}$ is measured at voltages higher than 280 mV.

to the Simmons model, this implies that the applied voltage was not sufficiently large. Finally, the double logarithmic plot of this IVC shows that the linear regime exists at low voltages, above 280 mV it changes to a dependence of $I \propto V^{1.5}$ but does not reach the FN regime with a dependence stronger than $I \propto V^2$. These power law dependencies fit the curve well and explain why no minimum is obtained in the Fowler-Nordheim plot.

Most IVCs are (approximately) symmetrical, but asymmetrical behavior occurs also, as shown in Fig. 50. Obviously, fitting the asymmetrical IVCs with the symmetrical expression of the resonant tunneling model is not really successful and yields a large error $r \approx 0.84$ (see Fig. (50 a)). In principle, the resonant tunneling model can be modified to simulate an asymmetrical behavior, however, the process is complicated. One way of interpreting the data is to use an independently fitting of the positive and negative applied voltage, respectively. Consequently, both voltage regimes are described by independent values for the molecular level and coupling constant. In Fig. (50 b) $\epsilon_l(\text{BeDT}) \approx (0.856 \pm 0.003) \text{ eV}$ and $\epsilon_r(\text{BeDT}) \approx (1.178 \pm 0.008) \text{ eV}$, for the negative and positive voltage regime, respectively. The coupling constants are $\Gamma_l = (1.53 \pm 0.01) \times 10^{-5} \text{ eV}$ and $\Gamma_r = (1.82 \pm 0.02) \times 10^{-5} \text{ eV}$. The fitting for both sides is relatively accurate ($r_l \approx 0.976$, and

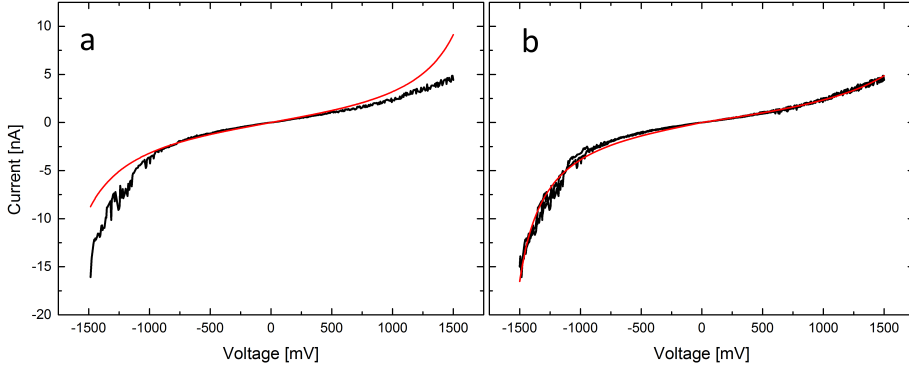


Figure 50: Fitting an asymmetric IVC of BeDT (black line) with the RTM (a, red line) yields $\epsilon(\text{BeDT}) = (-0.95 \pm 0.02) \text{ eV}$ and $\Gamma = (1.62 \pm 0.02) \times 10^{-5} \text{ eV}$ for the molecular level and the coupling constant, respectively. However, the coefficient of determination is only $r \approx 0.84$. By separating the voltage regime into two parts and using an independent set of parameters of the symmetrical model for each side (b, red line) the fitting becomes more appropriate. The coefficients of determination are $r_l \approx 0.976$, and $r_r \approx 0.989$ for the left and right hand side, respectively. The molecular levels are $\epsilon_l \approx (0.856 \pm 0.003) \text{ eV}$ and $\epsilon_r \approx (1.178 \pm 0.008) \text{ eV}$, and the coupling constants are $\Gamma_l = (1.53 \pm 0.01) \times 10^{-5} \text{ eV}$ and $\Gamma_r = (1.82 \pm 0.02) \times 10^{-5} \text{ eV}$.

$r_r \approx 0.989$). As expected, the molecular energy level on the left side is smaller compared to the right side. The asymmetry in the IVCs can be caused by different geometrical arrangement of the Au atoms for the left and right contact, resulting in a different coupling of the molecule to the Au. Alternatively, the small size of BeDT enhances the chances of more than one molecule contributing to the current, which could cause an asymmetric situation via clustering of BeDT molecules.

In conclusion, 1,4-benzenedithiol (BeDT) exhibits a number of plateaus in the CPCs (and therefore several peaks in the histogram). The observed plateaus lie around $10^{-2 \pm 1} G_0$. Since clustering or multiple connection of molecules lead automatically to an increase of the conductivity, it is expected that the conductance for a single BeDT molecule should be close to the lowest conductance plateau, i.e. $G(\text{BeDT}) \approx 10^{-3} G_0$. Due to the conjugated structure of benzene (and the delocalization of the electrons) a large conductance is expected. However, since the bonds of the anchoring groups to the Au possess a large resistance compared to that of benzene, the S-Au bonds are expected to dominate the conductance value. A large number of experimental and theoretical literature values exists for the conductance of a BeDT molecule. The reported experimental conductance values differ over several orders of magnitude, i.e. they range from $1 \times 10^{-1} G_0$ to $5 \times 10^{-5} G_0$ for a single BeDT molecule, whereas the theoretical values range between $0.05 G_0$ and $0.5 G_0$ [48].

The symmetric IVCs of BeDT exhibit a characteristic and stable “s-shape”. Fitting one exemplary IVC with RTM yields a molecular level of about $\epsilon_{\text{RTM}}(\text{BeDT}) \approx 0.46 \text{ eV}$. The double logarithmic plot indicates that a contribution of the molecular level sets in already at $\epsilon_{\text{dl}}(\text{BeDT}) > 0.28 \text{ eV}$, whereas the FN-plot leads to a barrier height $\epsilon_{\text{FN}}(\text{BeDT}) > 0.6 \text{ eV}$. These values are representative for similar symmetrical IVCs obtained for BeDT.

In the case of asymmetric IVCs, the molecular levels obtained from the different methods are usually much higher, but differ for individual curves.

Literature values obtained from break-junction measurements (and calculated with RTM) are

$\epsilon(\text{BeDT}) \approx 0.5 \text{ eV}$ [38], and therefore close to our values.

Thus, the BeDT is successfully characterized in our break-junction setup. The range of conductance levels is consistent with the variety of conductance values in the literature and the molecular level (obtained by the RTM) corresponds to the literature values.

4.4 Terphenyldithiol

p-Terphenyl-4,4''-dithiol consists of three connected benzol rings in a row with two thiol groups at the ends. It represents a conjugated system with delocalized electrons. In organic light emitting diodes (OLED) similar molecules (triphenylamine) can be used [12]. The chemical formula of terphenyldithiol (TPT) is $C_{18}H_{14}S_2$. Our TPT has a purity of 96% (Sigma Aldrich) and is analyzed with elementary analysis and gas chromatography.

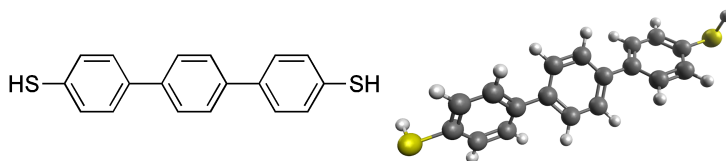


Figure 51: Structure of p-terphenyl-4,4''-dithiol. Three aromatic rings in a row are connected with a thiol group at the ends.

The weight of carbon obtained from the elementary analysis is approximately 1.5% below the theoretical expected value, whereas the amount of hydrogen is very close to the theoretical value. The chromatogram shows a clear peak of TPT (relative area 93.2%) but five additional peaks are detected, the largest one (relative area 3.6%) for terphenylthiol—an identical molecule, however, with only one thiol group (see appendix B). Since the probability is low for terphenylthiol to connect to both electrodes in the measurement we can ignore this molecule. For the measurements, a 0.2 mM solution of TPT in pure ethanol was prepared.

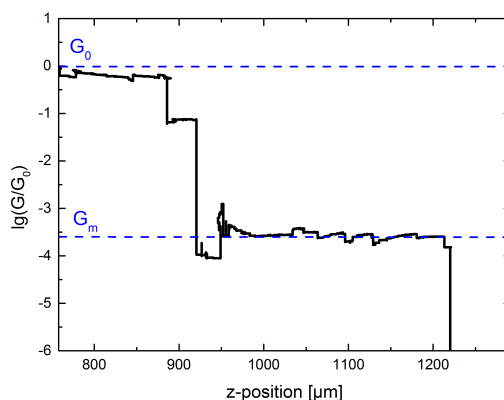


Figure 52: Example of a very stable CPC of TPT recorded at 36 K. The reduced temperature seems to lead to a reduced mobility and thermal fluctuation of the molecule and the Au atoms in the electrode.

The CPCs of TPT are measured at 50 mV. In some CPCs several plateaus at different conductance values are present. However, in most cases a major plateau is visible between $10^{-3} G_0$

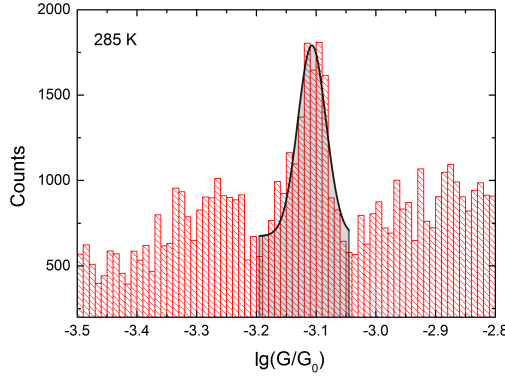


Figure 53: Histogram of p-terphenyl-4,4''-dithiol at 285 K and 150 mV with a Gaussian distribution as a fit to the histogram peak. Note that the fitted Gauß-function has no physical meaning, but helps to measure the approximate position of the peak $G_{285\text{ K}}(\text{HDT}) = (7.8 \pm 0.9) \times 10^{-4} G_0$.

and $10^{-4} G_0$, see for example Fig. 52. The resulting histogram, obtained from several hundred CPCs, yields a clearly visible peak in the conductance spectrum (Fig. 53). The position of the peak changes with temperature. The resulting temperature dependence is shown in Fig. (54 a). The higher the temperature, the higher the conductance of the main conductance peak. To analyze this behavior, the data are plotted in form of an Arrhenius plot (Fig. (54 b)). For direct (elastic) tunneling, the current should not depend on the temperature. Whereas for inelastic hopping transport a dependence $\ln(I/v) \propto T^{-1}$ is predicted (see also Tab. 1 in Chap. 2.4.3). Fig. (54 b) shows the corresponding plot of $\ln(I)$ versus T^{-1} . For low temperatures the current does not change with temperature indicating direct tunneling as dominating conduction mechanism. However, at $T_{\text{trans}} \approx 100$ K a change in the behavior sets in, and the current increases rapidly with increasing temperature in agreement with the hopping mechanism [20, 41]. Therefore we conclude that the electronic transport mechanism changes from elastic tunneling for $T \lesssim 100$ K to an inelastic hopping mechanism for $T \gtrsim 100$ K.

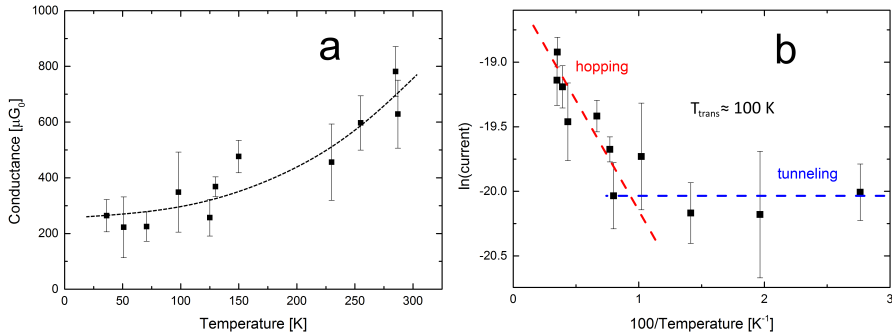


Figure 54: Temperature dependence of the dominating conductance peak of the histogram for TPT in linear form (a) and in form of an Arrhenius plot (b). The change of the temperature dependence in (b) from constant to exponential increase indicates a transition from a tunneling to a hopping mechanism at $T_{\text{trans}} \approx 100$ K.

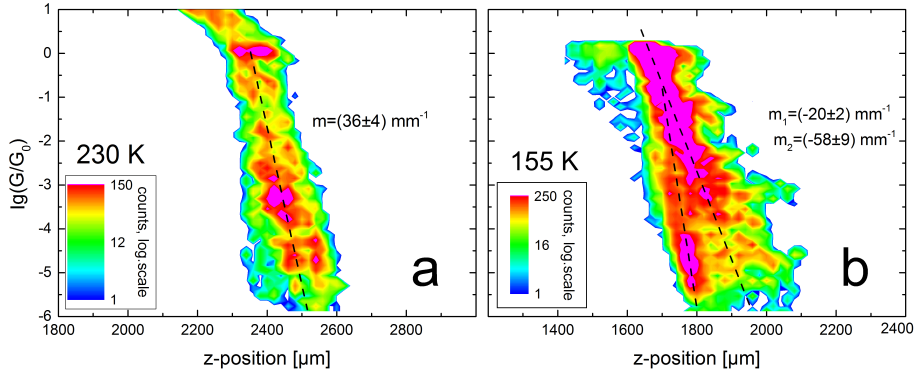


Figure 55: The contour histograms of TPT show the breaking at the quantum of conductance G_0 , and the molecular peak between 10^{-3} and $10^{-4} G_0$. Furthermore, a decay constant different from vacuum tunneling can be observed (see dashed line in (a)). For the contour histogram recorded at 230 K (a) the slope is $m = (36 \pm 4) \text{ mm}^{-1}$, and therefore $\delta \approx 0.6 \text{ \AA}^{-1}$. In some contour histograms both behaviors, vacuum tunneling CPCs and molecular influenced CPCs are observable (b). The corresponding decay constants are $\delta \approx -1 \text{ \AA}^{-1}$ for the vacuum tunneling and $\delta \approx 0.4 \text{ \AA}^{-1}$ for the molecular traces. An overview of the decay constants for TPT at different temperatures is given in Fig. 56.

Two exemplary contour histograms of TPT are presented in Fig. 55. By fitting the slope of the conductance traces a decay constant for the tunnel current in case of a molecular junction is obtained. The decay constant is about a factor 2 smaller than the decay constant for vacuum tunneling without molecules. The values for the tunneling constant change because the work function of the metal might be lower if molecules are present. However, also the plateaus in the conductance traces influence the slope significantly, since they are included in the fitting of the slope of the contour histogram. Fig. (55 b) shows a contour histogram composed of CPCs that show molecular behavior, and CPCs that exhibit vacuum tunneling. In the contour histogram the vacuum tunneling has a decay constant of $\delta_{\text{vacuum}} \approx 1 \text{ \AA}^{-1}$ and the molecular part, where a much slower decrease is observed, $\delta_{\text{TPT}} \approx 0.4 \text{ \AA}^{-1}$. The decay constant for TPT at different temperatures calculated from contour histograms are shown in Fig. 56. It does not depend on the temperature, and is clearly below the vacuum tunneling decay constant. Since the histograms are measured in the linear regime at a constant voltage of 50 mV, the conductance value obtained from the peak in the histogram is most likely characterizing the metal-molecule contact.

Furthermore, IVCs of TPT are recorded at different temperatures and FN plots and double logarithmic plots are performed. TPT can be measured up to a rather large voltages of $\pm 1.5 \text{ V}$ in a stable and reproducible way. Fig. (57 a) shows a typical measurement of an IVC of TPT recorded at 150 K, displayed in the linear form (including the RTM fit), FN plot, and double logarithmic plot. A characteristic s-shape is observed that indicates that one (or more) molecules are trapped in the junction. Both sides yields quite similar values for the molecular orbital ($\epsilon_l \approx 0.77 \text{ eV}$ and $\epsilon_r \approx 0.83 \text{ eV}$) and the coupling constant ($\Gamma_l = (9.1 \pm 0.1) \times 10^{-5} \text{ eV}$ and $\Gamma_r = (8.2 \pm 0.8) \times 10^{-5} \text{ eV}$). This indicates, that there is only a small anisotropy, most likely in the Au-molecule bond on both sides. The FN plot shows a clear minimum at $V_{\text{FN},l} \approx 1.05 \text{ V}$ and $V_{\text{FN},r} \approx 1.17 \text{ V}$ on the left and right hand side, respectively (cf. Fig. (57 b)).

Finally, in the double logarithmic plot a linear dependence is observed up to $\sim 550 \text{ mV}$, followed by a nearly quadratic regime up to 1 V . At even higher voltages a remarkably strong voltage de-

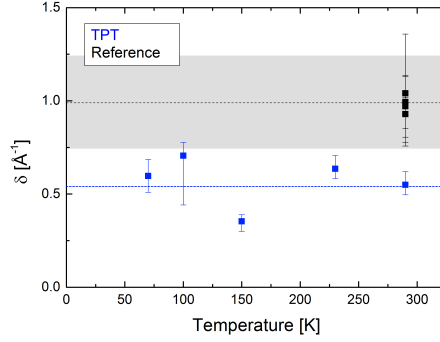


Figure 56: Decay constant of TPT $\delta_{\text{TPT}} \approx 0.55 \text{ \AA}^{-1}$ (blue), obtained from slopes in the contour histogram at different temperatures. The values are clearly below the value of the reference measurements without molecule, i.e. for vacuum tunneling (black). The decay constant of TPT exhibits no temperature dependence.

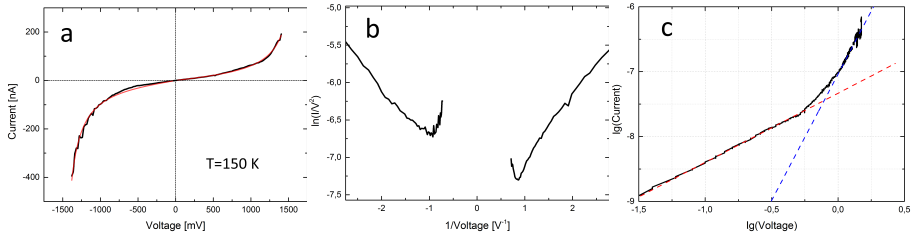


Figure 57: IVC of TPT at 150 K (a). The RTM fit with independent parameters for both sides yields the molecular level and coupling constants $\epsilon_l = (0.766 \pm 0.003) \text{ eV}$ and $\Gamma_l = (9.1 \pm 0.1) \times 10^{-5} \text{ eV}$, $\epsilon_r = (0.834 \pm 0.003) \text{ eV}$ and $\Gamma_r = (8.22 \pm 0.08) \times 10^{-5} \text{ eV}$ with an accuracy $r_l = 0.99$ and $r_r = 0.996$. (b) The Fowler-Nordheim plot shows two kinks at the transition voltages $V_{T-} \approx -1.05 \text{ V}$ and $V_{T+} \approx 1.17 \text{ V}$. (c) In the double logarithmic plot the current-voltage dependence $I \propto V^n$ is linear ($n = 1.06 \pm 0.01$) up to approximately 0.55 V, almost exactly at 1 V the dependence changes to $n = (3.9 \pm 0.1) \text{ V}$.

pendence of approximately $I \propto V^4$ is observed. The V_{FN} values of the FN plot are larger than the ϵ values of the RTM fit. The starting point of the quadratic voltage dependence in the double logarithmic plot corresponds to the transition voltage of the FN plot. Thus, the field emission contribution to the conductance starts between 0.8 eV and 1.1 eV for TPT trapped between Au electrodes at 150 K. IVCs of TPT exhibit different forms, hence different values for the molecular level are obtained. Fig. 58 shows a summary of a number of data obtained from IVCs of TPT (at room temperature). In Fig. (58 a) typical energy levels derived from RTM fits and FN plots are shown. The RTM values are generally slightly smaller than the FN values, i.e. the RTM provides an molecular level of $\epsilon_{\text{RTM}}(\text{TPT}) = (0.8 \pm 0.2) \text{ eV}$ whereas the FN plot gives $\epsilon_{\text{FN}}(\text{TPT}) = (1.0 \pm 0.3) \text{ eV}$. Fig. (58 b) demonstrates, that there exist no correlation between the RTM coupling constant Γ and the RTM molecular level ϵ . Moreover, the coupling constant seems to vary strongly (i.e. various coupling arrangements are possible), whereas the molecular energy level is more or less constant.

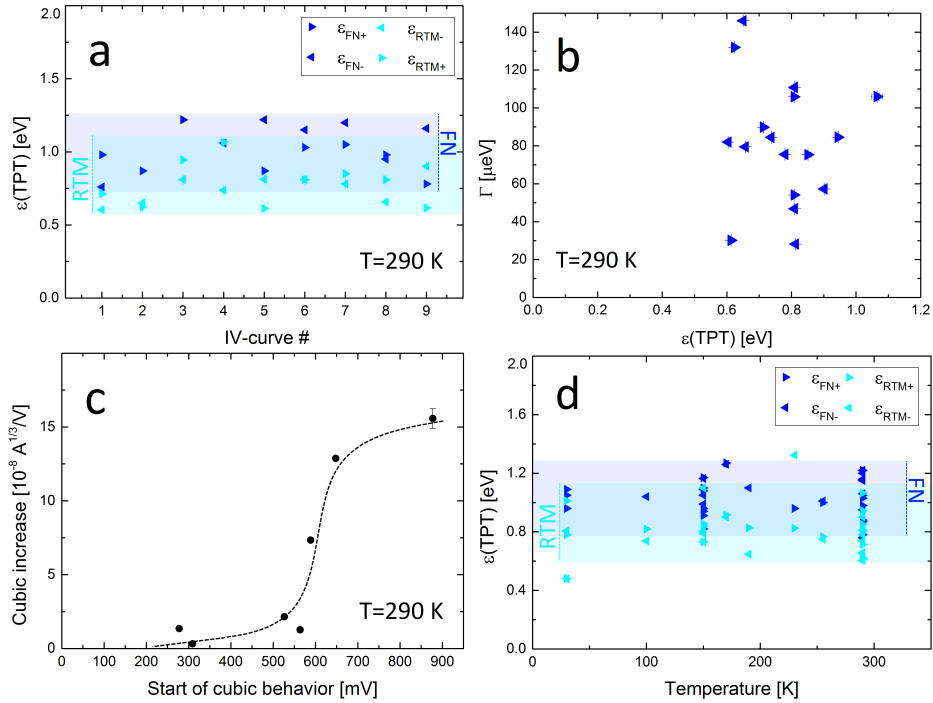


Figure 58: IVC measurement of TPT at room temperature (a, b, c) and over a large temperature range (d): (a) Molecular orbital levels for several IVCs from independent measurements. The values are obtained from the FN plot (dark blue) and the RTM fitting (cyan). Triangles pointing to the right and triangles pointing to the left indicate the value obtained in the positive and in the negative voltage regime, respectively. (b) RTM coupling constant Γ as function of the molecular levels ϵ , no correlation is observable. (c) Strength of the cubic behavior of IVCs versus the voltage where the cubic behavior starts. The later the cubic behavior starts the stronger is the increase. (d) Molecular orbital levels at different temperatures, as in (a) the values obtained from the FN plot (dark blue) and the RTM (cyan). No temperature dependence of the molecular levels are obtained.

Fig. (58 c) shows a discussion of the shape of the IVCs that might hint towards different broadening of the energy levels of the molecular orbital. Based on the double-logarithmic plot different power law behaviors $I \propto V^n$ can easily be distinguished. The figure shows in principle the correlation between the onset of the FN regime (i.e. a stronger behavior than $I \propto V^2$) and the steepness of the IVC in the FN regime (taking the steepness in the cubic regime $I \propto V^3$).

The correlation seems to indicate that the FN behavior starts at lower voltages if the energy band of the molecular orbital is broadened and at higher voltages if the energy band of the molecular orbital is narrow. The broadening of the energy band might be a result of the reorganization of the molecular orbitals if attached to gold. This might explain the different shapes of the IVCs and hence the different values for the molecular level that are evaluated with RTM and FN plot.

Finally, Fig. (58 d) shows the energy levels of the molecular orbital obtained from IVCs measured at different temperatures. No temperature dependence of the transition voltage in the FN plots or in the fitted parameters for the RTM is visible. The values differ (even for IVCs measured at constant temperatures) but over the whole temperature range constant molecular levels of $\epsilon_{\text{RTM}}(\text{TPT}) = (0.8 \pm 0.2) \text{ eV}$ and $\epsilon_{\text{FN}}(\text{TPT}) = (1.0 \pm 0.3) \text{ eV}$ are estimated. Hence, the molecular orbitals for TPT between Au electrodes does not change with temperature (or the effect is smaller than the deviation of molecular levels at constant temperature).

In conclusion, p-terphenyl-4,4''-dithiol (TPT) is characterized over a temperature range of 30 K to 290 K. Due to its length $\sim 1.6 \text{ nm}$ geometrical effects of the binding at the Au electrodes do not play a major role which makes this molecule highly suitable for break-junction characterization. CPCs and IVCs (up to 1.5 V) are recorded for different temperatures. In the CPCs clearly pronounced plateaus can be observed. The conductance plateaus result in a clearly visible peak in the histogram with a conductance value of $G(\text{TPT}) \approx 8 \times 10^{-4} G_0$ at room temperature, which decreases with decreasing temperature. This behavior is indicative for a change from a hopping transport for $T \gtrsim 100 \text{ K}$ to a tunneling dominated transport at low temperatures. The longer the molecule, the higher is the probability for the hopping process to dominate the conductance. The TPT molecule represents a relative short system for hopping mechanism (cf. Refs. [20, 41]).

In contrast to the CPC characterization, no temperature dependence is observed for the energy levels of the molecular orbitals that are derived from IVCs. RTM and FN plot yield temperature independent values of $\epsilon_{\text{RTM}}(\text{TPT}) = (0.8 \pm 0.2) \text{ eV}$ and $\epsilon_{\text{FN}}(\text{TPT}) = (1.0 \pm 0.3) \text{ eV}$. Although both derivations are based on relatively simple theories, the values should correspond to the molecular orbital that is involved in the conductance. Literature values obtained from measurements of self assembled mono-layers (SAM) lie in the same range ($\epsilon(\text{TPT}) = (1.07 \pm 0.10) \text{ eV}$, [21]).

The combination of the results of CPCs (i.e., temperature dependence of the conductance) and the IVCs (no temperature dependence of the molecular orbital) leads to the following conductance mechanism. At low temperatures direct tunneling dominates the transport. With increasing temperatures ($T_{\text{trans}} \approx 100 \text{ K}$) the conductance becomes temperature dependent, hopping sets in as the dominating transfer mechanism.

4.5 Porphyrines

Porphyrines represent a very interesting class of molecules that, for instance, play an important role in human metabolism processes or photosynthesis in plants. The basic structure of all porphyrines is the porphine (see Fig. 59) that consists of four modified pyrroles (a ring of four carbons and one nitrogen) connected via conjugated bonds. Therefore, porphyrines represents a highly conjugated system. Together with the large variety of chemical structures that can be attached to porphine, this leads to the unique versatility of this type of molecule.

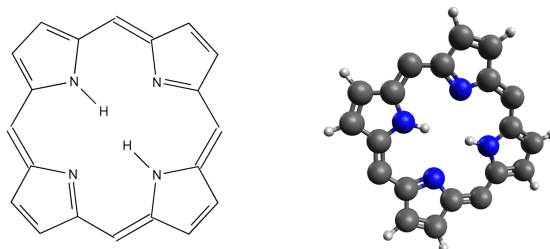


Figure 59: Basic structure of porphine.

A typical representative, the porphyrine 5,10,15,20-tetra(4-pyridyl)-21H,23H-porphine is used in this thesis. Four pyridine groups (pyridil) are connected to the basic porphine structure (see Fig. 60). The tetrapyridil-porphine (TPyP) is commercially available (Sigma Aldrich/Frontier Scientific, CAS-nr. 16834-13-2) with a purity of 97%. The elemental analysis of our material yielded theoretical values for nitrogen and hydrogen, whereas the measured weight of carbon was roughly 0.5% lower than expected. The proton-NMR measurement exhibited the expected peaks [17] and only a small contamination (see appendix B).

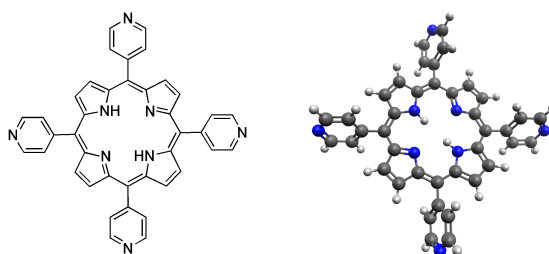


Figure 60: Structure of 5,10,15,20-Tetra(4-pyridyl)-21H,23H-porphine, four pyridine groups (“pyridil”) are attached to the central porphine complex. In the break-junction measurements the connection to the Au is performed by the nitrogen of the pyridil.

For the preparation of the porphyrines a 0.02 mM solution of porphyrine in chloroform was prepared, and pyridine was added to the solvent to increase the solubility and to stabilize the porphyrine in the chloroform (see Chap. 3.5) [5].

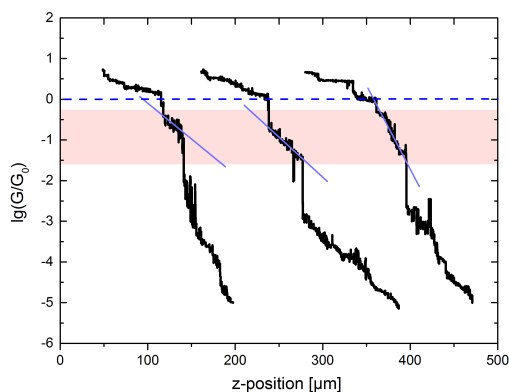


Figure 61: CPCs of TPyP usually do not exhibit a single clear pronounced plateau below G_0 , but “tilted” plateaus around $G_{\text{TPyP}} \approx 0.1 G_0$.

Typical examples of CPCs of tetrapyrrolic-porphine (TPyP) are shown in Fig. 61. No clearly pronounced molecular plateau can be observed below G_0 . However, often the CPCs show a kind of “tilted plateau” in the regime of $0.1 G_0$. This tilted plateau is terminated by an abrupt drop in the conductance to a value of $\sim 10^{-3} G_0$, followed by a further tunneling-like decrease of the conductance. Both, a plateau and the abrupt drop in the conductance are strong indications for the presence of molecules between the Au contacts. However, due to our experience with the preparation of the porphyrine and the knowledge about the pyridine-Au contact our interpretation is as follows:

- TPyP tends to cluster even if we use extremely low concentrations. Therefore, we believe that a cluster of TPyP molecules is formed and shunts the contact.
- In contrast to thiol, pyridine develops only a weak contact to Au. Moreover due to the clustering, there will be a number of Au-pyridine contacts, which leads to the large conductance value.
- Typically one contact (right or left) will be stronger. Therefore, the weaker contact will break and the molecular cluster will “slide” along this contact which leads to the tilting of the plateau.
- Finally, the cluster will be removed from the “weak contact”. This leads to the sudden drop of the conductance, since now tunneling sets in. However, different to the experiments with TPT, no chain-like structure of Au atoms is pulled out of the electrode and thus no reorientation of the electrodes takes place. Therefore this drop in conductance is not as large as for TPT (typically to $10^{-6} G_0$)

Obviously the clustering of molecules hampers the measurement since

- we have to choose very small concentrations of TPyP in chloroform,
- the clusters are less mobile and therefore the chance of detecting molecules is small in our experiment.
- If molecules are measured (tilted plateau) then these are not single molecule measurements.

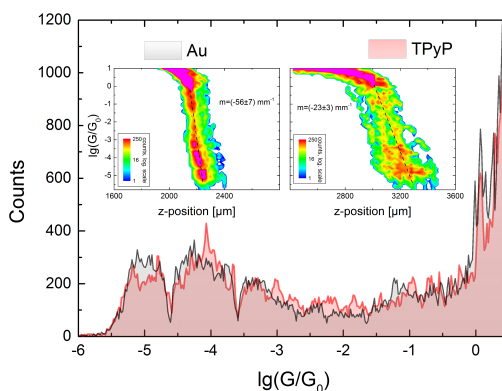


Figure 62: Two standard histograms of an Au bridge without (black) and with TPyP molecules (red) show nearly similar behavior. However, the contour histograms (insets) reveal a difference, although no clear plateaus are detectable for this measurement.

However, with the help of contour histograms the effect of TPyP on the CPCs can be observed even though the standard histograms are not very helpful. Fig. 62 shows a comparison of standard histograms of a break-junction without molecules and with TPyP. While the histograms do not provide notable differences, the contour histograms (insets) of the same data indicate a change in the breaking behavior of the Au bridge if molecules are deposited. The main difference between both contour histograms lies in the width of the contours. In case of measurement with TPyP a large range of possible scenarios occur, ranging from CPCs without molecules in the junction to CPC with different arrangement and sizes of clusters of TPyP. Since the interpretation of CPCs or single histograms is difficult, general mechanisms can be investigated if a large number of measurements are performed at changing conditions.

Therefore, in these measurements the temperature can play an important role. By cooling down the sample, the mobility of the molecules and clusters of molecule decreases and the situation might occur that molecules are “stuck” in the junction and, thus, measured repeatedly. Temperature dependence measurements could reveal whether the formation of clusters or the flexibility of single molecules caused the “tilted plateaus”. Therefore, contour histograms were recorded at different temperatures ranging from 30 K up to room temperature. As expected, the form of the contour histogram of TPyP differ for every measurement, however, at lower temperatures more often stable regimes can be obtained. Fig. 63 shows two contour histograms, for TPyP at 290 K and 155 K, respectively. While for the latter histogram a dense region of conductance values around $(10^{-1}-10^{-2})G_0$ is clearly observed, the contour histogram recorded at room temperature does not reveal such significant behavior. However, it is clearly visible that both contour histograms can be distinguished from those without molecules. The difference is not only given by the peaks that are characteristic for the presence of the molecules (e.g. around $(0.1-0.01)G_0$ in Fig. (63 b)) but also by the slope of the line that connects the maxima in the contour plot (see lines in Fig. 62 and 63).

The lines in the semi logarithmic plots represent the average slope of all CPCs, i.e. the decay constant of an assumed pure tunneling mechanism. Using the attenuation factor, the resulting decay constants $\delta(\text{TPyP}) \approx 0.39$ for the measurements with TPyP are clearly below those for vacuum tunneling, see Fig. 64, i.e. the molecular contribution is clearly visible. Furthermore, the decay constant appears to be temperature independent. While the fitting procedure might not reveal a reliable “tunnel decay constant”, it is certainly a proof for the presence of molecules. The low value

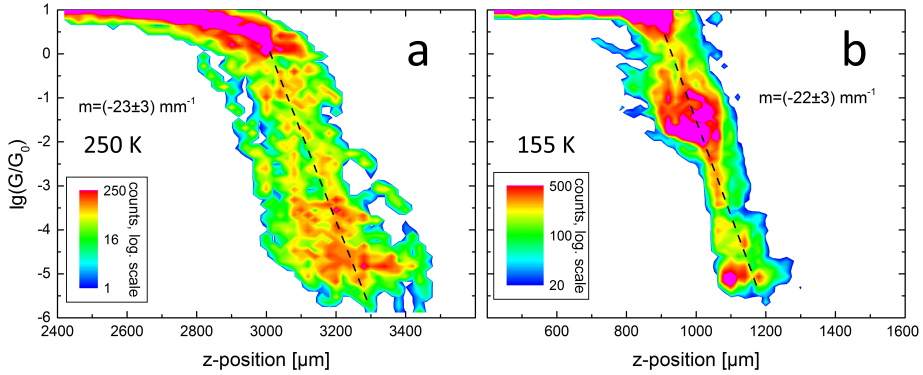


Figure 63: Contour histograms of TPyP at 290K (a) and 155K (b). The form of the contour histograms differ significantly for measurements of TPyP. The tendency to observe a regime of high conductances (b) enhances with decreasing temperature. However, both contour histograms show an averaged tunnel decay constant that differ from vacuum tunneling, $\delta_{290\text{K}}(\text{TPyP}) = (0.41 \pm 0.05) \text{ \AA}^{-1}$ and $\delta_{155\text{K}}(\text{TPyP}) = (0.39 \pm 0.05) \text{ \AA}^{-1}$.

indicates the strong effect of TPyP on the measured conductance. Mainly two mechanisms can cause the observed difference in the decay constant from vacuum tunneling, molecular plateaus in the CPCs and a lower work function due to the presence of molecules on the gold. Since the work function can be considered to be nearly temperature independent, the unchanging decay constant δ indicates that the breaking behavior of the system does not change (significantly) with the temperature. This enhances the probability that clusters dominate the breaking process.

Since histograms (CPCs) mainly provide information about the electronic properties of the metal-molecule bonds, IVCs have to be performed in order to learn more about the electronic properties of the molecule itself. However, as described above, in case of TPyP clustering of molecules in the junction is most likely. Therefore, also the IVC have to be taken with care, they might reflect the electronic properties of TPyP clusters.

Nevertheless, IVCs are recorded at different temperatures. At higher temperatures all IVCs exhibit a similar behavior, see Fig. (65 a). For one direction of the applied voltage (in this case negative) a relatively slow change of the current is measured, whereas in the opposite voltage regime a stronger increase is observed. Generally, the expected linear behavior is observed up to several 100 mV, before the slope of the curve in the positive voltage range changes to finally $I \propto V^4$ (see inset of Fig. (65 a)). RTM fits yield values for the molecular levels clearly below 1 eV ($\epsilon_{l,290\text{K}}(\text{TPyP}) \approx 0.6 \text{ eV}$ and $\epsilon_{r,290\text{K}}(\text{TPyP}) \approx 0.7 \text{ eV}$) and values for the coupling of $\Gamma_{l,290\text{K}}(\text{TPyP}) \approx \Gamma_{r,290\text{K}}(\text{TPyP}) \approx -2 \times 10^{-5} \text{ eV}$. At high voltages strong fluctuations are observed. As a result the RTM fits are less accurate ($r \approx 0.97$).

At lower temperatures the deviation from the RTM fit increases. A typical example of an IVC recorded at $T \approx 185 \text{ K}$ is shown in Fig. (65 c). Although the reduced temperatures in general leads to a stabilization of the IVC, fluctuations are observed in the regime where the voltage increases. Nevertheless, the RTM fit yields similar values compared to those measured at room temperature ($\epsilon_{l,185\text{K}}(\text{TPyP}) \approx 0.9 \text{ eV}$, $\epsilon_{r,185\text{K}}(\text{TPyP}) \approx 0.7 \text{ eV}$). The double-logarithmic plot of the IVC shows, that at this temperature the linear regime at low voltages is finally transferred to a $I \propto V^7$ dependence at high voltages. Obviously, this dependence cannot be fitted with RTM. The reason for this strong current dependence of the IVC might be a direct contribution of one or more molec-

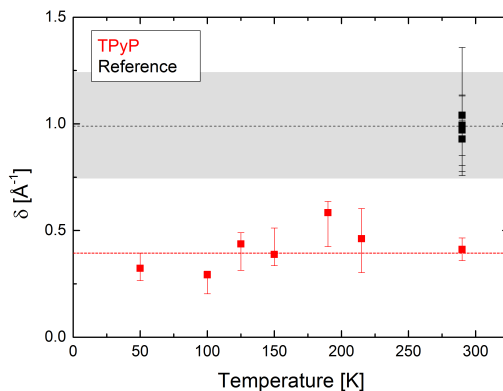


Figure 64: Decay constant of TPyP (red) $\delta(\text{TPyP}) \approx 0.39$, obtained from slopes in the contour histograms at different temperatures. The values are clearly below the value of the reference measurements without molecule, i.e. for vacuum tunneling (black).

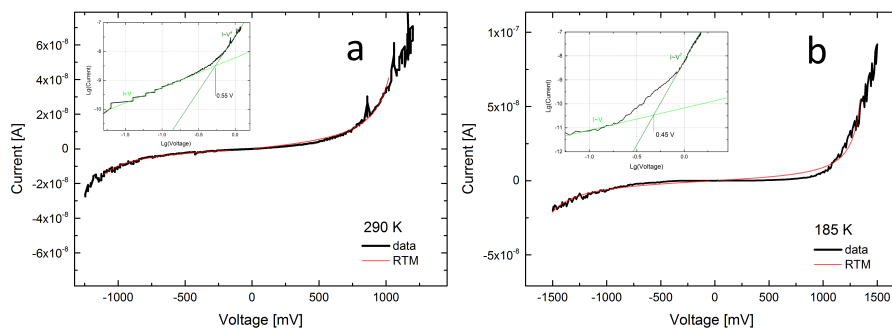


Figure 65: Exemplary IVCs of TPyP at room temperature (a) and 185 K (b). The black line represents the experimental data, the red line is the RTM fit. The insets show the same data in double-logarithmic form.

ular orbitals that open additional conductance channels. If inelastic transport occurs, the strong increase in current at high voltages would lead to local heating of the molecule and the Au contact.

The IVCs of TPyP at even lower temperature provide further insights. The measurement becomes visibly more stable and the IVCs of TPyP reveal an astonishing behavior. The basic form of the curve is similar to the IVCs in Fig. 65, however, a clear point of inflection can be observed. In order to use the derivatives as a method of investigation, the IVC is smoothed (e.g. moving average using 5 values) without changing the general features (cf. red lines in Fig. 66) to evaluate the first derivative.

An overview of IVCs, measured from 290 K down to 70 K is shown in Fig. 66. Similar to the IVCs recorded at higher temperatures, the curves are strongly asymmetric, however, for 155 K a kink in the IVC is visible (see Fig. 66). While for the higher temperatures the derivatives of the IVC are not helpful, for the IVC measured at $T = 155$ K clearly pronounced peaks occur in the second derivative. For example, the IVC measured at 130 K exhibits a clear plateau, and in the first derivative a small range of negative differential resistance is visible around 0.8 V. While for the first and second derivative small fluctuations (resulting from numerical procedure) are visible, two major peaks, at $E_1 \approx (400 - 450)$ mV and $E_2 \approx (1100 - 1300)$ mV are clearly pronounced. A similar behavior is observed for the IVC measured at 70 K. It seems that the peak(s) observed at low temperatures shift to higher voltages above 130 K. The peaks might be caused electronically or by molecular vibrations [26]. These interesting modes are only measured at low temperatures ($T \lesssim 180$ K), therefore one explanation could be, that at high temperatures the molecules are mobile and rearrange in the cluster which leads to the strong fluctuations. At low temperatures the cluster of molecules is stable, therefore the energy values of electronical or vibrational modes of the molecular cluster can be resolved.

In conclusion, tetrapyrrolic-porphine is an interesting molecular system that reveals a much more complex behavior than simple molecules (like hexanedithiol). In our break-junction experiments no clear pronounced plateaus are visible. Instead “tilted plateaus” in the CPCs are observed for relatively high conductances in the range of $(0.01 - 0.1) G_0$. These conductance values seem to characterize the bond between clusters of TPyP and the Au electrodes. Therefore a large range of scenarios (variations of the location and size of a cluster or single molecules) lead to a quite broad contour histogram. The lower limit of the conductance regime (the tilted plateaus) might indicate the “conductance value” for TPyP. This would lead to $G(\text{TPyP}) \approx 3 \times 10^{-2} G_0$. This value might be the conductance of a cluster of porphyrines (not a single molecule) or it might characterize in great part the anchoring groups. However, small plateaus are occasionally observed for conductances around $(10^{-4} - 10^{-5}) G_0$ which could be the conductance of the molecule only contacted weakly by its pyridil groups to the Au electrodes. The observed behavior of the CPCs coincides with the literature. In [43] measurements on similar porphyrines are performed, where the same effects (tilted plateaus, a high conductance region) in equal conductance ranges are observed.

Due to the complex behavior standard histograms do not reveal differences to the reference measurements. In contrast, the contour histograms show a broadening and a different average slope. This slope is two times smaller than that for vacuum tunneling, which is caused by (tilted) plateaus and the change of the work function of gold. Hence, it is a clear indication that TPyP influences the breaking process significantly. The averaged decay constant maintains its low value for the measured temperature range between (30–290) K, i.e. the breaking process remains relatively stable.

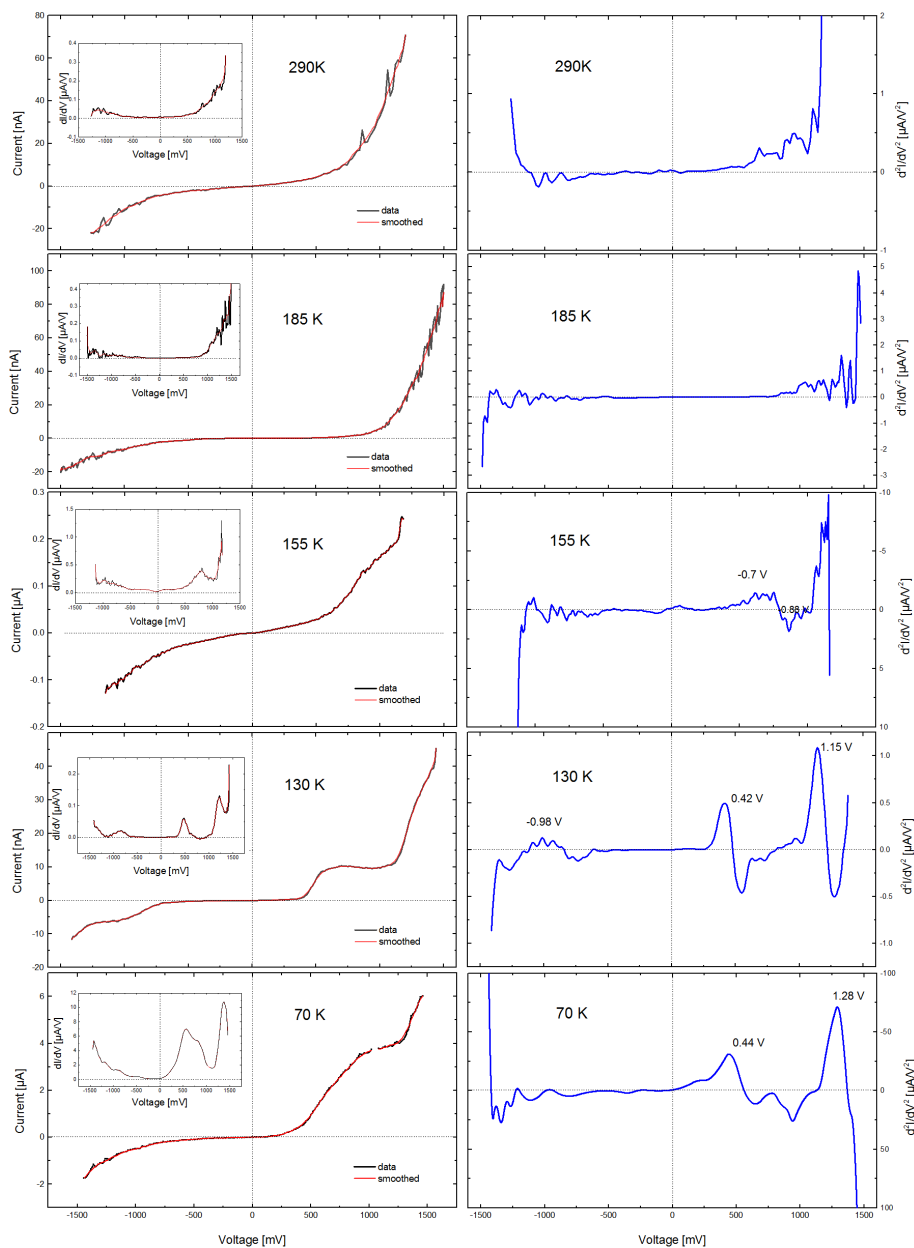


Figure 66: IVCs of TPyP recorded at different temperatures. Left side: original data (black), smoothed data (red, moving average using 5 data points) and first derivative (inset, data and smoothed data). Right side: second derivative (blue).

IVCs are measured up to 1.5 V. At high temperatures and high voltages the IVCs are unstable which maybe due to the complex structure of one, or several clustered TPyP molecules leading to geometrical dependent conductance switching. At lower temperatures less fluctuations are visible in the IVC, maybe due to reduced mobility of the molecules.

The form of the IVC depends on the temperature. For high temperatures the IVC are fitted with the RTM, and a molecular orbital of approximately $\epsilon_{290\text{ K}}(\text{TPyP}) \approx (0.65 \pm 0.1) \text{ eV}$ is obtained for both, negative and positive voltage. At lower temperatures (185 K) the IVC form changes, i.e. the increase of the current with voltage is stronger, and the RTM can only be fitted with lower accuracy, nevertheless the molecular level for the analyzed IVCs is relatively close to the level obtained at room temperature ($\epsilon_{185\text{ K}}(\text{TPyP}) \approx (0.8 \pm 0.1) \text{ eV}$ for both voltages). The coupling constant remains nearly unchanged for all IVCs ($\Gamma_{(185/290)\text{ K}}(\text{TPyP}) \approx (-2 \pm 0.2) \times 10^{-5} \text{ eV}$). The form of the IVCs corresponds approximately to the literature [43].

At even lower temperatures, starting below $\sim 155 \text{ K}$, the form of the IVC is completely changed. Sharp step- and plateau-like features are observed. This behavior cannot be fitted with the RTM, however, the second derivative yields at least two clear peaks around 0.4 eV and 1.2 eV. The exact values depend on the temperature, starting at 130 K it seems that they shift to higher voltages with increasing temperature. The origin of these peaks can be either electronical or vibrational modes [26, 35, 53].

5 Summary

Nowadays, the investigation of single molecules represents a cutting edge of science, that combines the two traditional disciplines, physics and chemistry. Besides of curiosity and the search for knowledge, certainly solid reasons to investigate the electronic properties of complex molecular systems, more practical reasons exist. Despite their importance several aspects are not well understood like the electron pathway in proteins or the possibility to use (single) molecules as part of electronic systems of the future.

The mechanically controllable break-junction (MCBJ) technique represents an ideal way for the investigation of single molecules. Despite its simple working principle the control and stable measurements of single molecules are possible. In this thesis, the first steps towards characterizing single molecules via a cryogenic version of a MCBJ setup is performed using different molecules as a test bed ranging from more rod-like “one-dimensional” molecules to complex porphyrines.

A major part of the thesis was the development and operation of an automated cryogenic MCBJ setup, the optimization of the break-junction samples themselves, and to establish adequate measurement procedures. In detail:

- A cryogenic setup was developed and the sophisticated sample holder was constructed and implemented. Electronic setup and devices were optimized to reach the necessary precision for the measurement of the low conductances of $\sim 10^{-7} G_0$, typically equal to $\sim 10^{-13} A$. The piezo positioner allows a lateral control of the break-junction (theoretically) in the pm regime, thanks to an attenuation factor of $\sim 10^{-6}$.
- The temperature control, different types of measurement cycles (e.g. CPC, IV and histogram) and the bending procedure were automatized in a self-written program that allows maximum flexibility.
- Optimal lithographically prepared samples allow several thousands of bending procedures and can be used for several weeks or even months of continuous measurement. In order to improve the bending process the production steps were changed several times and different sizes and materials for the substrate were tested. Furthermore, several patterns for the (e-beam) lithographic structure were developed. Palladium (Pd) and gold (Au) were tested as electrode materials.

With the completed systems, different molecules were characterized. First, two simple molecules were investigated: Hexanedithiol (HDT), an alkane which has a rod-like “1-dimensional” structure, and the most simple aromatic dithiol, benzenedithiol (BeDT). The main results are:

- In contrast to the Pd samples, those with Au electrodes turned out to be suitable for break-junction measurements. Therefore, Au was used for all measurements later on. The Au nano bridge can be controlled with remarkable precision and the conductance of an open break-junction is stable for days, especially at low temperatures. Mounting and electrical connecting turned out to be crucial, since the nano bridges were easily destroyed by electric charges. Hence, the connecting process was improved and different connection methods were tested.
- HDT turned out to be a suitable molecule for conductance–position characteristics (CPCs). It produced highly stable conductance plateaus at $\sim 5.8 \times 10^{-4} G_0$. BeDT shows a more complex behavior, since several plateaus were detected at high conductance values in the CPCs.

Both results agree with the literature values. Furthermore, current–voltage characteristics (IVCs) were performed up to 1 V for HDT and BeDT. A significant s-shape was observed, and a molecular level of $\epsilon(\text{HDT}) \approx 0.9$ eV and $\epsilon(\text{BDT}) \approx 0.5$ eV could be extracted for HDT and BeDT, respectively.

- Our analysis revealed that the contact between molecule and electrodes plays a major role in our experiment. On the one hand, the detection of molecules via plateaus in CPC depends highly on the ability to pull a chain-like atomic structure out of the electrodes. On the other hand, the measured conductance seems to be dominated by the large resistance of the contact of the anchoring groups to the electrodes. Hence, all conductance data obtained from CPCs or histograms reflect the contact resistance. Usually, only the data obtained via IVCs (i.e. higher voltages) provide specific information about the level of the molecule.

Finally, more complex molecules were investigated at different temperatures. The relatively long conjugated terphenyldithiol (TPT) and the “2-dimensional” conjugated tetrapyridilporphine (TPyP):

- The temperature dependence turned out to be a crucial aspect for the stability of the measurements and the characterization of molecules. The plateaus in the CPCs and the IVCs are more stable at cryogenic temperatures.
- Although TPT exhibited different stable plateaus in the CPCs, only one conductance was visible in all CPCs with a molecule. The value of this conductance (of the molecule-Au contact) is nearly constant at temperatures lower than $T \approx 100$ K, where it starts to increase. At this temperature a transition from coherent tunneling to incoherent “hopping” takes place. In contrast, the values for the molecular orbital extracted from the IVCs did not exhibit any temperature dependence.
- TPyP shows no clearly pronounced plateaus in the CPCs, however, tilted plateaus are observed regularly. This could be caused by (a) the tendency of this molecule to form clusters, which was observed by the scanning electron microscope (SEM), and (b) by the less effective bonding of the pyridil to Au (for TPyP) compared to that of the thiol to Au (for TPT). The tilted plateaus at high conductance would then describe the behavior of a cluster of TPyP that is bonded to one electrode and “slides” over the second electrode. Since in this case the standard histogram does not show pronounced peaks a contour histogram was introduced. The plateaus and the lower work function influence the CPCs, which appear in the contour histogram in form of a modified tilting of the contours with respect to the contour histograms of a reference measurement without molecules. At lower conductance sometimes small plateaus were observed that might be caused by single porphyrines. Finally, IVCs of TPyP were recorded for different temperatures. While at higher temperatures the IVCs exhibit a strong, but very noisy increase at higher voltages, this increase changes to a plateau-like form at lower temperatures. I.e. the IVCs are stable and reproducible. The 2nd derivative (d^2I/dV^2) shows pronounced peaks around 0.4 eV and 1.2 eV at low temperatures. Above ~ 130 K these peaks shift towards higher voltages with increasing temperature, until at ~ 180 K the peaks are covered by the voltage noise. Explanations for this peak are either vibrational or electronical modes, the voltage noise at higher temperature might be indicative for rearrangements of individual molecules in the cluster or at the Au electrode.

In conclusion, the automated cryogenic setup for mechanically controllable break-junction experiments was successfully developed. Single molecules could be characterized over a large temper-

ature range and the detection of molecular features seemed to be improved by the reduction of the temperature.

The electronic characterization of single molecules is of general interest for the understanding of charge transfer on molecular levels and future molecular electronics. If implemented in electrical circuits they could mimic or even improve the properties of conventional devices. However, our measurements also reveal some important aspects that have to be considered. Especially, the contact between molecule and electrode plays a crucial role regarding its large resistances and the alignment of its Fermi level with the molecular orbitals. At the low voltages, which are usually used in CPC and histograms, instead of the molecule itself the molecule-metal contact is often characterized. Furthermore, even though the single molecules are stable for a long time (minutes to hours in our experiment) in real electronic devices they have to be stable for a much longer period.

Nevertheless, the cryogenic MCBJ provides an elegant way to detect interesting electronic properties of single molecules and hence can contribute to basic science as well as to the development of future technologies.

6 Danksagung

Zum Abschluss möchte ich einigen Personen danken ohne die diese Arbeit nicht möglich gewesen wäre. Meinem Doktorvater Prof. Dr. Roger Wördenweber möchte ich für die hervorragende Betreuung und sein großes Interesse während der gesamten Zeit in Jülich danken. Prof. Dr. Ulrich Deiters danke ich für die Bereitschaft die Zweitkorrektur dieser Arbeit übernommen zu haben. Ein herzlicher Dank geht auch an Dr. Dirk Mayer, der die chemische Seite der Arbeit mit mir viele Male diskutiert hat, und an alle Mitglieder unserer Arbeitsgruppe:

“Tovarisch” Dr. Eugen Hollmann für seine Diskussionsbereitschaft und seine ausgezeichneten experimentellen Improvisationsfähigkeiten, Rolf Kutzner für seine ständige Hilfe und die netten Gespräche über FC und kulinarische Spezialitäten, Kirill für seine Freundschaft während unseres gemeinsamen Diplomanden- und Doktorandendaseins als Bürokollegen und für die interessante Reise in die Ukraine. 同志Biya, 同志Yang und “Tovarisch” Sascha möchte ich für die zahlreichen Gespräche und Diskussionen über Wissenschaft und Sprache, insbesondere Chinesisch, Russisch und Kölsch danken, und auch für den hervorragend gebastelten Doktorhut. Zahlreichen Kollegen aus meinem Institut welche die Arbeit oder die Mittagspause interessanter gestaltet haben möchte ich ebenfalls danken, sowie Andi für chemische Diskussionen.

Der Bonn Cologne Graduate School und Dr. Petra Neubauer möchte ich für die herzliche Aufnahme und das Stipendium danken.

Weiterhin möchte ich den wichtigen Personen aus meinem privaten Umfeld danken: An erster Stelle meinen lieben Eltern, die mich immer unterstützt haben und auch immer hinter mir standen, meiner Schwester Rebekka (auch für das Korrekturlesen) und meinem Bruder Simon auf die ich mich immer verlassen konnte und kann, sowie meiner Tante Bärbel. Auch meinen langjährigen Freunden möchte ich herzlich dafür danken dass auf sie immer Verlass ist (insbesondere aber Ben und Babs, Phil und Steffi, Georg, Biene, Norah, Volker, Saskia und Pascal, Jan, Anne und Christian). Allen Freunden die mir bei der Korrektur dieser Arbeit geholfen haben (vor allem Harald und Vicky) gilt natürlich ein besonderer Dank. Zu guter Letzt möchte ich meiner Freundin Katharina danken die mich seit vielen Jahren immer unterstützt und mir auch in schwierigen Zeiten stets mit Liebe zur Seite stand.

References

- [1] ANPz101 positioner, Attocube, 2014, <http://www.attocube.com/attomotion/premium-line/anpx51-24/>.
- [2] DIY Wiki, 2014, <http://wiki.diyfaq.org.uk>.
- [3] Lexikon Spektrum der Wissenschaft, 2014, <http://www.spektrum.de/lexikon/physik/gold/6013>.
- [4] PI 2600 Process Guide, HD Microsystems, 2009, http://www.hdmicrosystems.com/HDMicroSystems/en_US/pdf/PI-2600_ProcessGuide.pdf.
- [5] Private communication, Dr. Sabine Willbold, 2014.
- [6] Produktinfos, Allresist, 2014, http://www.allresist.com/wp-content/uploads/sites/2/2014/02/allresist-produktinfos_ar-p630-690_englisch.pdf.
- [7] SMU 2635B, Keithley Instruments, 2014, <http://www.keithley.com/products/dcac/currentvoltage/2600B/?m>.
- [8] Thomson Reuters Web of Knowledge, 2013, <http://www.scienceofknowledge.com>.
- [9] AVIRAM, A., AND RATNER, M. A. Molecular rectifiers. *Chemical Physics Letters* 29 (1974), 277–283.
- [10] BÜTTIKER, M. Role of quantum coherence in series resistors. *Physical Review B* 33 (1986), 3020–3026.
- [11] BÜTTIKER, M. Scattering theory of current and intensity noise correlations in conductors and wave guides. *Physical Review B* 46 (1992), 12485–12507.
- [12] CUEVAS, J., AND SCHEER, E. *Molecular Electronics: An Introduction to Theory and Experiment*. World Scientific Publishing Company, Incorporated, 2010.
- [13] DADOSH, T., GORDIN, Y., KRAHNE, R., KHIVRICH, I., MAHALU, D., FRYDMAN, V., SPERLING, J., YACOBY, A., AND BAR-JOSEPH, I. Measurement of the conductance of single conjugated molecules. *Nature* 436 (2005), 677–680.
- [14] EMERY, R., LENSHEK, D., BEHIN, B., GHERASIMOVA, M., AND POVIRK, G. Tensile behavior of free-standing gold films. In *Symposium I - Polycrystalline Thin Films - Structure, Texture, Properties* (1997), vol. 472 of *MRS Proceedings*.
- [15] FLIESSBACH, T. *Quantenmechanik*. Bibliographisches Institut Wissenschaftsverlag, 1991.
- [16] GALPERIN, M., RATNER, M. A., AND NITZAN, A. Molecular transport junctions: vibrational effects. *Journal of Physics: Condensed Matter* 19 (2007), 103201.
- [17] GHOSH, A., MAHATO, P., CHOUDHURY, S., AND DAS, A. Comparative study of porphyrin derivatives in monolayers at the air-water interface and in Langmuir-Blodgett films. *Thin Solid Films* 519, 22 (2011), 8066 – 8073.
- [18] GUNDLACH, K. Zur Berechnung des Tunnelstroms durch eine trapezförmige Potentialstufe. *Solid-State Electronics* 9 (1966), 949–957.

- [19] HAISS, W., VAN ZALINGE, H., BETHELL, D., ULSTRUP, J., SCHIFFRIN, D. J., AND NICHOLS, R. J. Thermal gating of the single molecule conductance of alkanedithiols. *Faraday Discussions* 131 (2006), 253–264.
- [20] HINES, T., DIEZ-PEREZ, I., HATH, J., LIU, H., WANG, Z.-S., ZHAO, J., ZHOU, G., MÜLLER, AND TAO, N. Transition from tunneling to hopping in single molecular junctions by measuring length and temperature dependence. *Journal of the American Chemical Society* 132 (2010), 11658–11664.
- [21] HONG, S., REIFENBERGER, R., TIAN, W., DATTA, S., HENDERSON, J., AND KUBIAK, C. Molecular conductance spectroscopy of conjugated, phenyl-based molecules on Au(111): the effect of end groups on molecular conduction. *Superlattices and Microstructures* 28 (2000), 289–303.
- [22] HUISMAN, E. H., GUÁDON, C. M., VAN WEES, B. J., AND VAN DER MOLEN, S. J. Interpretation of transition voltage spectroscopy. *Nano Letters* 9 (2009), 3909–3913.
- [23] JUHANIEWICZ, J., AND SEK, S. Peptide molecular junctions: Distance dependent electron transmission through oligoprolines. *Bioelectrochemistry* 87 (2011), 21–27.
- [24] KARTHÄUSER, S. Control of molecule-based transport for future molecular devices. *Journal of Physics: Condensed Matter* 23 (2011), 13001.
- [25] KIGUCHI, M., NAKASHIMA, S., TADA, T., WATANABE, S., TSUDA, S., TSUJI, Y., AND TERAOKA, J. Single-molecule conductance of π -conjugated rotaxane: New method for measuring stimulated electric conductance of π -conjugated molecular wire using STM break junction. *Small* 8 (2012), 726–730.
- [26] KUBATKIN, S., DANILOV, A., HJORT, M., CORNIL, J., BREDAS, J.-L., STUHR-HANSEN, N., HEDEGARD, P., AND BJORNHOLM, T. Single-electron transistor of a single organic molecule with access to several redox states. *Nature* 425 (2003), 698–701.
- [27] LANDAU, L., AND LIFSHITZ, E. *Quantum Mechanics: Non-relativistic Theory*. Butterworth-Heinemann, 1977.
- [28] LANGRETH D.C., DEVREESE J.T., V. D. V. Linear and nonlinear electron transport in solids. *NATO Advanced Science Institutes Series* 17 (1976), 634.
- [29] LEE, W., AND REDDY, P. Creation of stable molecular junctions with a custom-designed scanning tunneling microscope. *Nanotechnology* 22 (2011), 485703.
- [30] LI, Z., AND BORGUET, E. Determining charge transport pathways through single porphyrin molecules using scanning tunneling microscopy break junctions. *Journal of the American Chemical Society* 134 (2012), 63–66.
- [31] LIDE, D. R. *CRC Handbook of Chemistry and Physics*. CRC Press, 2007.
- [32] LINDSAY, S., AND RATNER, M. Molecular transport junctions: clearing mists. *Advanced Materials* 19 (2007), 23–31.
- [33] LINDSAY, S. M. *Introduction to Nanoscience*, vol. 1. Oxford University Press, 2010.
- [34] LIU, S., WEISBROD, S. H., TANG, Z., MARX, A., SCHEER, E., AND ERBE, A. Direct measurement of electrical transport through G-quadruplex DNA with mechanically controllable break junction electrodes. *Angewandte Chemie - International Edition* 49 (2010), 3313–3316.

- [35] LIU, Z.-F., WEI, S., YOON, H., ADAK, O., PONCE, I., JIANG, Y., JANG, W.-D., CAMPOS, L. M., VENKATARAMAN, L., AND NEATON, J. B. Control of single-molecule junction conductance of porphyrins via a transition-metal center. *Nano Letters* 14 (2014), 5365–5370.
- [36] LONG, Y.-T., ABU-IRHAYEM, E., AND KRAATZ, H.-B. Peptide electron transfer: more questions than answers. *Chemistry* 11 (2005), 5186–5194.
- [37] MARCUS, R. A. Electron transfer reactions in chemistry. theory and experiment. *Review of Modern Physics* 65 (1993), 599–610.
- [38] MATSUHITA, R., HORIKAWA, M., NAITOH, Y., NAKAMURA, H., AND KIGUCHI, M. Conductance and SERS measurement of benzenedithiol molecules bridging between Au electrodes. *The Journal of Physical Chemistry C* 117 (2013), 1791–1795.
- [39] MEIR, Y., AND WINGREEN, N. S. Landauer formula for the current through an interacting electron region. *Physical Review Letters* 68 (1992), 2512–2515.
- [40] MIRJANI, F., THIJSEN, J. M., AND VAN DER MOLEN, S. J. Advantages and limitations of transition voltage spectroscopy: A theoretical analysis. *Physical Review B* 84 (2011), 115402.
- [41] NOZAKI, D., GOMES DA ROCHA, C., PASTAWSKI, H., AND CUNIBERTI, G. Disorder and dephasing effects on electron transport through conjugated molecular wires in molecular junctions. *Physical Review B* 85 (2012), 155327.
- [42] PÄIVÄNRANTA, B., LANGNER, A., KIRK, E., DAVID, C., AND EKINCI, Y. Sub-10 nm patterning using EUV interference lithography. *Nanotechnology* 22 (2011), 375302.
- [43] PERRIN, M. L., MARTIN, C. A., PRINS, F., SHAIKH, A. J., EELKEMA, R., VAN ESCH, J. H., VAN RUITENBEEK, J. M., VAN DER ZANT, H. S. J., AND DULIC, D. Charge transport in a zinc-porphyrin single-molecule junction. *Beilstein Journal of Nanotechnology* 2 (2011), 714–719.
- [44] QI, Y., QIN, J., ZHANG, G., AND ZHANG, T. Breaking mechanism of single molecular junctions formed by octanedithiol molecules and Au electrodes. *Journal of the American Chemical Society* 131 (2009), 16418–16422.
- [45] RAMMER J., S. H. Quantum field-theoretical method in transport theory of metals. *Review of modern physics* 58 (1986), 323.
- [46] REED, M. A. Inelastic electron tunneling spectroscopy. *Materials Today* 11 (2008), 46–50.
- [47] SAKAI, M., YAMAUCHI, H., NAKAMURA, M., AND KUDO, K. Fabrication of organic conductive wires and molecular break junction. *Journal of Physics: Conference Series* 358 (2012), 012011.
- [48] SCHEER, E., BELZIG, W., NAVEH, Y., DEVORET, M. H., ESTEVE, D., AND URBINA, C. Proximity effect and multiple Andreev reflections in gold atomic contacts. *Physical Review Letters* 86 (2001), 284–287.
- [49] SCHRÖDINGER, E. Quantisierung als Eigenwertproblem i. *Annalen der Physik* 79 (1926), 361–376.
- [50] SCHRÖDINGER, E. Quantisierung als Eigenwertproblem ii. *Annalen der Physik* 79 (1926), 489–527.

- [51] SCHRÖDINGER, E. Quantisierung als Eigenwertproblem iii. *Annalen der Physik* 80 (1926), 734–756.
- [52] SCHRÖDINGER, E. Quantisierung als Eigenwertproblem iv. *Annalen der Physik* 81 (1926), 109–139.
- [53] SEDGHI, G., GARCIA-SUAREZ, V. M., ESDAILE, L. J., ANDERSON, H. L., LAMBERT, C. J., MARTIN, S., BETHELL, D., HIGGINS, S. J., ELLIOTT, M., BENNETT, N., MACDONALD, J. E., AND NICHOLS, R. J. Long-range electron tunnelling in oligo-porphyrin molecular wires. *Nature Nanotechnology* 6 (2011), 517–523.
- [54] SON, J. Y., AND SONG, H. Molecular scale electronic devices using single molecules and molecular monolayers. *Current Applied Physics* 13 (2013), 1157 – 1171.
- [55] SONG, H., KIM, Y., JEONG, H., REED, M. A., AND LEE, T. Coherent tunneling transport in molecular junctions. *The Journal of Physical Chemistry C* 114 (2010), 20431–20435.
- [56] SZE, S., AND NG, K. *Physics of Semiconductor Devices*. Wiley, 2006.
- [57] TAO, N. J. Electron transport in molecular junctions. *Nature Nanotechnology* 1 (2006), 173–181.
- [58] THIESS, A., MOKROUSOV, Y., HEINZE, S., AND BLÜGEL, S. Magnetically hindered chain formation in transition-metal break junctions. *Physical Review Letters* 103 (2009), 217201.
- [59] TIKHONOV, A., COALSON, R. D., AND DAHNOVSKY, Y. Calculating electron current in a tight-binding model of a field-driven molecular wire: Application to xylyl-dithiol. *Journal of Chemical Physics* 117 (2002), 567–580.
- [60] VAN RUITENBEEK, J. M., ALVAREZ, A., PIEYRO, I., GRAHMANN, C., JOYEZ, P., DEVORET, M. H., ESTEVE, D., AND URBINA, C. Adjustable nanofabricated atomic size contacts. *Review of Scientific Instruments* 67 (1996), 108–111.
- [61] VENKATARAMAN, L., KLARE, J. E., NUCKOLLS, C., HYBERTSEN, M. S., AND STEIGERWALD, M. L. Dependence of single-molecule junction conductance on molecular conformation. *Nature* 442 (2006), 904–907.
- [62] VOLLHARDT, K., SCHORE, N., AND BUTENSCHÖN, H. *Organische Chemie*. Wiley-VCH, 2011.
- [63] VROUWE, S. A. G., VAN DER GIESSEN, E., VAN DER MOLEN, S. J., DULIC, D., TROUWBORST, M. L., AND VAN WEES, B. J. Mechanics of lithographically defined break junctions. *Physical Review B* 71 (2005), 035313.
- [64] WAGNER, S., KISSLINGER, F., BALLMANN, S., SCHRAMM, F., CHANDRASEKAR, R., BODENSTEIN, T., FUHR, O., SECKER, D., FINK, K., RUBEN, M., AND WEBER, H. B. Switching of a coupled spin pair in a single-molecule junction. *Nature Nanotechnology* 8 (2013), 575–579.
- [65] XIAO, X., XU, B., AND TAO, N. Changes in the conductance of single peptide molecules upon metal-ion binding. *Angewandte Chemie International Edition* 43 (2004), 6148–6152.
- [66] XIAO, X., XU, B., AND TAO, N. Conductance titration of single-peptide molecules. *Journal of the American Chemical Society* 126 (2004), 5370–5371.

-
- [67] XU, B., AND TAO, N. J. Measurement of single-molecule resistance by repeated formation of molecular junctions. *Science* 301 (2003), 1221–1223.
- [68] ZHOU, C. AND MÜLLER, C., AND DESHPANDE, M. R. AND SLEIGHT, J. W. AND REED, M. A. Micro-fabrication of a mechanically controllable break junction in silicon. *Applied Physics Letters* 67 (1995), 1160–1162.

APPENDICES

A The Quantum of Conductance

If the size of a conductor becomes small enough that quantum effects cannot be ignored anymore, the situation can be analyzed sophisticatedly with time-dependent perturbation theory or scattering formalisms, detailed calculations can be found in Ref.[10] Here, a more intuitive way is introduced which leads to the same result.

The number of conducting electrons between two metal electrodes depends on the density of states of the electrons in the metal. An applied voltage shifts the Fermi level of one electrode with regard to the other and more electrons will contribute to the current. In a first approximation the voltage V opens the energy range by eV , the number of the electrons is proportional to the applied voltage and to the density of states

$$n = \frac{dn}{dE} eV = \frac{dn}{dk} \frac{dk}{dE} eV. \quad (36)$$

The averaged group velocity $|\vec{v}| = v$ of the electrons is

$$v := \frac{d\omega}{dk} = \frac{1}{\hbar} \frac{dE(k)}{dk}, \quad (37)$$

ω represents the angular frequency and k the wave number of the electron, respectively. Using Eq. (36), (37) and the density of states $dn/dk = (2\pi)^{-1}$ of a one dimensional structure, the absolute value of the net current density

$$I = nev \quad (38)$$

is given by

$$I = \left(\frac{1}{2\pi\hbar v} eV \right) 2ev = \frac{2e^2}{h} V. \quad (39)$$

Here, the factor 2 considers up and down spin states of the electrons. Eq. (39) provides a remarkable result. For the nano-contact the conductance changes in a step-like manner, and the proportional constant does not depend on material specific properties, like the density of states. Before we discuss this behavior in more detail, we introduce a more complex formula for the voltage dependent current of a small sample between two electrodes. The electronic states of the electrodes are described by the Fermi function $f(E)$. At zero temperature the electron states are filled up to the Fermi energy, and higher energy states are not occupied. The current between the electrodes can be expressed as an integral over the energy of the electrons

$$I(V) = \frac{2e}{h} \int_{-\infty}^{\infty} dE T(E) [f_L(E) - f_R(E)], \quad (40)$$

with f_L and f_R being the Fermi function of the left and right electrode, respectively. The most complex part is the energy dependent transmission probability $T(E)$ for the electrons. Eq. (40) is the simplest form of the Landauer formula, already introduced in the 1950's. In the case of zero temperature and low voltages the Landauer formula becomes

$$I = GV, \quad (41)$$

with a conductance of

$$G = \frac{2e^2}{h} T. \quad (42)$$

We can approximate the transmission probability T as the sum of N individual transmission channels T_n that have a value between 0 and 1. The conductance is

$$G = \frac{2e^2}{h} \sum_{n=1}^N T_n. \quad (43)$$

Consequently, the maximal conductance of one transmission channel is

$$G_0 := \frac{2e^2}{h}, \quad (44)$$

and is called the *quantum of conductance*. It is exactly the same result equation (39) provides.

$$G_0 \approx 77 \mu\text{S} \approx (13 \text{ k}\Omega)^{-1}. \quad (45)$$

B Chemical Analysis

1,6-Hexanedithiol

Elementary analysis:

Element	Measured % of weight	Theoretical % of weight
Carbon	47.83±0.27	47.95
Hydrogen	9.29±0.10	9.39

Table 4: Results of the elementary analysis of 1,6-hexanedithiol

Gas chromatography:

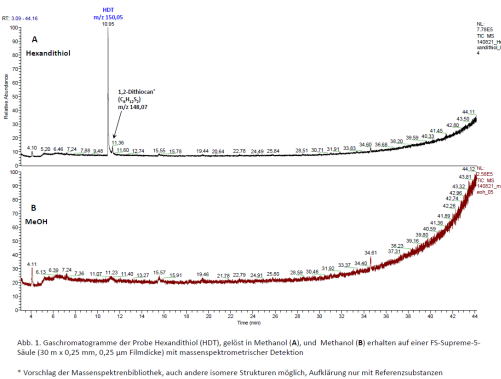


Figure 67: Chromatogram of 1,6-hexanedithiol

Position	Area [%]	Comment
10.95	94.83	HDT
11.36	5.17	Dithiocan

Table 5: Peaks of the gas chromatography of 1,6-hexanedithiol (Fig.67)

Benzene-1,4-dithiol

Elementary analysis:

Gas chromatography:

p-Terphenyl-4,4"-dithiol

Elementary analysis:

Gas chromatography

Element	Measured % of weight	Theoretical % of weight
Carbon	50.96±0.06	50.66
Hydrogen	4.22±0.01	4.25

Table 6: Results of the elementary analysis of benzene-1,4-dithiol

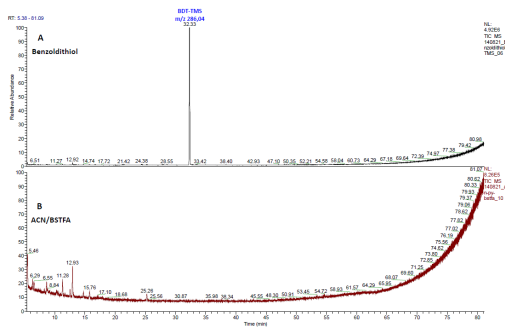


Figure 68: Chromatogram of benzene-1,4-dithiol

Position	Area [%]	Comment
32.33	100	Benzenedithiol

Table 7: Peaks of the gas chromatography of benzene-1,4-dithiol (Fig.68)

Element	Measured % of weight	Theoretical % of weight
Carbon	71.84±0.61	73.43
Hydrogen	4.80±0.02	4.79

Table 8: Results of the elementary analysis of p-terphenyl-4,4''-dithiol

Position	Area [%]	Comment
53.41	0.4	?
54.7	0.35	?
56.95	0.72	?
62.85	3.62	Terphenylthiol
66.79	1.75	?
76.89	93.17	Terphenyldithiol

Table 9: Peaks of the gas chromatography of p-terphenyl-4,4''-dithiol (Fig.69)

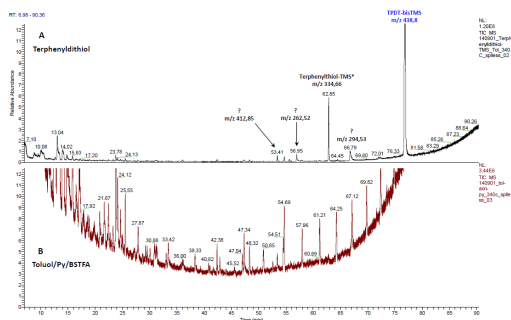


Abb. 3. Gaschromatogramme der Probe Terphenyldithiol-Bis(trimethyläthyl)ether (TPDT-bisTMS), gelöst in Toluol/Pyridin (Pg. A), und Toluol/Pyridin (B) erhalten nach Derivatisierung mit BSTFA auf einer FS-Supreme-5-Säule (30 m x 0,25 mm, 0,25 µm Filmdicke) mit massenspektrometrischer Detektion

* Strukturvorschlag auf Basis des Massenspektrums, Bestätigung nur mit Referenzsubstanzen möglich

Figure 69: Chromatogram of p-terphenyl-4,4''-dithiol

Element	Measured % of weight	Theoretical % of weight
Carbon	77.17±0.06	77.65
Hydrogen	4.41±0.15	4.24
Nitrogen	17.95±0.27	18.11

Table 10: Results of the elementary analysis of tetrapyrroline

5,10,15,20-Tetra(4-pyridyl)-21H,23H-porphines

Elementary analysis:

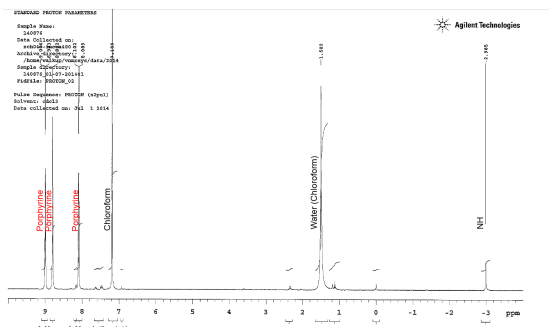


Figure 70: Proton-NMR of 5,10,15,20-tetra(4-pyridyl)-21H,23H-porphine solved in chloroform

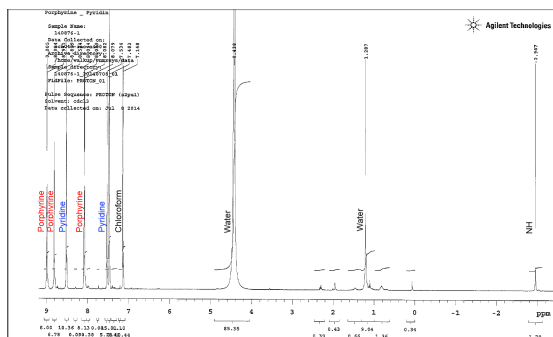


Figure 71: Proton-NMR of 5,10,15,20-tetra(4-pyridyl)-21H,23H-porphine solved in chloroform and pyridine (see Fig. (72) for details)

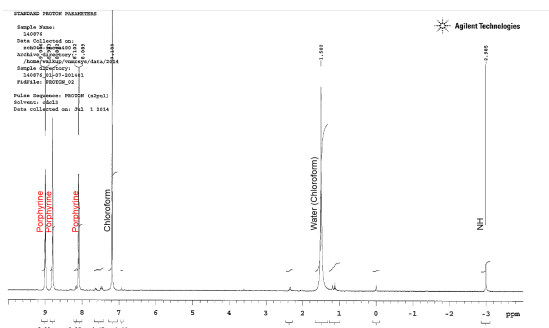


Figure 72: Proton-NMR of 5,10,15,20-tetra(4-pyridyl)-21H,23H-porphine solved in chloroform (detailed view of Fig. 71)

Band / Volume 85

Neutron Scattering

Experiment Manuals of the JCNS Laboratory Course held at Forschungszentrum Jülich and at the Heinz Maier-Leibnitz Zentrum Garching
edited by Th. Brückel, G. Heger, D. Richter, G. Roth and R. Zorn (2014),
ca. 195 pp
ISBN: 978-3-89336-966-9

Band / Volume 86

Development and Characterization of a Microfluidic Magnetic Oscillation Reactor for Enzymes

D. Jussen (2014), xxi, 131 pp
ISBN: 978-3-89336-974-4

Band / Volume 87

Submolecular imaging with single particle atomic force sensors

G. Kichin (2014), 140 pp
ISBN: 978-3-89336-976-8

Band / Volume 88

Multiscale Multimodel Simulation of Micromagnetic Singularities

C. Andreas (2014), xix, 188 pp
ISBN: 978-3-89336-983-6

Band / Volume 89

***Ab initio* description of transverse transport due to impurity scattering in transition-metals**

B. C. Zimmermann (2014), 164 pp
ISBN: 978-3-89336-985-0

Band / Volume 90

Ladungstransport durch Graphenschichten und GaAs-Nanodrähte untersucht mit einem Multispitzen-Rastertunnelmikroskop

S. Korte (2014), 96 pp
ISBN: 978-3-89336-990-4

Band / Volume 91

6th Georgian-German School and Workshop in Basic Science

A. Kacharava (Ed.) (2014), CD
ISBN: 978-3-89336-991-1

Band / Volume 92

***Ab initio* investigations of π -conjugated-molecule-metal interfaces for molecular electronics and spintronics**

M. Callsen (2014), viii, 155 pp
ISBN: 978-3-89336-992-8

Band / Volume 93

**Ladungstransportmessungen an Si(111) Oberflächen
mit einem Multispitzen-Rastertunnelmikroskop**

M. Blab (2014), iv, 132, X pp
ISBN: 978-3-89336-997-3

Band / Volume 94

Functional Soft Matter

Lecture Notes of the 46th IFF Spring School 2015
23 February – 06 March, 2015 Jülich, Germany
ed. by J. Dhont, G. Gompper, G. Meier, D. Richter, G. Vliegthart, R. Zorn
(2015), ca. 600 pp
ISBN: 978-3-89336-999-7

Band / Volume 95

**2-Steps in 1-pot: enzyme cascades for the synthesis
of chiral vicinal amino alcohols**

T. Sehl (2014), XIV, 167 pp
ISBN: 978-3-95806-001-2

Band / Volume 96

**Immunohistochemical and electrophysiological characterization of the
mouse model for Retinitis Pigmentosa, *rd10***

S. Biswas (2014), XII, 119 pp
ISBN: 978-3-95806-011-1

Band / Volume 97

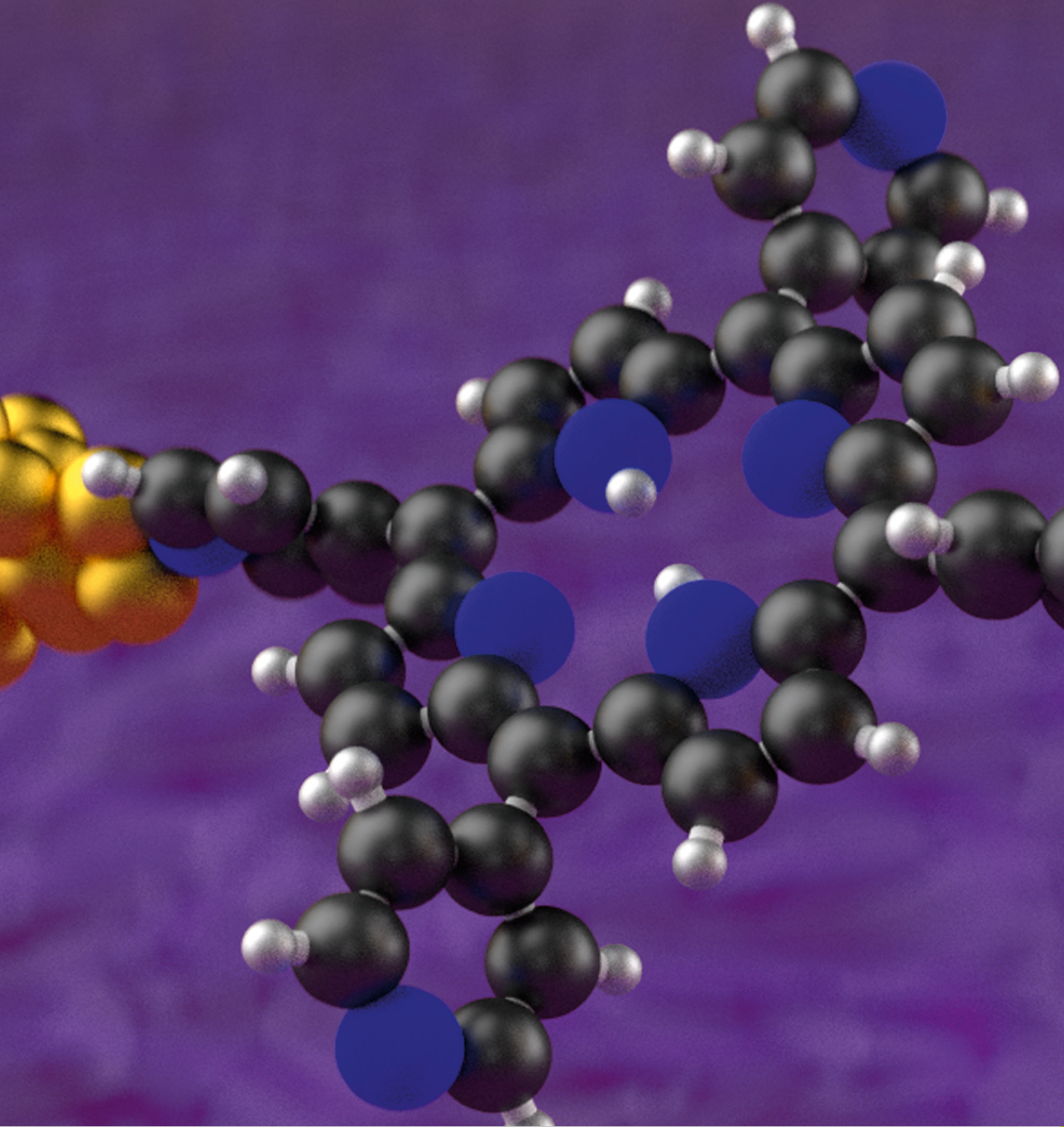
**Single molecule localization microscopy: Imaging of cellular structures
and a new three-dimensional localization technique**

X. Fan (2014), XII, 92 pp
ISBN: 978-3-95806-014-2

Band / Volume 98

Cryogenic Break-Junction Characterization of Single Organic Molecules

T. Grellmann (2014), VI, 86 pp
ISBN: 978-3-95806-015-9



Schlüsseltechnologien / Key Technologies
Band / Volume 98
ISBN 978-3-95806-015-9